IMT School for Advanced Studies, Lucca
Lucca, Italy

Novel Interface Discretisation Methods for Contact Mechanics

PhD Program in Systems Science

Track in Computer Science and Systems Engineering

XXXIII Cycle

By

Jacopo Bonari

2021

The dissertation of Jacopo Bonari is approved.

PhD Program Coordinator: Prof. Rocco De Nicola, IMT School for Advanced Studies Lucca

Advisor: Prof. Dr. Ing. Marco Paggi, IMT School for Advanced Studies Lucca

Co-Advisor: Univ.-Prof. Dr.-Ing. Alexander Popp, Universität der Bundeswehr München

The dissertation of Jacopo Bonari has been reviewed by:

Prof. Dr. Ing. Michele Ciavarella, Politecnico di Bari

Dr. Vladislav Yastrebov, MINES ParisTech, PSL University

IMT School for Advanced Studies Lucca
2021

Contents

List of Figures

List of Tables

Acknowledgements

According to Umberto Eco, a student is not supposed to thank his advisor, since he only fulfils a duty. Well, I believe that there are many different ways in which this task can be performed, and I am equally sure that this specific one has been carried out in the best way possible. So, thanks to Prof. Dr. Ing. Marco Paggi for making the PhD an experience that I would repeat. A heartfelt thank goes to Univ.-Prof. Dr.-Ing. Alexander Popp, who hosted me far beyond the original plans and with whom I hope to keep collaborating in the future, together with Matthias, Ivo, Nora and all the IMCS Team, always ready to share their perspective and offer precious advice and expertise. I would also care to mention Prof. Paolo Valvo and Prof. Ramazan-Ali Jafari-Talookolaei, who introduced me to the research activity. I would not have reached this achievement without your encouragement. A heartfelt acknowledgement goes to my family, who has always supported me, has been my first sponsor since I started this path and still owes a proper dedication from the last graduation ceremony. I am not committing the same mistake twice. The second personal mention cannot but go to Vanessa, now more than ever not just a partner but, most important, a friend and a travel companion. Before starting the PhD, I have been told that the most valuable thing earned would have been the network of people met along the way. Thank you, Maurizio, for this disclosure; I found it definitely true. Thanks to all the people I have met at IMT, whom I considered from the beginning friends, and only after colleagues. Thanks to Maria Rosaria, who has been patient enough to work with me; I am really looking forward to col-

laborating with you again. A special acknowledgement goes to the old friends that I deeply missed during this troubled year. Thanks to all the guys from my hometown, I am looking forward to making some noise with you again. Thanks to Carlo, Paul, Fabiana and Laura, who I hope to see as soon as possible. Thanks to all the Engineering Without Borders group, I always considered you the guiding light to follow in this age of bewilderment and lack of references.

In conclusion, I would like to acknowledge the precious help in terms of funding received from the MIUR-DAAD Joint Mobility Program 2017 for the project "Multi-scale modelling of friction for large scale engineering problems", together with the contribution of the Erasmus+ European project that supported my mobility to the Bundeswehr Univerität München (Germany), where part of my research activity has been carried out and the funding from the project PRIN, "XFAST-SIMS: Extra fast and accurate simulation of complex structural systems".

Munich, May 2021.

Abstract

This thesis' main scope is the presentation of two different methodologies for the analysis of contact problems involving morphologically complex or rough surfaces. Both approaches rely on the Finite Element Method (FEM) as the chosen computational framework. They hinge on the definition of an interface finite element used to model the space encompassed by two solids in contact. This kind of interface element is shared with the field of non-linear fracture mechanics, employed for the simulation of non-linear crack growth according to Cohesive Zone Model (CZM). Here, for the first time, the formulation is extensively applied to contact mechanics. With no further modifications, the interface element is suited for the solution of contact problems involving smooth and conformal interfaces, exploiting a *node-to-node* approach and a penalty formulation for the enforcement of the contact constraints. The element is enriched with specific characteristics that allow for the solution of rough contact problems yet maintaining a very simple mesh discretisation, both using a single-scale and a multi-scale approach. In the single-scale approach, a novel methodology is exploited that considers an equivalent flat interface and accounts for the actual geometry by a suitable correction of the standard normal gap. In the multi-scale approach, the Boundary Element Method (BEM) is exploited for solving, at a micro-scale, the normal contact problem of a rough rigid indenter making contact with an elastic half-space, according to a far-field displacement determined by the deformation imposed at a macro-scale. The solution in terms of averaged pressure and mean separation is then passed back to the macro-scale.

Chapter 1

Introduction

1.1 Motivation

Current technological trends require the production and the analysis of structures down to the micro- and nano-scale. At this level of magnification, phenomena related to the texture of the surfaces of components in contact strongly affect their global physical response, which commonly involves transferring pure mechanical stress across an interface through normal and tangential contact forces. Relevant episodes concurrently taking place at the interface and closely entwined with the transmission of forces comprehend the transfer of heat and electrical potential, oxidation, corrosion, change in optical properties and fluid percolation, which in turn have relevant effects on the contacting surfaces wear, plasticity, contamination by third bodies, lubrication and phase transformations, to name the most relevant.

The deviation of a surface from perfect flatness at a certain magnification could directly stem from the property of the material it is made of, might be caused by local imperfections or even could be designed, tailored and obtained through specific machining processes. A particular form of special texturing, roughness or waviness can be investigated to obtain specific surface characteristics that enhance selected properties like adhesion, hydrophobicity or hygroscopicity.

1.2 State-of-the-art of rough contact mechanics

1.2.1 Analytical and statistical models

From a historical perspective, the probably most important outcome related to the awareness of the actual rough microscopical nature of surfaces resulted in the explanation given by Bowden and Tabor [1] of the effectiveness of the Coulomb friction law, which, in turn, is a direct consequence of the linear relationship that in a contact problem holds between the normal load and the *actual* contact area. This linear dependence emerged from experimental evidence in cases where *theory* predicted a non-linear relationship, e.g. in the context of the Hertz theory [2].

The first model that was capable of reproducing such linear dependency tackling a contact problem that involved micro-textured surfaces is due to Archard [3], where the author foresaw a characteristic that since then became of capital importance in the context of tribology and surface metrology in general, that most of engineered and natural surfaces exhibit a *self-affine fractal* topology over several different length scales, sometimes spanning from the atomic scale up to the characteristic length of the object [4, 5].

From the pioneering work of Archard, that together with the model of Greenwood and Williamson [6] paved the way for the theories whose fundamental assumptions are still today accepted, a dense network of increasingly accurate models came out. To name the most relevant, from whom many other models have been derived, we might recall Bush, Gibson, and Thomas [7] who treated the elastic contact between a rigid rough surface and a plane considering each asperity as a paraboloid with equal principal curvatures and applying the classical Hertzian solution for their deformation; A. and Bhusan [8], who have been the firsts to apply the fractals theory to the elastoplastic problem of contacting rough surfaces and Persson [9], who has developed a theory which, contrarily to the preceding ones, is more and more accurate as of the load increases, being exact for full contact. In between, many different formulations have been developed on top of the fundamentals for increasing their accuracy, enhancing their capabilities and overcome some of their

shortcomings. The problem of nominally flat spheres has been thoroughly investigated, thus extending the domain of analysis to curved nominally smooth interfaces, see Greenwood and Tripp [10], Pohrt and Popov [11], Yastrebov [12]. Several improvements over the original models have been obtained in the course of the years. To name a couple of them, Greenwood [13] obtained a simplified and more accurate version of Bush, Gibson and Thomas's theory using an approximate expression for the peaks' curvature instead of the exact one; Ciavarella, Delfine, and Demelio [14] set up a *discrete* Greenwood and Williamson model* using synthetic surfaces and accounting for first-order interaction between the asperities, obtained considering the half-plane displacement outside a single asperity contact area; later on Ciavarella, Greenwood, and Paggi [15] obtained a further improved model which accounted for the elastic displacement interaction between the asperities considering the average constant displacement given by the mean nominal pressure caused by the contact of a single peak.

The presented models deal with frictionless normal contact. Under specific assumptions, frictional contact can also be analysed by knowing the tangential load history without the need to directly addressing the related tangential problem. This line of research started with Cattaneo [16] and [17]; under the hypotheses of normal-tangential decoupling, linear displacements and half-space approximations, they proved that for a constant normal load and a monotonic increasing tangential load, the distribution of the tangential tractions could be expressed as the superposition of two normal tractions distributions related to a specific normal load. Since then, the result has been extended to general oblique load histories, see for example [18], Jäger [19], Jäger [20] and more complex contacting geometries, also determining non-compact contact domains, Ciavarella [21], Ciavarella [22], opening perspectives for the application of what is now commonly referred to as the *Ciavarella–Jäger theorem* to the analysis of frictional rough contacts.

The micromechanical contact theories presented here have been the basis for the analysis of rough surfaces and rough profiles contact prob-

*In contrast with the original one that relied on a continuous distribution of heights.

lems for decades, with the capability to address additional features that have not been properly enumerated here, being not part of the present dissertation. Among these, a key role is played by adhesive phenomena. For a complete survey of the range of application of micromechanical contact theories, the interested reader is referred to the recent thorough review paper by Vakis et al. [23] and to Müser et al. [24], where several different methodologies have been tested against a reference contact problem, and their results compared with a brute force numerical solution.

1.2.2 Numerical models

One of the main drawbacks of micromechanical contact theories is that they only predict global quantities, e.g. the effective contact area and the total reaction force, without providing punctual information on isolated contact spots in such a way that is often difficult, if not impossible, having exact pieces of information over the real distributions of contact tractions and consequently contact zones. In this perspective, numerical methods gained importance over the past years, thanks to improved computational power and efficiency. Among them, the most employed computational frameworks are the *Boundary Element Method* (BEM) and the *Finite Element Method* (FEM), with their special focus on contact mechanics.

The Boundary Element Method

The numerical framework referred to as BEM is a strategy for solving initial boundary value problems, which is particularly suited for contact mechanics since it only requires solving the problem at the frontier of the definition domain. The first applications date back to Andersson [25] and Andersson and Allan-Persson [26], where the method is formalised for the solution of the contact between two elastic solids characterised by a smooth boundary. A subset of the method has proven to be very effective for the solution of rough surfaces contact. Often, a synecdoche holds between BEM applied to rough surface contact and the broader BEM for

computational contact mechanics. The former covers the cases of rigid rough surfaces making contact at selected points with flat deformable half-spaces. The latter can solve contact between two bodies, which can be both elastic and have a general shape but are usually characterised by smooth boundaries. A recent article by Xu and Jackson [27] sheds light on this perhaps subtle nomenclature overlapping and rigorously proves that the second strictly reduces to the first when the aforementioned hypotheses are formulated. For the avoidance of any doubt, in the rest of the dissertation, the term BEM will be referred to the subset of the numerical framework dealing with a rigid rough surface making contact with an elastic half-space when $3D$ problems are addressed, or a rough profile making contact with an elastic half-plane under plane strain assumptions in the case of $2D$ geometries. The procedure is well summarised in Johnson [28, Ch. 5, pg. 144–152]. The surface displacements on the boundary, together with the related distribution of contact pressures, can be expressed by a *convolution* of the tractions and the related influence function, representing the displacement of a point given the action of a unitary load. This results in a boundary integral equation (BIE) discretised over the elastic frontier, obtaining a linear system in which the displacements are linked to the interface tractions via an influence matrix. The problem is solved via the proper inversion of the resulting system with the additional requirement of respecting the contact constraints, making the problem strongly non-linear. The influence matrix coefficients are available in the analytical form if the load is simply a point force acting on a semi-indefinite boundary, thanks to the Flamant and Boussinesq–Cerruti solution; if it is represented by a unitary distribution of normal pressure acting over a rectangular area, the solution obtained by Love [29] can be exploited; the results of Li and Berger [30] can be used if a triangular patch of constant or linearly varying pressure is assumed. More complex influence functions can be identified for the common $2D$ case of a semi-indefinite elastic layer of finite thickness, for which an analytical form can not be derived, see, e.g. [31], [32], [33] in which the method is applied to the solution of contact problems involving simple contacting geometries.

Exemplary instances of the application of BEM to frictionless contacts involving complex rough surfaces can be found in [34], together with a critical review of the most common non-linear solution algorithms, and [35], in which optimised solution strategies are adapted to the solution of the system of equations thanks to the characteristic block structure of the influence coefficients matrix.

The effects of friction can be taken into account using two principal approaches. The first is the application of the Ciavarella–Jäger theorem, which allows to solve the normal contact problem separately, and then defines the tangential solution as a proper superposition of normal states, an example of this application can be found in Paggi, Pohrt, and Popov [36], for monotonically increasing loads. The mentioned theorem is very powerful and allows to solve the frictional problem straightforwardly but relies on rather strong assumptions, namely the decoupling between normal and tangential tractions and the equality of the influence functions in the two coordinate directions. The second approach is less elegant but allows to overcome these limitations. The problem is solved iteratively; for each iteration, two active sets are defined for the tangential displacements, and the respect of Coulomb friction law is verified *a posteriori*. If a violation is detected, the nodes are moved to the proper active set according to a specific criterion. The procedure is repeated until all the nodes belonging to the sets composing the contact domain respect the tangential constitutive law. In this regard, an example is offered by Pohrt and Li [37], which solve the uncoupled problem with a full characterisation of the stick and slip separation zones under the action of a monotonic tangential load.

Thanks to an innovative approach introduced by Carbone and Putignano [38], the use of BEM has also been extended to linear viscoelastic materials under the sliding action of rough indenters, the interested reader is referred to the review by Putignano and Carbone [39]. The method is perfectly suitable for the steady-state analysis of the distribution of the normal traction arising in these contexts, together with the related side effects, one over the others, viscoelastic friction. This kind of dissipative phenomena should not be confused with Coulomb friction.

The asymmetry determines it in the distribution of normal contact forces caused during sliding motion by the viscoelastic effect. It is of great importance for quantifying bulk viscoelastic energy losses. However, to the best of the author's knowledge, the method is used in a frictionless sense concerning the classic static Coulomb friction. When this framework is validated with experimental results, the effects caused by classic friction are depurated, see e.g. Putignano, Reddyhoff, and Dini [40].

In conclusion, the pros and cons of BEM can be summarised, stating that it is well suited for the solution of contact problems involving rough surfaces given its pointwise input, which allows mapping complex geometries with the desired level of resolution without the need of also discretising the bulk. Given the characteristics of the problem, different strategies can be implemented for considering the effect of classic Coulomb friction. Conversely, its main shortcomings are that it is limited to simple bulk geometries, mostly half-spaces and finite-thickness layers. In general, it is subjected to the previous evaluation of a related influence function. Considering the exclusion of the categories of exception presented, the method is limited to small displacements regime and linear elastic materials. The overcoming of these limitations is difficult but not impossible. Different strategies can be implemented in this regard. An example is given in Zhao, Vollebregt, and Oosterlee [41], where a complex bulk geometry is considered, and the related influence functions are obtained separately via FEM.

The Finite Element Method

The Finite Element Method is today the most spread tool in the field of computational mechanics. Several strategies have been developed and refined in the course of the years for its successful application to contact mechanics problems. Without the aim of providing an exhaustive literature review, the interested reader is referred to the works of Wriggers [42] and Yastrebov and Breitkopf [43], for a general view of the subject; to Popp [44] for a particular focus on mortar methods and to De Lorenzis, Wriggers, and Hughes [45] for a comprehensive review of the isogeometric framework applied to contact problems.

The main strength of the numerical approaches shown in the preceding paragraph is its capability of ideally solving the problem in a deterministic sense[†], ideally with a one-to-one correspondence between the analysed point and its contact state, thanks to the fact that real fractal surfaces always present a high wavenumber cut-off which from the theoretical point of view is given by the breakdown of continuum mechanics hypotheses, but in practice happens before, given the presence on the surface of impurities, third bodies, fluid films etc. This important consideration also holds for FEM.

Applying FEM to the solution of contact problems involving the contact of fractal rough surfaces allows gaining a deeper understanding of many key features of the subject which were once precluded using the strategies exposed in the preceding paragraphs, prime examples being the analysis of finite displacements, different constitutive behaviours and more complex geometries. This comes with the cost of a remarkable increase in computational resources needed, together with the higher care required by a trustful discretisation of the surface. In this regard, it is useful to draw a comparison with BEM. For what concerns the resources needed, BEM only requires the discretisation of the interface without considering the bulk, which is not true for FEM. If we consider regular structured grids in $3D$, doubling the resolution employed for sampling the surface implies a quadratic increase in the mesh nodes, which is cubic for FEM, thus rapidly leading to unbearable problems. For this reason, the use of more complex meshing algorithms is required, capable of grading the mesh discretisation from the required level of fine resolution in correspondence of the contact surface to coarser element dimension in correspondence of the bulk, which usually is interested by a constant or slowly varying gradient of stress that does not require fine meshing. The direct result would be an unstructured mesh, with the related issues, unless specific strategies are put in place, for example, with the application of a specific mesh tying algorithm or limiting the changes of the finite elements characteristic dimensions to specifically limited layers of the mesh, a strategy whose employment is going to be reviewed in the lines

[†]Under the hypotheses of continuum mechanics, until the nanoscale threshold.

below.

Besides the high requirement of computational resources, another problem absent for BEM is the surface discretisation itself. In a previous numerical method, choosing an adequate number of grid points could be seen enough for satisfactory modelling of the morphology; this is true also for FEM, but with the additional caveat that the resulting mesh should be free of highly distorted elements that lead to poor computational efficiency or the end absence of convergence.

Given these considerations, the increase in computational resources witnessed in the recent past has opened new perspectives for the solution of contact problems involving fractal rough surfaces. To the best of the author's knowledge, the first instance of a rough surface contact problem solution via FEM can be found in Hyun et al. [46]. Here the rough surface is modelled starting from a flat plane, discretised via a standard regular mesh. After that, a heights field is assigned to each node. Simply displacing the node in a direction normal to the flat boundary by the required height might result in a badly shaped element. To overcome the issue, not only the surface nodes are displaced, but also the ones belonging to the bulk, each by a proper fraction of the total height, to globally obtain the desired rough surface,[‡] Fig. 1;

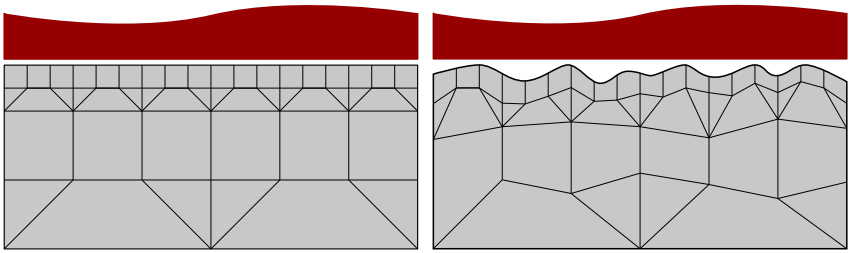

(a) Starting condition. **(b)** Mesh nodes displacements.

Figure 1: Possible mesh discretisation of a rough surface.

[‡]This operation could be made difficult by the fact that the mesh in the direction normal to the surface is not structured, given its gradation from finer to coarser. So it could not be straightforward to assess which quote of displacement to apply to subsurface nodes.

A different modelling approach has been followed by Bandeira, Wriggers, and de Mattos Pimenta [47], who solved a rough frictionless contact problem to derive specific contact interface laws. First of all, a flat plane has been discretised with standard elements. All and only the surface nodes have been displaced according to the surface roughness, but with the roughness height limited to a specific bandwidth to keep a certain limit aspect ratio for the elements. Moreover, an intermediate smoothing step has been performed. The actual rough surface has been smoothed via Bézier functions, this operation at the risk of filtering out roughness features related to its original morphology.

A complementary approach can be followed. It also starts with a flat interface as the first step. Then, on top of the flat boundary, another mesh is defined, with a vertical discretisation proportional to the surface height at that point, such to enforce a proper aspect ratio of the generated elements, Fig. 2. A drawback of the approach is that in the created layer, the mesh is structured, and a potentially high number of degrees of freedom is added to the problem. An example of this approach can be found in Yastrebov et al. [48], and Couto Carneiro, Pinto Carvalho, and Andrade Pires [49] in which the contact problem between deformable rough surfaces and rigid flat planes is solved in the context of Representative Volume Elements (RVE) identification and also by Wang et al. [50], which aims to provide a methodology for the deterministic solution of a frictional rough contact problem.

A mention of works related to the presented issues can be made. Thompson and Thompson [51] and Thompson [52] presents guidelines for the inclusion of measured rough surfaces in a FEM framework and, perhaps more relevant, to give an estimation of the goodness of the results obtained. As stated in the preceding paragraphs, FEM is a powerful method that can push the analysis in terms of the resolution to the limit but with a strongly increasing computational cost. In [53], an effective post-processing framework is proposed, capable of refining and giving an accurate estimation of the true contact area for relatively coarse discretisations, with the related gain in computational resources. In conclusion, from the purely computational side, the scripts developed by Loth

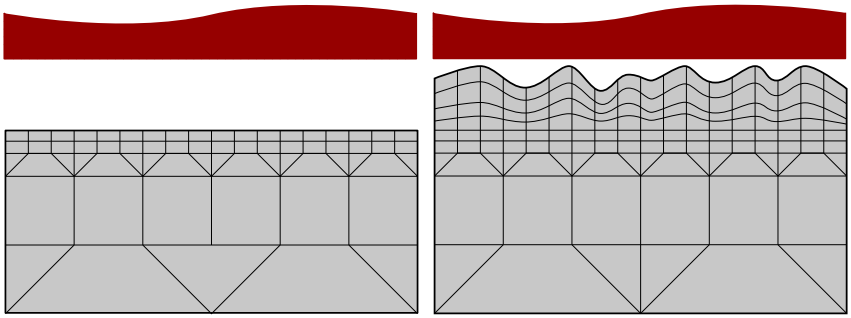

(a) Starting condition. **(b)** Additional elements.

Figure 2: Possible mesh discretisation of a rough surface.

et al. [54] and implemented in the mesh generator *GMSH* [55] provides a handy tool for the synthetic generation of rough meshes, also in the challenging scenario of curved nominally smooth interfaces, but with the drawback of being limited to unstructured meshes, which perhaps make the framework less attractive concerning more standard applications.

1.3 Scope of the dissertation

This thesis's main scope is to present two different methodologies for the analysis of contact problems involving morphologically complex or rough surfaces. Both approaches rely on FEM as a chosen computational framework. They hinge on the definition of an interface finite element used to model the space encompassed by two solids in contact. This kind of interface element is shared by the field of non-linear fracture mechanics, where it is employed for the simulation of non-linear crack growth according to the Cohesive Zone Model (CZM). Here for the first time, the formulation is extensively applied to contact mechanics. With no further modifications, this interface element is well-suited for the solution of contact problems involving smooth and conformal interfaces, exploiting a *node-to-node* approach and a penalty formulation for the enforcement of the contact constraints. In this work, the element is enriched with spe-

cific characteristics that allow for the solution of rough contact problems yet maintaining a very simple mesh discretisation, both using a single-scale and a multi-scale approach. A novel methodology is exploited in the single-scale approach that considers an equivalent flat interface and accounts for the actual geometry by a suitable correction of the standard normal gap. In the multi-scale approach, BEM is exploited for solving, at a micro-scale, the normal contact problem of a rough rigid indenter making contact with an elastic half-space, according to a far-field displacement determined by the deformation experienced by a macro-scale. The solution in terms of averaged pressure and mean separation is then passed back to the macro-scale.

1.4 Chapters overview

The content of the dissertation is organised as follows.

1.4.1 Interface finite element model

In this chapter, the formulation for an interface finite element is thoroughly derived, which constitutes the common support and basis for the two different methodologies presented. The element is adapted from the Cohesive Zone Model (CZM) employed in nonlinear fracture mechanics and mimics the interface shared by two generic bodies in conformal contact. Its variational formulation is thoroughly derived, starting from the strong form of governing differential equilibrium equations, down to a level adequate for its implementation inside a standard FEM software.

1.4.2 Mapping of a complex morphology into the finite element

A new approach for rough surface discretisation is described on top of the interface finite element presented in the previous chapter. It allows to solve non-conformal contact problems involving complex textured or rough surfaces by considering an equivalent flat interface and accounting for the actual geometry a correction of the standard normal gap. A

benchmark test is provided for assessing the validity of the formulation in the case of a reference problem for which the solution is known. Finally, the element is tested against a complex quasi-fractal surface under varying load conditions, with a complete derivation of the evolution of the vertical and horizontal traction fields. This chapter is part of [56]

1.4.3 A multi-scale formulation

A separation of the length scales is performed for examining the contact of nominally smooth but microscopically rough surfaces. Two different scenarios are coupled together. At the micro-scale, BEM is exploited for solving the normal contact problem of a rough rigid indenter making contact with an elastic half-space, according to a far-field displacement determined by the deformation experienced by the macro-scale. The solution in terms of averaged pressure and mean separation is finally passed back to the macro-scale. Different scale coupling strategies are discussed and compared. Part of the chapter can be found in [57].

1.4.4 Advanced applications

The versatility of the application proposed in Ch. 3 and its capability to be extended for the study of more complex problems are examined in the last chapter, where a $3D$ version of the implementation is considered together with instances concerning the indenting of non-elastic materials and the presence of the additional features, such as finite sliding displacements. This chapter is part of [58].

Chapter 2

General framework for an Interface Finite Element

In this Chapter, the derivation of an interface finite element employed in the analysis of contact problems is addressed. $2D$ *quad* and $3D$ *hex* shell-like elements, which so far have been extensively employed in non-linear fracture mechanics, will be applied to the analysis of contact problems. Some examples regarding the exploitation of this framework and its effectiveness and versatility in assessing reproducing complex interface behaviour can be found in studies related to cohesive crack growth, see for example Ortiz and Pandolfi [59] and Reinoso and Paggi [60], fracture models involving interface micromechanical features [61], finite thickness interfaces [62, 63], plasticity and fracture models with the concurrent use of a *node-to-segment* approach for enforcing non penetration conditions [64, 65, 66], simulation of dynamic non-linear peeling tests, [67], paper debonding, [68, 69], delamination of composite laminates and rubber-like materials, [70, 71, 72]. The versatility of the method can be proven by its application to simulate multi-physics phenomena involving heat exchanges across the interface [73] or, in general, the presence of more field variables. Particularly relevant in this context is its use combined with the *phase field* method for fracture mechanics, see for example Carollo, Reinoso, and Paggi [74]. Here, the method will be extensively applied

for the first time to the simulation of contact problems with complex geometrical characteristics.

The base configuration of the element is suitable for modelling the interaction of two deformable bodies under the hypothesis of small displacements. The following derivation relies on the strong differential form describing the equilibrium and compatibility conditions of two linear elastic bodies coming into contact across a *smooth*, *conformal* interface. This general condition is employed as a framework for the introduction of the *contact conditions* and the element itself, while hereinafter will be restricted. This because the contact typology investigated will deal with rigid indenters acting over deformable bulks, a scenario that can be classified under the label of *Signorini problem*. The aforementioned restriction allows extending and enriching the formulation of the interface element to deal consistently with the topics discussed in Ch. 3 and 4, where applications regarding a multi-scale approach and a new concept in treating a complex interface geometry will be discussed. It is good to pinpoint from now that the restriction made, viz. the rigid assumption over one of the bodies, is not a strict prerequisite, and a proper formalisation, which is beyond the scope of this dissertation and left for further investigation would allow for the relaxation of the mentioned restraint, resulting in a broader range of application.

2.1 Strong form of governing equations

Assume that two deformable bodies define the domains $\mathcal{B}_i \in \mathbb{R}^3$,$i = 1,\ 2$ in a reference configuration described by standard Cartesian basis $\mathbf{e}_1$, $\mathbf{e}_2$, $\mathbf{e}_3$. In absence of contact interactions, the boundary $\partial\mathcal{B} = \bigcup_{i=1,2} \partial\mathcal{B}_i$ of the domain can be split into two disjointed sets, Fig. 3:

(i) a region where displacements are imposed, *i.e.* the Dirichlet boundary $\partial\mathcal{B}_i^{\mathrm{D}}$;

(ii) a region where tractions are imposed, *i.e.* the Neumann boundary $\partial\mathcal{B}_i^{\mathrm{N}}$.

In case of contact, specific boundary conditions must be specified at the common interface $\partial\mathcal{B}^{\mathrm{C}}$ where contact might happen to enforce compatibility conditions. The boundary configuration is so divided into three mutually exclusive sets. Since the actual contact area is not known a priori, a further conceptual subdivision over $\partial\mathcal{B}^{\mathrm{C}}$ can be performed, distinguishing a region where contact actually occurs from the remaining part of the expected contact area, which phenomenologically belongs to the Neumann boundary[*]. The final boundary subdivision can be expressed as:

$$\partial\mathcal{B} = \partial\mathcal{B}_1^{\mathrm{D}} \cup \partial\mathcal{B}_2^{\mathrm{D}} \cup \partial\mathcal{B}_1^{\mathrm{N}} \cup \partial\mathcal{B}_2^{\mathrm{N}} \cup \partial\mathcal{B}^{\mathrm{C}}, \tag{2.1}$$

$$\partial\mathcal{B}_i^{\mathrm{D}} \cap \partial\mathcal{B}_i^{\mathrm{N}} = \partial\mathcal{B}_i^{\mathrm{N}} \cap \partial\mathcal{B}_i^{\mathrm{C}} = \partial\mathcal{B}_i^{\mathrm{C}} \cap \partial\mathcal{B}_i^{\mathrm{D}} = \varnothing, \text{ for } i = [1, 2] \tag{2.2}$$

The initial boundary value problem (IBVP) can be formalised by introducing a displacement field $\mathbf{u}_i(\mathbf{x}, t) = [u_i(\mathbf{x}, t),\, v_i(\mathbf{x}, t),\, w_i(\mathbf{x}, t)]^{\mathsf{T}}$. It

[*]So far this distinction could appear unnecessary since under the hypotheses of conformal contact the contact area is supposed to be known in advance. However, this is not true for *receding* contact problems and for the case which will be treated in Ch. 3, where conformal conditions only hold at the mesh level, while the actual contact geometries are different.

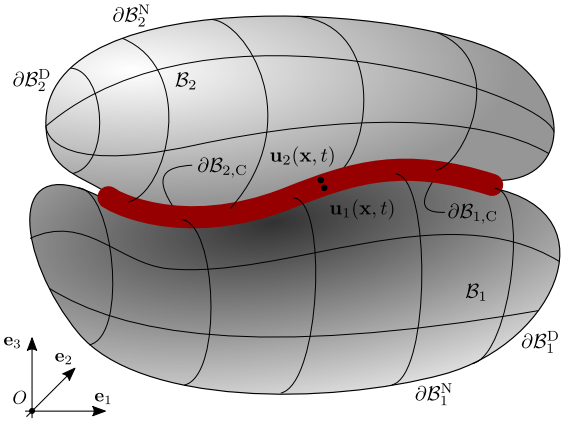

Figure 3: Identification of the domains Ω_i $(i = 1, 2)$, together with the imposed boundary conditions and the contact interface.

maps the displacements of the points of $\mathcal{B}_i$, identifying u_i, v_i and w_i the displacements along $\mathbf{e}_1$, $\mathbf{e}_2$ and $\mathbf{e}_3$, respectively, and recalling continuous and differentiable functions of the position vector $\mathbf{x}$ at time t. Furthermore, a small deformation strain tensor is defined as the symmetric part of the deformation gradient, $\mathbf{E}_i(\mathbf{x},t) = \nabla^S \mathbf{u}_i(\mathbf{x},t)$, with ∇^S standing for the symmetric part of the gradient operator.

With no contact contributions, the linear momentum balance equation for both $\mathcal{B}_1$ and $\mathcal{B}_2$, along with Dirichlet and Neumann boundary conditions on $\partial\mathcal{B}_i^{\mathrm{D}}$ and $\partial\mathcal{B}_i^{\mathrm{N}}$, can now be recalled for obtaining the strong form of equilibrium for the contacting bodies. Without taking into account contributions due to contact conditions, they read:

$$\nabla \cdot \mathbf{T} + \hat{\mathbf{b}}_0 = \rho_0 \ddot{\mathbf{u}} \quad \text{in } \mathcal{B}, \tag{2.3a}$$

$$\mathbf{T} \cdot \mathbf{n} = \hat{\mathbf{t}}_0 \quad \text{on } \partial\mathcal{B}^{\mathrm{N}}, \tag{2.3b}$$

$$\mathbf{u} = \hat{\mathbf{u}}_0 \quad \text{on } \partial\mathcal{B}^{\mathrm{D}}. \tag{2.3c}$$

This set of equations equally holds for both bodies, and in order to light the notation, the dependency over the body index i has been suppressed, together with the dependence of the field variables over the position vector $\mathbf{x}$ and time t. Nonetheless, since a second derivative for displacements is present, a set of two initial conditions must be defined as well, in the form:

$$\mathbf{u}(\mathbf{x},0) = \hat{\mathbf{u}}_0 \text{ in } \mathcal{B}, \tag{2.4a}$$

$$\dot{\mathbf{u}}(\mathbf{x},0) = \hat{\dot{\mathbf{u}}}_0 \text{ in } \mathcal{B}. \tag{2.4b}$$

2.2 Weak form of equations

The strong formulation expressed by Eq. (2.3) can be cast in a different form which permits to seek for an approximate yet accurate solution with weaker differentiability requirements. Multiplying it by a weighting function $\delta\mathbf{u}$, coincident with a virtual displacement, integrating over the domain $\mathcal{B}$, and finally integrating by parts the stress divergence term,

leads to:

$$\sum_{\gamma=1}^{2}\left[\int_{\mathcal{B}_\gamma}\mathbf{T}(\mathbf{u}_\gamma):\mathbf{E}_\gamma(\delta\mathbf{u})\,\mathrm{d}V+\int_{\mathcal{B}_\gamma}\rho_0\ddot{\mathbf{u}}_\gamma\cdot\delta\mathbf{u}\,\mathrm{d}V\right.$$
$$\left.-\int_{\partial\mathcal{B}_\gamma^{\mathrm{N}}}\hat{\mathbf{t}}_0\cdot\delta\mathbf{u}\,\mathrm{d}A-\int_{\mathcal{B}_\gamma}\hat{\mathbf{b}}_0\cdot\delta\mathbf{u}\,\mathrm{d}V\right]=0. \quad (2.5)$$

This equation is a formulation of the principle of virtual work that collects the energetic contributions given by the elastic energy and the inertial forces' work, the body forces and the external forces applied to the frontier. It can be observed that the original differential equation is still satisfied, provided that $\delta\mathbf{u}$ is arbitrary everywhere except in correspondence of $\partial\mathcal{B}^{\mathrm{D}}$, where *essential* boundary conditions are provided and the condition $\delta\mathbf{u}|_{\partial\mathcal{B}^{\mathrm{D}}}=0$ must hold.

The normal and tangential contact conditions on $\partial\mathcal{B}_C$ modify the weak form expressed by Eq. (2.5) with respect to the classic elastostatic variational equality, determining its modification into the following variational inequality, which from the energetic point of view takes into account the increase in stored elastic energy due to the presence of the contact constraints, with respect to the equivalent contactless elastic problem:

$$\sum_{\gamma=1}^{2}\left[\int_{\mathcal{B}_\gamma}\mathbf{T}(\mathbf{u}_\gamma):\mathbf{E}_\gamma(\delta\mathbf{u})\,\mathrm{d}V+\int_{\mathcal{B}_\gamma}\rho_0\ddot{\mathbf{u}}_\gamma\cdot\delta\mathbf{u}\,\mathrm{d}V\right.$$
$$\left.-\int_{\partial\mathcal{B}_\gamma^{\mathrm{N}}}\hat{\mathbf{t}}_0\cdot\delta\mathbf{u}\,\mathrm{d}A-\int_{\mathcal{B}_\gamma}\hat{\mathbf{b}}_0\cdot\delta\mathbf{u}\,\mathrm{d}V\right]\geq 0. \quad (2.6)$$

If the extension of the contact domain is known, the equality can be restored adding the energetic terms related to both normal and tangential contact, obtaining:

$$\sum_{\gamma=1}^{2}\left[\int_{\mathcal{B}_\gamma}\mathbf{T}(\mathbf{u}_\gamma):\mathbf{E}_\gamma(\delta\mathbf{u})\,\mathrm{d}V+\int_{\mathcal{B}_\gamma}\rho_0\ddot{\mathbf{u}}_\gamma\cdot\delta\mathbf{u}\,\mathrm{d}V\right.$$
$$\left.-\int_{\partial\mathcal{B}_\gamma^{\mathrm{N}}}\hat{\mathbf{t}}_0\cdot\delta\mathbf{u}\,\mathrm{d}A-\int_{\mathcal{B}_\gamma}\hat{\mathbf{b}}_0\cdot\delta\mathbf{u}\,\mathrm{d}V\right]-\delta\Pi_{\mathrm{n}}-\delta\Pi_\tau=0 \quad (2.7)$$

2.3 Contact kinematics and contact constraints

A relative displacement field can now be introduced for the description of the kinetics interaction between the two bodies in correspondence of the common contacting boundary $\partial\mathcal{B}^{\mathrm{C}}$. It is defined *gap field* across the interface and expressed as $\mathbf{g}(\mathbf{x},t) = \mathbf{u}_2(\mathbf{x},t) - \mathbf{u}_1(\mathbf{x},t)$, whose components describe the relative displacements of two corresponding nodes across the interface, expressed in global coordinates:

$$\mathbf{g}(\mathbf{x},t) = \left[\Delta u(\mathbf{x},t),\, \Delta v(\mathbf{x},t),\, \Delta w(\mathbf{x},t)\right]^{\mathsf{T}}, \tag{2.8}$$

being $\Delta(\cdot)$ the scalar difference between the corresponding quantities related to the two bodies. It has to be remarked that since the interface is conformal, a direct correspondence holds for matching points across it, with no need of setting up projection algorithms for the identification of the gap vector. This, together with the assumption of small displacements, makes it possible to define $\mathbf{g}(\mathbf{x},t)$ only in terms of the relative corresponding points displacements. Once the gap field is known, an inequality constraint can be set to define a non-penetration law that describes whether the interface is opening or the two bodies are coming into contact. Defining $\mathbf{n}$ as the outward pointing unit vector normal to $\partial\mathcal{B}_1$, the contact constraint takes the form:

$$g_{\mathrm{n}}(\mathbf{x},t) = \mathbf{g}(\mathbf{x},t)\cdot\mathbf{n} \geq 0, \tag{2.9}$$

being $g_{\mathrm{n}}(\mathbf{x},t)$ the projection of the gap field along the normal direction. The outward pointing normal $\mathbf{n}$ can be evaluated according to Eq. (2.28) for the $2D$ case and with Eq. (2.33c) for what concerns $3D$. When the inequality is strictly equal to zero, the bodies are in contact and the forces exchanged at the interface level are described by the traction vector $\mathbf{t}^{(\gamma)}$, equal and opposite for $\mathcal{B}_1$ and $\mathcal{B}_2$, that can be expressed according to Cauchy's stress theorem as:

$$\mathbf{T}\cdot\mathbf{n} = \mathbf{t} = p_{\mathrm{n}}\mathbf{n} + q_1\boldsymbol{\tau}_1 + q_2\boldsymbol{\tau}_2, \tag{2.10}$$

where the body-related superscript (γ) has been suppressed and $\boldsymbol{\tau}_j$ are the surface unit tangent vectors in correspondence of the contact point.

Consequently, the quantities p_n, q_1 and q_2 represent the normal and the tangential contact tractions.

2.3.1 Normal contact constraints, constitutive kinematics

If adhesive forces are neglected, the normal traction is always acting inward concerning the boundary, and therefore negative. This allows us to summarise the conditions for normal contact in the set of relations known as Hertz-Signorini-Moreau conditions:

$$g_\mathrm{n} \geq 0, \qquad p_\mathrm{n} \leq 0, \qquad g_\mathrm{n} p_\mathrm{n} = 0 \qquad \text{on } \partial\mathcal{B}_\mathrm{C}. \tag{2.11}$$

Eqs. (2.11) are well known in the field of constrained optimisation as Karush-Kuhn-Tucker (KKT) conditions. They correspond to a Linear Complementary Program (LCP) whose solution coincides with a related convex Quadratic Program (QP) optimality condition. Tackling the problem by treating normal contact as a unilateral constraint leads to accurate results in terms of normal contact tractions, but this comes at the cost of implementing a dedicated solution strategy.

While correct unilateral constraint enforcement will be retrieved in Chap. 4, in the context of BEM application, the FEM-related implementations addressed in the dissertation rely on a more versatile yet approximate approach. If the quantity addressed by the variable g_n is allowed to take negative values as well, a penetration function can be written reversing Eq. (2.9) as:

$$g_\mathrm{n} = \begin{cases} (\mathbf{u}_2 - \mathbf{u}_1) \cdot \mathbf{n} & \text{if } (\mathbf{u}_2 - \mathbf{u}_1) \cdot \mathbf{n} < 0, \\ 0 & \text{otherwise}, \end{cases} \tag{2.12}$$

which gives the level of the reciprocal interpenetration of $\mathcal{B}_1$ and $\mathcal{B}_2$. Starting from this definition, a displacement based normal contact constitutive relation can be defined introducing a penalty parameter ε_n and evaluating the normal contact traction as:

$$p_\mathrm{n} = \varepsilon_\mathrm{n} g_\mathrm{n}. \tag{2.13}$$

It is evident from the equation above that, given the discontinuous nature of the penetration function, traction different from zero will arise

only for a certain level of penetration, and that an exact value of p_{n} can be retrieved only for $\varepsilon_{\mathrm{n}} \to \infty$, restoring the enforcement of the KKT conditions. This constraint enforcement method goes under the name of *penalty approach*, Fig. 4, since it penalises every constraint violation by associating the related displacement solution with a high energy level.

The penalty method is widely used thanks to its ease of implementation and efficiency. It has the great advantage of not introducing additional unknowns to the problem. Moreover, this constitutive normal law for the interface represents outstanding support for introducing more complex constitutive relations, the next chapters' subject. Since in nature there are no free meals, the method presents drawbacks as well. As stated before, an exact solution is retrieved only for $\varepsilon_{\mathrm{n}} \to \infty$, but as the parameter grows, the problem becomes increasingly ill-conditioned. A trade-off must therefore be chosen between accuracy and well conditioning of the related solution system of equations. Apart from these considerations, the penalty parameter's introduction makes the solution problem-specific, and no general rules exist for its evaluation. For a given penalty parameter, remarkable differences also hold between problems solved under force control, for which equilibrium guarantees a more accurate transmission of forces across the interface, and problems solved under displacement control, where the interface stress depends on the applied displacement field [42, Ch. 6 pag. 119]. Some guidelines for evaluating the penalty parameters can be found in [75, 76, 77].

2.3.2 Tangential contact constraints and constitutive relation

If the effect of friction is accounted, the response of the contact interface can be further categorised in two different regions. The contact domain is therefore expressed as:

$$\begin{aligned} &\partial\mathcal{B}_{\mathrm{C,st}} \cup \partial\mathcal{B}_{\mathrm{C,sl}} = \partial\mathcal{B}_{\mathrm{C}}, \\ &\partial\mathcal{B}_{\mathrm{C,st}} \cap \partial\mathcal{B}_{\mathrm{C,sl}} = \varnothing. \end{aligned} \tag{2.14}$$

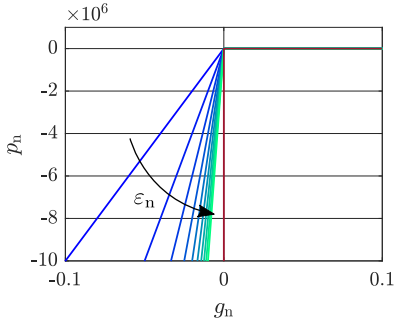

Figure 4: Hertz-Signorini-Moreau conditions *vs.* penalty approach.

In the equation above, the two subscripts denote regions of *stick* and *slip* respectively. The first is characterised by the absence of tangential relative motion between the bodies in contact, the second by a relative sliding which gives birth to tangential tractions that oppose the relative movement. The solution of continuity in the contact subdomain frontier is a direct consequence of the non-linearity of the Coulomb law employed for modelling friction, [†]. It can be expressed by the following set of equalities and inequalities:

$$\mathbf{g}_\tau = 0, \qquad \|\mathbf{q}_\tau\| \leq \mu p_\mathrm{n} \qquad \text{on } \partial\mathcal{B}_{\mathrm{C,st}}, \tag{2.15a}$$

$$\mathbf{q}_\tau = -\mu|p_\mathrm{n}|\frac{\dot{\mathbf{g}}_\tau}{\|\dot{\mathbf{g}}_\tau\|}, \qquad \dot{\mathbf{g}}_\tau > 0 \qquad \text{on } \partial\mathcal{B}_{\mathrm{C,sl}}, \tag{2.15b}$$

in which $\dot{\mathbf{g}}_\tau$ is the sliding velocity, and μ is the friction coefficient. According to Eq. (2.15b), the tangential reaction can prevent relative sliding up to a limit value coincident with $\mu|p_\mathrm{n}|$, above which relative sliding begins with a constant tangential reaction equivalent to the same threshold value. The interface behaviour is depicted in Fig. 5, together with the constitutive law employed for resolving the non-linearity in correspondence of the origin:

$$\mathbf{t}_\tau = -\mu|p_\mathrm{n}|\frac{\dot{\mathbf{g}}_\tau}{\|\dot{\mathbf{g}}_\tau\|}\tanh\frac{\|\dot{\mathbf{g}}_\tau\|}{\dot{\varepsilon}_\tau} \tag{2.16}$$

[†]Coulomb law is still an excellent compromise between ease and accuracy, see comments made over [1]

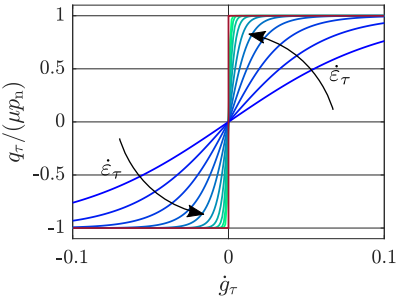

Figure 5: Coulomb friction law *vs.* regularised friction law.

Equation (2.16) can be seen as the tangential analogous of Eq. (2.13). Again a parameter $\dot{\varepsilon}_\tau$ is introduced for approximating a limiting case, recovered for $1/\dot{\varepsilon}_\tau \to \infty$, with considerations that are equivalent to the ones drawn for the normal penalty. As the normal penalty introduces a violation over the normal constraint, the assumptions defining the points relative to kinematics in the stick domain are not respected. A zero tangential traction is present only in combination with a null relative displacement, while the increase of $\mathbf{q}_\tau$ up to its limit value happens without a solution of continuity. It has to be remarked that the use of Eq. (2.16) only represents a possibility among many others. Different regularisation curves can be found in [42, Ch. 5, pag. 79-83] concerning different sets of material contacts.

2.4 Contact contribution to the weak form

According to the constitutive equations defined for the interface, the contributions of the interface tractions to the principle of virtual work expressed by Eq. (2.7) can be stated, for normal and tangential directions respectively, as:

$$\delta\Pi_\mathrm{n} = \int_{\partial\mathcal{B}_\mathrm{C}} p_\mathrm{n}(\mathbf{u})\delta g_{\mathrm{lc,n}}(\mathbf{u})\,\mathrm{d}A, \quad \delta\Pi_\tau = \int_{\partial\mathcal{B}_\mathrm{C}} \mathbf{q}_\tau(\mathbf{u})^\mathsf{T}\delta\mathbf{g}_{\mathrm{lc},\tau}(\mathbf{u},\dot{\mathbf{u}})\,\mathrm{d}A, \tag{2.17}$$

where $g_{\mathrm{lc,n}}(\mathbf{u})$ and $\mathbf{g}_{\mathrm{lc},\tau}(\mathbf{u},\dot{\mathbf{u}})$ are the normal and tangential gap field, evaluated in the local reference system. The displacement field $\mathbf{u}$, solution of the weak form is such that it corresponds to the minimum of the energy for any choice of the virtual displacements $\delta\mathbf{u}$.

2.5 Finite element discretisation

The numerical solution of the variational equality described by Eq. (2.7) in the framework of the finite element method requires the geometrical approximation of the two bulks, $\mathcal{B}_\gamma$, and of the interface, $\partial\mathcal{B}_{\mathrm{C}}$, and their discretisation into finite elements, a process that can be formalised as:

$$\mathcal{B}_\gamma \approx \mathcal{B}_\gamma^{\mathrm{h}} = \bigcup_{\mathrm{e}=1}^{n_\Omega} \Omega_\gamma^{(\mathrm{e})}, \qquad \partial\mathcal{B}_{\mathrm{C}} \approx \partial\mathcal{B}_{\mathrm{C}}^{\mathrm{h}} = \bigcup_{\mathrm{e}=1}^{n_\Gamma} \Gamma^{(\mathrm{e})}, \tag{2.18}$$

where $\Omega^{(\mathrm{e})}$ represents the element that compose the geometric approximation $\mathcal{B}^{\mathrm{h}}$ of the bulk $\mathcal{B}$, while $\Gamma^{(\mathrm{e})}$ is the interface element in which $\partial\mathcal{B}_{\mathrm{C}}^{\mathrm{h}}$ is divided, in its turn an approximation of $\partial\mathcal{B}_{\mathrm{C}}$, Fig. 6. Throughout the dissertation, in the numerical examples provided, the bulk has been modelled using the following approach:

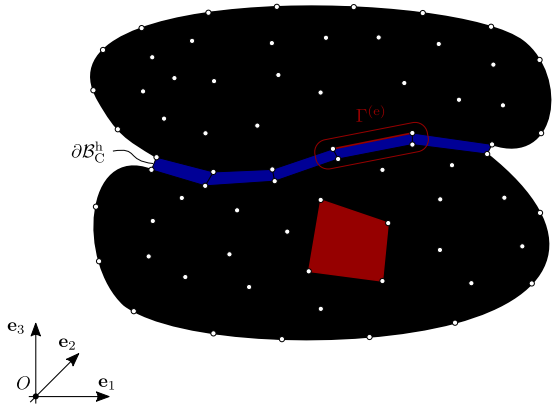

Figure 6: FEM approximation of the bulk and the interface.

- for 2D problems:
  - an unstructured mesh has been used for the simulation of infinite domains, made of standard linear isoparametric *tria* and *quad* elements. The need for simulating unlimited domains came arose for validation purposes, *viz.* Sec. 3.2
  - a structured mesh only made of *quad* elements has been used for reproducing finite-size bulks, employed for practical applications;
- for 3D problems:
  - an unstructured mesh has been used for the simulation of infinite domains, made of standard linear isoparametric 5-nodes *pyramid*, 4-nodes *teth* and 8-nodes *hex* elements, see Sec. 5.1.2
  - a structured mesh made of 8-nodes *hex* elements only has been used for reproducing finite-size bulks, employed for practical applications.

There is no restriction on the finite element typology to be employed for the bulk, provided that it is consistent with the interface discretisation. Since a contact strategy analogous to a *node-to-node* approach has been chosen, a discretisation of the two bulks characterised by matching nodes at the interface is necessary. Under the hypothesis of small displacements, this requirement makes possible the analysis of frictional effects due to relative nodal tangential displacements, since slip will be infinitesimal too [78]. Upon these premises, a 4-nodes interface finite element $\Gamma^{(e)}$ is introduced, as a special case of a collapsed 4-nodes *quad* element, for 2D problems, together with its 3D extension, a 8-nodes shell-like *hex* element.

The interface element is defined by two facets, each belonging to the boundary of one of the two bodies, see Fig. 7, each facet characterised by two or four nodes according to the problem dimension. Equation (2.8) expresses the energetic contribution of the interface to the global weak

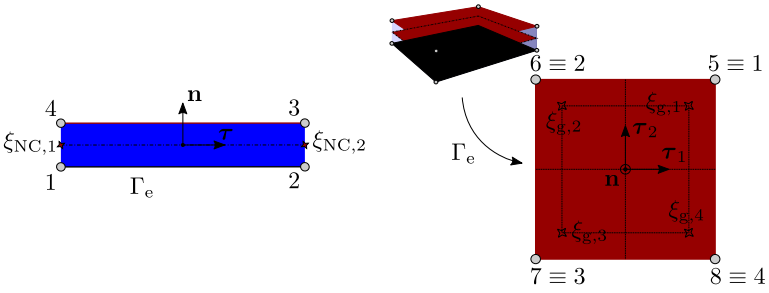

(a) *quad* finite element. **(b)** *hex* finite element.

Figure 7: $2D$ and $3D$ interface finite elements.

form. This contribution explicitly reads:

$$\delta\boldsymbol{\Pi} \approx \delta\boldsymbol{\Pi}_{\mathrm{h}} = \int_{\partial\mathcal{B}_{\mathrm{C}}^{\mathrm{h}}} \mathbf{p}(\mathbf{u}) \cdot \delta\mathbf{g}_{\mathrm{lc}}(\mathbf{u}, \dot{\mathbf{u}})\, \mathrm{d}A = \bigcup_{\mathrm{e}=1}^{n_\Gamma} \int_{\Gamma_e} \tilde{\mathbf{p}}(\hat{\mathbf{u}}_{\mathrm{e}})^{\mathsf{T}} \delta\tilde{\mathbf{g}}_{\mathrm{lc}}(\hat{\mathbf{u}}_{\mathrm{e}}, \hat{\dot{\mathbf{u}}}_{\mathrm{e}})\, \mathrm{d}A, \quad (2.19)$$

where Eq. (2.17) has been condensed collecting the normal and tangential terms in the traction vector $\mathbf{p} = [q_{\tau 1}, q_{\tau 2}, p_{\mathrm{n}}]^{\mathsf{T}}$ and local gap vector $\mathbf{g}_{\mathrm{lc}} = [g_{\tau 1}, g_{\tau 2}, g_{\mathrm{n}}]^{\mathsf{T}}$. In the equation above, the symbol $(\tilde{\cdot})$ denotes the isoparametric form of the element displacements and their related quantities, while $(\hat{\cdot})$ their respective nodal values, with the subscripts e spanning through the total number of elements n_Γ employed for the interface discretisation.

Consequently, the isoparametric finite element approximation of the linear normal and tangential gaps $\tilde{\mathbf{g}}_{\mathrm{lc}}$ has the general expression:

$$\tilde{\mathbf{g}}_{\mathrm{lc,e}} = \mathbf{Q}\mathbf{B}(\boldsymbol{\xi})\hat{\mathbf{u}}_{\mathrm{e}}, \quad (2.20)$$

where $\hat{\mathbf{u}}_{\mathrm{e}}$ is the nodal displacement vector and $\mathbf{B}(\boldsymbol{\xi})$ a linear operator which evaluates the proper relative nodal displacements and interpolates them along the element $\Gamma^{(\mathrm{e})}$. For this purpose, a standard system of *parent coordinates* is introduced for parametrising the value of the field on

each interval across different nodes. In the present case, standard linear shape functions for the *quad* element and bi-linear shape functions for the *hex* element are chosen. The final step is the multiplication by the rotation matrix $\mathbf{Q}$, for moving from the global to the local reference system, aligned to the interface element. The derivation will be specialised for a plane strain case 2-dimensional case and a full 3-dimensional scenario in the next two sections.

2.5.1 $2D$ interface finite element formulation

In 2D problems, the vectors and matrix operators of Eq. (2.20) take the following form. First, a nodal displacements vector is introduced, being u_i and v_i the horizontal and vertical displacements evaluated in the global reference system, and numbered according to Fig. 7a:

$$\hat{\mathbf{u}}_{\mathrm{e}} = \begin{bmatrix} u_1 & v_1 & u_2 & v_2 & u_3 & v_3 & u_4 & v_4 \end{bmatrix}^{\mathsf{T}}, \tag{2.21}$$

their relative difference is evaluated by pre-multiplying the previous by:

$$\mathbf{L} = \begin{bmatrix} -1 & 0 & 0 & 0 & 0 & 0 & +1 & 0 \\ 0 & -1 & 0 & 0 & 0 & 0 & 0 & +1 \\ 0 & 0 & -1 & 0 & +1 & 0 & 0 & 0 \\ 0 & 0 & 0 & -1 & 0 & +1 & 0 & 0 \end{bmatrix}. \tag{2.22}$$

Linear shape functions are employed for interpolating the values of the gap field along with the element:

$$\mathbf{N} = \begin{bmatrix} N_1(\xi) & 0 & N_2(\xi) & 0 \\ 0 & N_1(\xi) & 0 & N_2(\xi) \end{bmatrix}, \tag{2.23}$$

where, as usual, the two linear interpolating functions take the form:

$$N_1(\xi) = \frac{1-\xi}{2}, \qquad N_2(\xi) = \frac{1+\xi}{2}. \tag{2.24}$$

Finally, the operator $\mathbf{B}(\xi) = \mathbf{N}(\xi)\mathbf{L}$ is introduced, and a rotation is applied for aligning the gap field to the element local reference system:

$$\mathbf{Q} = \begin{bmatrix} \tau_x & \tau_y \\ n_x & n_y \end{bmatrix}. \tag{2.25}$$

In Eq. (2.25), the entries of the rotation matrix are the unit vectors defining the local normal and tangential directions of the interface, such that $\mathbf{n} = [n_x,\, n_y]^\mathsf{T}$ and $\boldsymbol{\tau} = [\tau_x,\, \tau_y]^\mathsf{T}$. They are evaluated in function of the global coordinates of the four nodes. A centerline for the element is defined, linking the points $\mathbf{x}_{\mathrm{m},i} = [x_{\mathrm{m},i},\, y_{\mathrm{m},i}]^\mathsf{T}$, $i = (1, \ldots, 2)$, each of them located in the position sketched in Fig. 7a, and with expression:

$$\mathbf{x}_{\mathrm{m},1} = \frac{1}{2}(\mathbf{x}_1 + \mathbf{x}_4), \qquad \mathbf{x}_{\mathrm{m},2} = \frac{1}{2}(\mathbf{x}_2 + \mathbf{x}_3). \tag{2.26}$$

A length l_0 can be defined as $l_0 = \|\mathbf{x}_{\mathrm{m},2} - \mathbf{x}_{\mathrm{m},1}\|$, and finally the unit vectors as:

$$\tau_x = \frac{x_{\mathrm{m},2} - x_{\mathrm{m},1}}{l_0}, \qquad \tau_y = \frac{y_{\mathrm{m},2} - y_{\mathrm{m},1}}{l_0}, \tag{2.27}$$

$$n_x = -\frac{y_{\mathrm{m},2} - y_{\mathrm{m},1}}{l_0}, \qquad n_y = \frac{x_{\mathrm{m},2} - x_{\mathrm{m},1}}{l_0}. \tag{2.28}$$

The explicit expression of $\tilde{\mathbf{p}}_\mathrm{e}$ and $\tilde{\mathbf{g}}_{\mathrm{lc,e}}$ in function of $\hat{u}_\mathrm{e}$ allows to evaluate the energetic contribution of the interface elements to the system, according to Eq. (2.19).

2.5.2 $3D$ interface finite element formulation

An analogous approach can be followed for the derivation of the interface element kinematics in 3D. The local gap field maintains the same expressions, while the matrix operators can be re-defined according to the element node numbering of Fig. 7b. In particular, the nodal displacements are now stored as $\hat{\mathbf{u}}_\mathrm{e} = [u_1, v_1, w_1, \ldots, u_8, v_8, w_8]^\mathsf{T}$, where nodes 1 to 4 belong to the inferior facet, nodes 5 to 8 to the superior facet and u_i, v_i and w_i are the nodal displacements in the global reference system. The matrix operator $\mathbf{B}(\boldsymbol{\xi})$ interpolates the tangential and normal gaps across the interface:

$$\mathbf{B}(\boldsymbol{\xi}) = \begin{bmatrix} -N_1(\boldsymbol{\xi}) & 0 & 0 & \ldots & +N_4(\boldsymbol{\xi}) & 0 & 0 \\ 0 & -N_1(\boldsymbol{\xi}) & 0 & \ldots & 0 & +N_4(\boldsymbol{\xi}) & 0 \\ 0 & 0 & -N_1(\boldsymbol{\xi}) & \ldots & 0 & 0 & +N_4(\boldsymbol{\xi}) \end{bmatrix}. \tag{2.29}$$

In the present case, standard bilinear shape functions have been employed, with the expression:

$$N_1(\boldsymbol{\xi}) = \frac{1}{2}(1+\xi)\frac{1}{2}(1+\eta), \tag{2.30a}$$

$$N_2(\boldsymbol{\xi}) = \frac{1}{2}(1-\xi)\frac{1}{2}(1+\eta), \tag{2.30b}$$

$$N_3(\boldsymbol{\xi}) = \frac{1}{2}(1-\xi)\frac{1}{2}(1-\eta), \tag{2.30c}$$

$$N_4(\boldsymbol{\xi}) = \frac{1}{2}(1+\xi)\frac{1}{2}(1-\eta), \tag{2.30d}$$

The gap in the local reference frame can be evaluated by applying a suitable rotation matrix $\mathbf{Q}$, function of the coordinates $\mathbf{x}_i = [x_i,\, y_i\, z_i]^T$, $i = (i, \ldots, 8)$ of the element nodes:

$$\mathbf{Q} = \begin{bmatrix} \tau_{1x} & \tau_{1y} & \tau_{1z} \\ \tau_{2x} & \tau_{2y} & \tau_{2z} \\ n_x & n_y & n_z \end{bmatrix}. \tag{2.31}$$

The tangential and normal unit vectors $\boldsymbol{\tau}_1$, $\boldsymbol{\tau}_2$ and $\mathbf{n}$ are evaluated in function of the global coordinates of the nodes $\mathbf{x}_{\mathrm{m},i} = [x_{\mathrm{m},i},\, y_{\mathrm{m},i}\, z_{\mathrm{m},i}]^{\mathsf{T}}$, $i = (1, \ldots, 4)$, each of them located on the mid-plane lying parallel to the two opposite facets, sketched in Fig. 7b and with expression:

$$\mathbf{x}_{\mathrm{m},i} = \frac{1}{2}(\mathbf{x}_i + \mathbf{x}_{i+4}) \quad \text{for } i = (1, \ldots, 4) \tag{2.32}$$

Given $\mathbf{x}_{\mathrm{m},i}$, the unit vectors read:

$$\boldsymbol{\tau}_1 = \frac{(\mathbf{x}_{\mathrm{m},1} + \mathbf{x}_{\mathrm{m},4}) - (\mathbf{x}_{\mathrm{m},2} + \mathbf{x}_{\mathrm{m},3})}{\|(\mathbf{x}_{\mathrm{m},1} + \mathbf{x}_{\mathrm{m},4}) - (\mathbf{x}_{\mathrm{m},2} + \mathbf{x}_{\mathrm{m},3})\|}, \tag{2.33a}$$

$$\boldsymbol{\tau}_2 = \frac{(\mathbf{x}_{\mathrm{m},1} + \mathbf{x}_{\mathrm{m},2}) - (\mathbf{x}_{\mathrm{m},3} + \mathbf{x}_{\mathrm{m},4})}{\|(\mathbf{x}_{\mathrm{m},1} + \mathbf{x}_{\mathrm{m},2}) - (\mathbf{x}_{\mathrm{m},3} + \mathbf{x}_{\mathrm{m},4})\|}, \tag{2.33b}$$

$$\mathbf{n} = \boldsymbol{\tau}_1 \wedge \boldsymbol{\tau}_2. \tag{2.33c}$$

2.6 Evaluation of the residual vector and effective dynamic tangent matrix

The contribution of a single interface element to Eq. (2.7) can now be evaluated. Recalling the expression of the traction vector $\tilde{\mathbf{p}}_{\mathrm{e}}$, it is possi-

ble to express the variation of the normal penalty and tangential contributions apported by each element as:

$$\delta\tilde{\Pi}_{\mathrm{e}} = \int_{\square} \delta\mathbf{g}(\hat{\mathbf{u}}_{\mathrm{e}})^{\mathsf{T}}\mathbf{p}(\hat{\mathbf{u}}_{\mathrm{e}}, \hat{\dot{\mathbf{u}}}_{\mathrm{e}}) j_{\mathrm{e}}(\boldsymbol{\xi})\,\mathrm{d}\boldsymbol{\xi}, \tag{2.34}$$

where the integral over the original domain $\Gamma^{(\mathrm{e})}$ has been converted, via a change of the integration variable to an integral on the parent coordinates domain defined by $\square = \{\boldsymbol{\xi} \in \mathbb{R}^2 \big| (|\xi|, |\eta|) \leq 1\}$ in 3D and by $\square = \{\xi \in \mathbb{R} \big| |\xi| \leq 1\}$ in 3D. The determinant of the transformation $j_{\mathrm{e}}(\boldsymbol{\xi})$ mapping the change of coordinates from the global to the parent reference system reads, employing standard bi-linear shape functions:

$$j_{\mathrm{e}}(\boldsymbol{\xi}) = \frac{\partial \tilde{x}_{\mathrm{e}}}{\partial \xi}\frac{\partial \tilde{y}_{\mathrm{e}}}{\partial \eta} - \frac{\partial \tilde{x}_{\mathrm{e}}}{\partial \eta}\frac{\partial \tilde{y}_{\mathrm{e}}}{\partial \xi} \tag{2.35}$$

and simply $j_{\mathrm{e}}(\xi) = \partial \tilde{x}_{\mathrm{e}}/\partial \xi$ for the linear shape functions of the *quad* element, where $\tilde{x}_{\mathrm{e}}$ and $\tilde{y}_{\mathrm{e}}$ represent the isoparametric form of the global coordinates. The variation of the local gap is given, in matrix notation, by:

$$\delta\mathbf{g}(\hat{\mathbf{u}}_{\mathrm{e}}) = \frac{\partial \tilde{\mathbf{g}}}{\partial \hat{\mathbf{u}}_{\mathrm{e}}}\delta\hat{\mathbf{u}}_{\mathrm{e}} = \mathbf{Q}\mathbf{B}(\boldsymbol{\xi})\delta\hat{\mathbf{u}}_{\mathrm{e}}. \tag{2.36}$$

Finally, the variation can be set to zero, and the residual vector obtained:

$$\delta\tilde{\Pi}_{\mathrm{e}} = \delta\hat{\mathbf{u}}_{\mathrm{e}}^{\mathsf{T}} \int_{\square} \mathbf{B}^{\mathsf{T}}\mathbf{Q}^{\mathsf{T}}\mathbf{p}(\hat{\mathbf{u}}_{\mathrm{e}}, \hat{\dot{\mathbf{u}}}_{\mathrm{e}}) j_{\mathrm{e}}(\boldsymbol{\xi})\,\mathrm{d}\boldsymbol{\xi} = 0, \tag{2.37}$$

which gives:

$$\mathbf{R}_{\Gamma}(\hat{\mathbf{u}}_{\mathrm{e}}, \hat{\dot{\mathbf{u}}}_{\mathrm{e}}) = \int_{\square} \mathbf{B}^{\mathsf{T}}\mathbf{Q}^{\mathsf{T}}\mathbf{p}(\hat{\mathbf{u}}_{\mathrm{e}}, \hat{\dot{\mathbf{u}}}_{\mathrm{e}}) j_{\mathrm{e}}(\boldsymbol{\xi})\,\mathrm{d}\boldsymbol{\xi} = \mathbf{0}, \tag{2.38}$$

where the subscript Γ specifies that the equation above refers to an element belonging to the interface. A quadrature formula can be exploited for evaluating the integral in $\mathbf{R}$. This requires the sampling of the integrand at specific locations. For the 2D *quad* element, a Newton-Cotes integration formula has been used, with unitary weights w_i and two quadrature points set in correspondence of $\xi_{\mathrm{NC}} = \pm 1$. For the 3D *hex* element, a Gauß-Legendre integration scheme has been exploited, still

with unitary weights w_i, but sampling points (hereinafter Gauß points, $\boldsymbol{\xi}_{\mathrm{G},k}$, $k = [1, \ldots, 4]$), located at:

$$\boldsymbol{\xi}_{\mathrm{G},1} = \left(+\frac{\sqrt{3}}{3}, +\frac{\sqrt{3}}{3}\right), \qquad \boldsymbol{\xi}_{\mathrm{G},2} = \left(-\frac{\sqrt{3}}{3}, +\frac{\sqrt{3}}{3}\right), \tag{2.39}$$

$$\boldsymbol{\xi}_{\mathrm{G},3} = \left(-\frac{\sqrt{3}}{3}, -\frac{\sqrt{3}}{3}\right), \qquad \boldsymbol{\xi}_{\mathrm{G},4} = \left(+\frac{\sqrt{3}}{3}, -\frac{\sqrt{3}}{3}\right). \tag{2.40}$$

The integral formulation of the residual becomes:

$$\mathbf{R}_{\Gamma}(\hat{\mathbf{u}}_{\mathrm{e}}, \hat{\dot{\mathbf{u}}}_{\mathrm{e}}) = \sum_{k=1}^{\mathrm{nnd}} w_k \mathbf{B}(\boldsymbol{\xi}_{\mathrm{G},k})^{\mathsf{T}} \mathbf{Q}^{\mathsf{T}} \mathbf{p}_k(\hat{\mathbf{u}}_{\mathrm{e}}, \hat{\dot{\mathbf{u}}}_{\mathrm{e}}) j_{\mathrm{e}}(\boldsymbol{\xi}_{\mathrm{G},k}), \tag{2.41}$$

being nnd the number of nodes of the element.

2.7 Assembly process and linearisation of the residual vector

Given the constitutive laws employed, Eq. (2.41) represents a set of non-linear transient equations, which can be addressed using a suitable numerical scheme. A Newton-Raphson iterative algorithm has been employed in combination with a direct solver for the solution of the resulting linear system.

The elementwise quantities are assembled together via an *assembly operator* for constructing the final set of equations:

$$\mathop{\mathsf{A}}_{\mathrm{e}=1}^{n_\Gamma + n_\Omega} \left[\mathbf{R}_{\Gamma}(\hat{\mathbf{u}}_{\mathrm{e}}, \hat{\dot{\mathbf{u}}}_{\mathrm{e}}) + \mathbf{R}_{\Omega}(\hat{\mathbf{u}}_{\mathrm{e}}, \hat{\ddot{\mathbf{u}}}_{\mathrm{e}}) \right] = \mathbf{R}(\hat{\mathbf{u}}, \hat{\dot{\mathbf{u}}}, \hat{\ddot{\mathbf{u}}}) = \mathbf{0}, \tag{2.42}$$

where n_Γ and n_Ω is the total number of elements, employed for the subdivision of the interface and bulk. To light up the notation, hereinafter the vector of nodal displacements $\hat{\mathbf{u}}_{\mathrm{e}}$, velocities $\hat{\dot{\mathbf{u}}}_{\mathrm{e}}$ and accelerations $\hat{\ddot{\mathbf{u}}}_{\mathrm{e}}$ will be replaced by $\mathbf{u}$, $\dot{\mathbf{u}}$, $\ddot{\mathbf{u}}$ respectively. For every time step, a *Newton-Raphson* algorithm is used for the iterative solution of Eq. (2.42). The residual vector is linearised introducing the tangent matrix $\mathbf{S}$, evaluated

as the directional derivative of the global residual in correspondence of a trial solution $\mathbf{u}^{(0)}$. The resulting set of linear equations reads:

$$\mathbf{S}^{(0)}\mathrm{d}\mathbf{u} = -\mathbf{R}^{(0)}, \tag{2.43}$$

where the tangent matrix is obtained as:

$$\mathbf{S} = -\frac{\partial \mathbf{R}}{\partial \mathbf{u}} - \frac{\partial \mathbf{R}}{\partial \dot{\mathbf{u}}}\frac{\partial \dot{\mathbf{u}}}{\partial \mathbf{u}} - \frac{\partial \mathbf{R}}{\partial \ddot{\mathbf{u}}}\frac{\partial \ddot{\mathbf{u}}}{\partial \mathbf{u}} = c_1\mathbf{K} + c_2\mathbf{C} + c_3\mathbf{M}, \tag{2.44}$$

being $\mathbf{K}$ the stiffness matrix, $\mathbf{C}$ the damping matrix, $\mathbf{M}$ the mass matrix and c_1, c_2 and c_3 scalar coefficients which depends on the time step Δt and on the selected time integration scheme. The trial solution is updated with the result coming from Eq. (2.43), such that at iteration $(i+1)$ we have:

$$\mathbf{u}^{(i+1)} = \mathbf{u}^{(i)} + \mathrm{d}\mathbf{u}^{(i)}. \tag{2.45}$$

The procedure is repeated until a convergence criterion is met. In the cases treated throughout the dissertation, the convergence condition is issued defining a relative *energy error* which must lay below a specified threshold:

$$\frac{E^{(i)}}{E^{(0)}} = \frac{\mathrm{d}\mathbf{u}^{(i)\mathsf{T}}\mathbf{R}^{(i)}}{\mathrm{d}\mathbf{u}^{(0)\mathsf{T}}\mathbf{R}^{(0)}} \leq 1.0 \times 10^{-16}. \tag{2.46}$$

2.7.1 Evaluation of the stiffness and damping matrices

The stiffness and damping matrices appearing in Eq. (2.44), result from the linearisation of the residual vector for a given iteration (i) and a single element e and read:

$$\mathbf{K}_{\mathrm{e}}^{(i)} = \sum_{k=1}^{\mathrm{nnd}} w_k \mathbf{B}(\boldsymbol{\xi}_{\mathrm{G},k})^{\mathsf{T}}\mathbf{Q}^{\mathsf{T}}\mathbb{K}_k\,\mathbf{Q}\,\mathbf{B}\,j_{\mathrm{e}}(\boldsymbol{\xi}_{\mathrm{G},k}), \tag{2.47a}$$

$$\mathbf{C}_{\mathrm{e}}^{(i)} = \sum_{k=1}^{\mathrm{nnd}} w_k \mathbf{B}(\boldsymbol{\xi}_{\mathrm{G},k})^{\mathsf{T}}\mathbf{Q}^{\mathsf{T}}\mathbb{C}_k\,\mathbf{Q}\,\mathbf{B}\,j_{\mathrm{e}}(\boldsymbol{\xi}_{\mathrm{G},k}), \tag{2.47b}$$

where $\mathbb{K}$ and $\mathbb{C}$ are the linearised interface constitutive matrices coming from the differentiation of the interface traction vector $\mathbf{p}$ with respect to

the field variables, after the application of a chain differentiation with respect to the gap field and recalling Eq. (2.20):

$$\frac{\partial \mathbf{p}(\mathbf{u},\dot{\mathbf{u}})}{\partial \mathbf{u}} = \frac{\partial \mathbf{p}(\mathbf{u},\dot{\mathbf{u}})}{\partial \mathbf{g}}\frac{\partial \mathbf{g}}{\partial \mathbf{u}} = \mathbb{K}\mathbf{Q}\mathbf{B}, \tag{2.48a}$$

$$\frac{\partial \mathbf{p}(\mathbf{u},\dot{\mathbf{u}})}{\partial \dot{\mathbf{u}}} = \frac{\partial \mathbf{p}(\mathbf{u},\dot{\mathbf{u}})}{\partial \dot{\mathbf{g}}}\frac{\partial \dot{\mathbf{g}}}{\partial \dot{\mathbf{u}}} = \mathbb{C}\mathbf{Q}\mathbf{B}. \tag{2.48b}$$

$2D$ formulation

In the $2D$ formulation, the above operators read:

$$\mathbb{K} = \begin{bmatrix} \dfrac{\partial p_\tau}{\partial g_\tau} & \dfrac{\partial p_\tau}{\partial g_{\mathrm{n}}} \\ \dfrac{\partial p_{\mathrm{n}}}{\partial g_\tau} & \dfrac{\partial p_{\mathrm{n}}}{\partial g_{\mathrm{n}}} \end{bmatrix}, \qquad \mathbb{C} = \begin{bmatrix} \dfrac{\partial p_\tau}{\partial \dot{g}_\tau} & \dfrac{\partial p_\tau}{\partial \dot{g}_{\mathrm{n}}} \\ \dfrac{\partial p_{\mathrm{n}}}{\partial \dot{g}_\tau} & \dfrac{\partial p_{\mathrm{n}}}{\partial \dot{g}_{\mathrm{n}}} \end{bmatrix}, \tag{2.49}$$

where $\mathbb{K}$ and $\mathbb{C}$ are derived by analytical differentiation if contact is detected, while on the other hand, every term of the matrices is set equal to zero if a positive g_{n}, *i.e.* an opening gap, is detected. In contact, they read:

$$\mathbb{K} = \begin{bmatrix} 0 & \mu\varepsilon_{\mathrm{n}} \tanh\left(\frac{\dot{g}_\tau}{\dot{\varepsilon}_\tau}\right) \\ 0 & \mu\varepsilon_{\mathrm{n}} \end{bmatrix}, \qquad \mathbb{C} = \begin{bmatrix} \frac{\mu p_{\mathrm{n}}}{\dot{\varepsilon}_\tau} \operatorname{sech}^2\left(\frac{\dot{g}_\tau}{\dot{\varepsilon}_\tau}\right) & 0 \\ 0 & 0 \end{bmatrix}. \tag{2.50}$$

3D formulation

In this case, $\mathbf{R}_\Gamma(\hat{\mathbf{u}}_{\mathrm{e}}, \hat{\dot{\mathbf{u}}}_{\mathrm{e}})$ can be derived in the same exact way with respect to the former 2D case, provided that the constitutive matrices $\mathbb{K}$ and $\mathbb{C}$ are suitably modified in accordance with the new expression for the regularised friction law, that results in a tangent vector $\mathbf{q}_\tau$ whose projections along directions 1 and 2 are:

$$q_{\tau 1} = -\mu|p_{\mathrm{n}}|\frac{\dot{g}_{\tau 1}}{\|\dot{\mathbf{g}}_\tau\|}\tanh\frac{\|\dot{\mathbf{g}}_\tau\|}{\dot{\varepsilon}_\tau}, \tag{2.51a}$$

$$q_{\tau 2} = -\mu|p_{\mathrm{n}}|\frac{\dot{g}_{\tau 2}}{\|\dot{\mathbf{g}}_\tau\|}\tanh\frac{\|\dot{\mathbf{g}}_\tau\|}{\dot{\varepsilon}_\tau}, \tag{2.51b}$$

while the expression for the normal traction p_{n} is identical with respect to the $2D$ formulation. By definition, the constitutive matrices are:

$$\mathbb{K} = \begin{bmatrix} \dfrac{\partial p_{\tau 1}}{\partial g_{\tau 1}} & \dfrac{\partial p_{\tau 1}}{\partial g_{\tau 2}} & \dfrac{\partial p_{\tau 1}}{\partial g_{\mathrm{n}}} \\ \dfrac{\partial p_{\tau 2}}{\partial g_{\tau 1}} & \dfrac{\partial p_{\tau 2}}{\partial g_{\tau 2}} & \dfrac{\partial p_{\tau 2}}{\partial g_{\mathrm{n}}} \\ \dfrac{\partial p_{\mathrm{n}}}{\partial g_{\tau 1}} & \dfrac{\partial p_{\mathrm{n}}}{\partial g_{\tau 2}} & \dfrac{\partial p_{\mathrm{n}}}{\partial g_{\mathrm{n}}} \end{bmatrix}, \quad \mathbb{C} = \begin{bmatrix} \dfrac{\partial p_{\tau 1}}{\partial \dot{g}_{\tau 1}} & \dfrac{\partial p_{\tau 1}}{\partial \dot{g}_{\tau 2}} & \dfrac{\partial p_{\tau 1}}{\partial \dot{g}_{\mathrm{n}}} \\ \dfrac{\partial p_{\tau 2}}{\partial \dot{g}_{\tau 1}} & \dfrac{\partial p_{\tau 2}}{\partial \dot{g}_{\tau 2}} & \dfrac{\partial p_{\tau 2}}{\partial \dot{g}_{\mathrm{n}}} \\ \dfrac{\partial p_{\mathrm{n}}}{\partial \dot{g}_{\tau 1}} & \dfrac{\partial p_{\mathrm{n}}}{\partial \dot{g}_{\tau 2}} & \dfrac{\partial p_{\mathrm{n}}}{\partial \dot{g}_{\mathrm{n}}} \end{bmatrix}. \tag{2.52a}$$

Their components can be derived by analytic differentiation. The only non-zero elements of $\mathbb{K}$ occupy the last column of the matrix and read:

$$\mathbb{K}_{1,3} = -\mu\, \varepsilon_{\mathrm{n}} \cos\vartheta_{\mathrm{v}} \tanh \frac{\rho_{\mathrm{v}}}{\dot{\varepsilon}_{\tau}}, \tag{2.53a}$$

$$\mathbb{K}_{2,3} = -\mu\, \varepsilon_{\mathrm{n}} \sin\vartheta_{\mathrm{v}} \tanh \frac{\rho_{\mathrm{v}}}{\dot{\varepsilon}_{\tau}}, \tag{2.53b}$$

$$\mathbb{K}_{3,3} = \varepsilon_{\mathrm{n}}, \tag{2.53c}$$

$$\tag{2.53d}$$

where the slip velocity has been expressed through the polar coordinates:

$$\rho_{\mathrm{v}} = \|\dot{\mathbf{g}}_{\tau}\|, \tag{2.54a}$$

$$\vartheta_{\mathrm{v}} = \tan^{-1} \frac{\dot{g}_{\tau 2}}{\dot{g}_{\tau 1}}. \tag{2.54b}$$

The elements of the damping matrix $\mathbb{C}$ which are different from zero are localised in the 2×2 top-left sub-matrix, since no dependency is present between the interface constitutive law and the velocity of the normal compenetration, nor between normal tractions and tangential slip. The

components can be written as:

$$\mathbb{C}_{1,1} = -\mu|p_{\mathrm{n}}|\left[\frac{1}{\rho_{\mathrm{v}}}\tanh\frac{\rho_{\mathrm{v}}}{\dot{\varepsilon}_{\tau}}\sin^2\vartheta_{\mathrm{v}} + \frac{1}{\dot{\varepsilon}_{\tau}}\left(1-\tanh^2\frac{\rho_{\mathrm{v}}}{\dot{\varepsilon}_{\tau}}\right)\cos^2\vartheta_{\mathrm{v}}\right], \tag{2.55a}$$

$$\mathbb{C}_{2,2} = -\mu|p_{\mathrm{n}}|\left[\frac{1}{\rho_{\mathrm{v}}}\tanh\frac{\rho_{\mathrm{v}}}{\dot{\varepsilon}_{\tau}}\cos^2\vartheta_{\mathrm{v}} + \frac{1}{\dot{\varepsilon}_{\tau}}\left(1-\tanh^2\frac{\rho_{\mathrm{v}}}{\dot{\varepsilon}_{\tau}}\right)\sin^2\vartheta_{\mathrm{v}}\right], \tag{2.55b}$$

$$\mathbb{C}_{1,2} = +\mu|p_{\mathrm{n}}|\sin\vartheta_{\mathrm{v}}\cos\vartheta_{\mathrm{v}}\left[\frac{1}{\rho_{\mathrm{v}}}\tanh\frac{\rho_{\mathrm{v}}}{\dot{\varepsilon}_{\tau}} - \frac{1}{\dot{\varepsilon}_{\tau}}\left(1-\tanh^2\frac{\rho_{\mathrm{v}}}{\dot{\varepsilon}_{\tau}}\right)\right], \tag{2.55c}$$

$$\mathbb{C}_{2,1} = \mathbb{C}_{1,2}. \tag{2.55d}$$

Care should be taken in the related code implementation since now, unlike the 2D case, the matrix would result undetermined for a null slip velocity. In the element implementation this last case must be treated separately, but taking the limit of $\mathbb{C}$ for $\rho_{\mathrm{v}} \to 0$ a removable discontinuity can be identified, resulting in:

$$\mathbb{C}_{1,1} = -\frac{\mu|p_{\mathrm{n}}|}{\dot{\varepsilon}_{\tau}}, \qquad \mathbb{C}_{1,2} = 0, \tag{2.56}$$

$$\mathbb{C}_{2,1} = 0, \qquad \mathbb{C}_{2,2} = -\frac{\mu|p_{\mathrm{n}}|}{\dot{\varepsilon}_{\tau}}. \tag{2.57}$$

2.8 Conclusions

In this Chapter, the general framework for an interface finite element has been derived. It can be directly applied to investigate elastic bodies' contact response under small deformation and conformal contact hypotheses. In the next chapters, the element properties are going to be enriched with innovative features. In Ch. 3, a suitable modification of the normal gap will be introduced, thus allowing for the simulation of the non-conformal contact between a deformable bulk and a rigid indenter characterised by an arbitrarily complex shape, without the need of explicitly discretising the complex boundary, as firstly addressed by Paggi and Reinoso [79]. Later on, in Ch. 4, a *multi-scale* approach is explored

for simulating the contact of the deformable bulk with a rough rigid indenter. For doing so, a scale separation is introduced. At the *micro-scale*, a boundary element algorithm is used for exactly evaluating a contact pressure field, which is homogenised and exploited at the *macro-scale* as a non-linear contact law, following an approach introduced by Zavarise et al. [80].

Chapter 3

Analysis of fully coupled normal and tangential contact problems with complex interfaces

In this chapter, an extension of the interface finite element derived in Ch. 2 is proposed for solving the normal and tangential contact problem between a rigid indenter of complex shape and an elastic body under generic load conditions. The indenter's actual shape is accounted as a correction of the local normal gap field $g_{\mathrm{lc,n}}$. The model is validated in relation to challenging scenarios for standard finite element procedures and analytical methods, such as the contact with *wavy* or *rough* profiles.

The original concept has been presented by Paggi and Reinoso [79] for frictionless contact, while the results derived in the current chapter, related to the accounting of friction, are presented in [56]. The present framework makes it possible to investigate the response of the system to tangential tractions, which is at the origin of important phenomena such as wear and fretting fatigue, together with the analysis of the effects of coupling between normal and tangential contact tractions, which is here investigated concerning challenging physical problems involving

arbitrary loading histories. The proposed approach is detailed in Sec. 3.1, while its validation is carried out in Sec. 3.2, against the analytic solution of the Westergaard problem [81] and a Hertzian contact problem obtained assuming the semi-coupling hypothesis between the normal and the tangential directions under different load scenarios [82]. In Sec. 3.3, the method is exploited to solve cases where no analytical solutions are available and particularly challenging according to standard finite element techniques. In particular, coupled normal and tangential frictional contact problems with indenters characterised by Weierstrass profiles as boundary and an increasing number of length scales, representative of multi-scale waviness, are investigated, and results are given in terms of the resulting interface tractions field. In conclusion of the chapter, a frictionless contact problem involving the contact of a self-affine rough profile against an elastic layer is solved. Its solution compared to the results of the same problem solved exploiting a BEM routine. Good accordance between the two sets of result is observed.

3.1 Interface finite element with embedded rough profiles

The proposed approach's innovation lies in an alternative definition of the normal gap $g_{\mathrm{lc,n}}$. In this framework, regardless of the actual topology, the contact interface is assumed to be *nominally smooth*, with uniquely defined normal and tangential unit vectors. In contrast, its exact height field distribution is analytically taken into account as a correction to the normal gap function. From the technical point of view, this could be the case of two profiles in contact which share a complementary *form* (or *lay*), but differ in terms of *waviness* and *roughness*, where the definition of these three quantities is made in accordance with standard surface metrology arguments, see for example "Filtering in the Frequency Domain" [83], Raja, Muralikrishnan, and Fu [84], De Chiffre et al. [85] and *Surface Texture (Surface Roughness, Waviness, and Lay)* [86].

3.1.1 Nominally flat rough indenter pressed against a deformable bulk

The method could be applied to the analysis of a deformable layer with a flat interface that makes contact with a nominally flat rough rigid surface, i.e. a rough surface with an overall flat *form*. This is the case, for example, of a nominally flat surface characterised by roughness at the micro-scale, Fig. 8a. The idea behind the proposed approach consists of defining an equivalent framework in which the contact problem's relevant features can be maintained without explicitly modelling the related geometric complexities. Let us assume that at $t = 0$ the two bodies make contact without exchanging any contact force. A *datum* is set in correspondence of the lowest point of elevation of the rough profile measured from a zero reference value, coincident with the flat boundary. An opposite equivalent flat boundary is set at a distance from the datum point equal to the root mean square elevation σ of the rough profile, dash-dotted line of Fig. 8a, measured from the datum. Finally, the height field

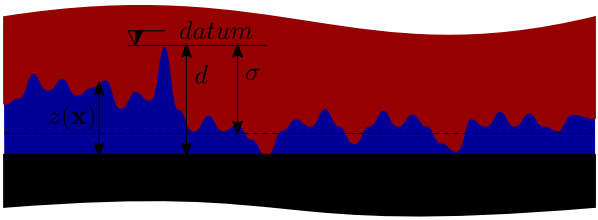

(a) Actual rough contact.

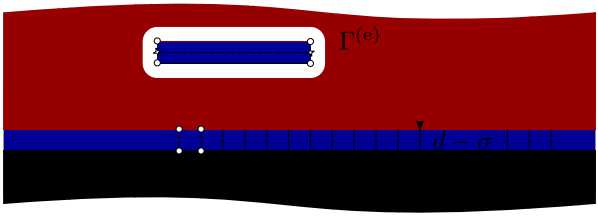

(b) Equivalent FE interface.

Figure 8: Interface discretisation with embedded roughness.

$z(x)$ is measured from the reference flat plane and stored. Starting from this data, an equivalent FEM approximation of the problem can be constructed, Fig. 8b. The two flat boundaries can be linked by a set of interface finite elements Γ, with an equivalent depth defined by $d - \sigma$. The height field can be represented in its isoparametric form as:

$$z(x) \approx \bigcup_{e=1}^{n_\Gamma} \tilde{z}_e(\boldsymbol{\xi}) = \bigcup_{e=1}^{n_\Gamma} \sum_{k=1}^{n_{\mathrm{nd}}} N_k(\boldsymbol{\xi}) \hat{z}_{e,k}. \tag{3.1}$$

The value of $\tilde{z}_e(\boldsymbol{\xi})$ can be used to correct the local gap associated with the equivalent flat boundary, to restore its exact variation from planarity without the need of explicitly discretising the actual complex morphology, cfr. Eq. (2.20):

$$\tilde{\mathbf{g}}^*_{\mathrm{lc,e}} = \mathbf{Q}\mathbf{B}(\boldsymbol{\xi})\hat{\mathbf{u}}_{\mathrm{e}} + [0,\, \tilde{z}_e(\boldsymbol{\xi})]^{\mathsf{T}}. \tag{3.2}$$

The number of interface elements that are necessary to discretise the rough profile properly is directly dependent on its morphology. The use of linear interpolating shape functions implies a bijective correspondence between a sampled height in the original profile and a nodal-wise gap correction in the FEM discretisation of the equivalent flat interface. According to this remark, the number of interface elements n_Γ employed should be high enough to guarantee that the related rough surface heights sampling has the appropriate resolution level to capture all the profile's relevant geometric characteristics.

3.1.2 Curved rough indenter over deformable bulk

The same underlying idea can also be extended to curved surfaces contact, provided that the two boundaries still share an overall common form. If, for example, the conformal shape is cylindrical, a datum can be set in correspondence of the rough profile point closest to the centre of the cylinder, Fig. 9a. The root means square radius R_σ can be evaluated through, for example, a standard least-squares minimisation. The elevation field can then be mapped using a suitable curvilinear abscissa s, with $z[\mathbf{x}(s)]$ evaluated along the normal $\mathbf{n}(s)$ of the curve that describes

the boundary of $\mathcal{B}_1$. The same requirement already stated for the former case also applies to this context for what concerns the number of interface elements to be employed. Additionally, n_Γ must also be high enough to have $R \gg L_\mathrm{e}$, being L_e the interface element length and R the radius of the cylinder, or, in general, the local radius of curvature of the interface lay. Which of these two conditions is stricter is problem-specific, depending on the ratios between the local radius of curvature of the rough profile R_p and the local radius of curvature of the interface form R_i. Fig. 10 shows the two opposite extremes we might have when two rough profiles with a *overall* complementary curved shape make contact over the

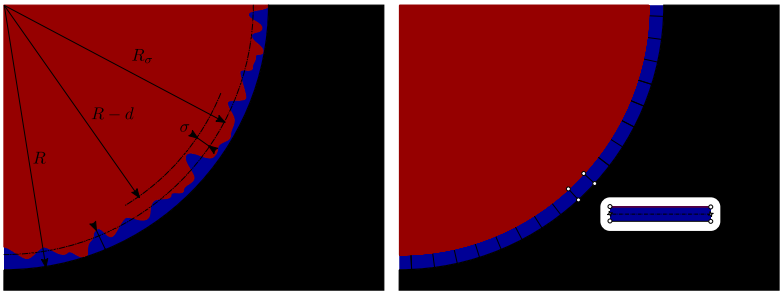

(a) Contact on a curved interface. **(b)** Equivalent FE interface.

Figure 9: Framework for curved rough contact.

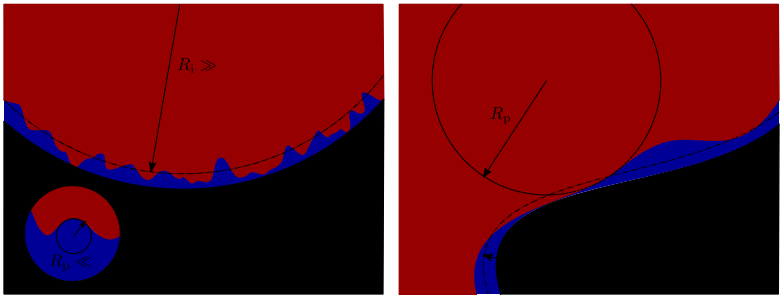

(a) Low ratio $R_\mathrm{p}/R_\mathrm{i}$. **(b)** High ratio $R_\mathrm{p}/R_\mathrm{i}$.

Figure 10: Distinct cases driving interface discretisation resolution.

curved side. Again the problem can be recast considering an equivalent simplified mesh discretisation with an embedded elevation field. The limit conditions can be distinguished as:

- a contacting profile with an almost flat interface and a very rough profile, in this case, we have $R_\mathrm{p}/R_\mathrm{i} \ll 1$ and the interface discretisation refinement is ruled by the rough profile, Fig. 10a;
- an interface with a small radius of curvature and an only mildly wavy profile, in this case might result $R_\mathrm{p} \sim R_\mathrm{i}$ and the discretisation of the wavy profile alone, filtered from the interface curvature, would not require a fine discretisation, which is nevertheless demanded by the interface curvature, Fig. 10b.

The proposed approach could, indeed, treat this second instance. In this case, an opportunity analysis should be carried out concerning the use of a standard full discretisation of the contacting bodies, which in this case would not be too demanding.

3.1.3 The Composite Topography

The instance presented in Sec. 3.1.1 can be regarded as the reformulation of a broader class of problems. Let us assume to have two linear elastic isotropic bodies in contact under the hypotheses of half-space approximation, each of them characterised by a camplex or rough boundary. Since the contact constraints only involve the relative vertical displacements of the two bodies, and the normal tractions exchanged are equal and opposite for $\mathcal{B}_1$ and $\mathcal{B}_2$, the elasticity equation related to a single contact spot could be expressed as:

$$v_1 - v_2 = \left(\frac{1-\nu_1^2}{E_1} + \frac{1-\nu_2^2}{E_2} \right) \frac{P}{\pi r}, \tag{3.3}$$

where v_i is the vertical displacement of the interface, r is the radial distance from the contact spot, P the force exerted, and E_i and ν_i are the Young's modulus and Poisson's ratio of the two bodies. Given that, the problem is equivalent to consider $\mathcal{B}_2$ rigid and $\mathcal{B}_1$ characterised by the

composite elastic Young's and shear moduli E and G, and by the composite Poisson's ratio ν:

$$\frac{1-\nu^2}{E} = \frac{1-\nu_1^2}{E_1} + \frac{1-\nu_2^2}{E_2}, \tag{3.4a}$$

$$\frac{1-2\nu}{4G} = \frac{1-2\nu_1}{4G_1} - \frac{1-2\nu_2}{4G_2}, \tag{3.4b}$$

where $G = E/[2(1+\nu)]$. Thanks to the hypothesis of half space approximation, also the contacting geometry can be simplified. After the re-cast of the problem mechanical properties, the situation is depicted in Fig. 11a. A zero reference can be placed in correspondence of the lowest valley of $\partial\mathcal{B}_1$, and an equivalent flat interface $\partial\mathcal{B}_1^*$ can be set in correspondence of the root mean square σ_1 of the elevation field. The resulting composite rigid profile $\partial\mathcal{B}_2^*$ can be evaluated as $z(\mathbf{x}) = d - [h_1(\mathbf{x}) + h_2(\mathbf{x})]$, where $h_1(\mathbf{x})$ and $h_2(\mathbf{x})$ are the normal distances measured from the reference points of $\partial\mathcal{B}_1$ and $\partial\mathcal{B}_2$.

In this way, the case treated in Sec. 3.1.1 can be exactly recovered, cfr. Fig. 8a and Fig. 11b. The problem of the contact of two dissimilar isotropic elastic bodies with a boundary described by an arbitrary geometry has been re-cast in the simplified one of a rigid shape indenting an elastic bulk whose mechanical and geometric characteristics are inherited from the two original bodies: the geometry of the rigid indenter is a combination of the two original ones, and so are its elastic parameters.

3.1.4 Some considerations

- We operate under the hypothesis of small displacements, but the simplifications added are significant. There is no need for projection algorithms with the related criticalities, see e.g. Wriggers [42, Ch. 4, pag. 60].

- the approach is *node-to-node*, but extendible to other more general contact approaches, e.g. *node-to-segment*, provided that a suitable framework for the interface finite element is derived, see for example Paggi and Wriggers [65].

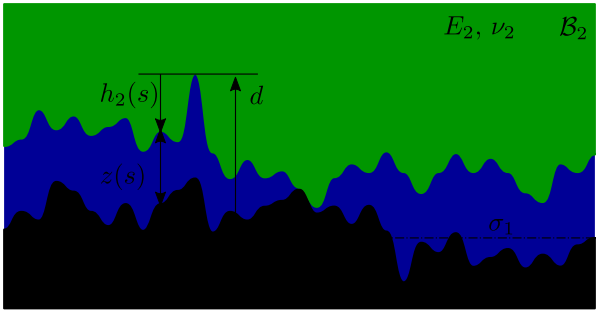

(a) Original configuration involving the contact of two elastic rough surfaces.

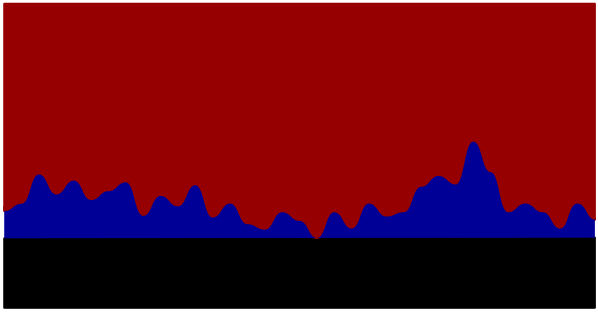

(b) Equivalent problem consisting in rigid-rough over flat-elastic contact.

Figure 11: Reformulation of the contact problem exploiting the concept of *composite topography*.

- The model can be easily be extended to take into account multi-physics phenomena invoking theorems that allow to draw analogies between the electrical and mechanical or thermal and mechanical fields, see, for example, Barber [87], Barber [88, Ch. 4, pag. 44-47], and Paggi and Barber [89]. The model is also suitable for investigating wear phenomena that can be considered considering degradation of the indenting profile determined by a selected wear law. Implementation that might easily be taken into account are the ones exposed, for example, in Andersson, Almqvist, and Larsson [90], Pinto et al. [91], Zhang, McHugh, and Leen [92], and McColl,

Ding, and Leen [93].

- The hypothesis of rigid to deformable contact can be relaxed. Both bodies can be considered deformable, provided that $z(\mathbf{x})$ is everywhere small compared to the bulks' characteristic dimensions. This would be equivalent to assuming that the profile's deformations are negligible concerning the bulks' deformations (since the profile shape is fixed). From the technical point of view, this assumption is justified by the empirical evidence that a rough boundary presents higher values of stiffness, in some cases several orders of magnitude, than the ones proper of the bulk, see for example Yovanovich, Devaal, and Hegazy [94] and Yovanovich, Hegazy, and Devaal [95].

3.2 Benchmark tests

In this section, the proposed approach is validated against reference solutions found in literature, specifically for the 2D version of the interface element with embedded roughness. While many closed-form solutions are readily available for frictionless contact, the scenario for coupled frictional problems is much more restricted.

3.2.1 The Westergaard problem

The framework is first validated against a frictionless problem, the contact of a rigid profile with a sinusoidal shape pressed against an elastic isotropic half-plane under the action of uniform pressure. The problem is known in the literature as Westergaard's problem [81] and the expression for the normal tractions distribution at the interface is given by:

$$p(x) = \frac{2\pi E g_0}{\lambda} \cos\left(\frac{\pi x}{\lambda}\right) \sqrt{\sin^2\left(\frac{\pi a}{\lambda}\right) - \sin^2\left(\frac{\pi x}{\lambda}\right)}, \tag{3.5}$$

where g_0 and λ are respectively the profile's amplitude and wavelength; E is the Young's modulus of the half-plane and a is the semi-width of a

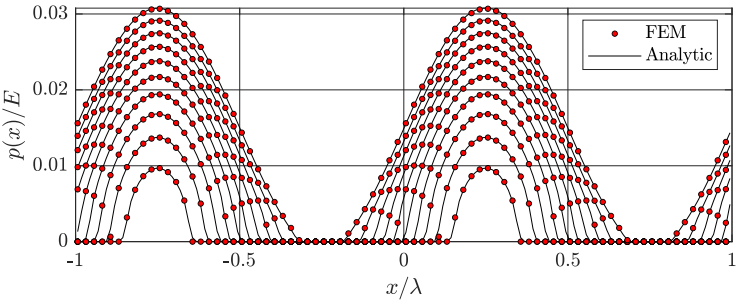

Figure 12: Comparison between the analytical solution given by Westergaard and the related FEM implementation for the frictionless indentation problem between a sine wave and a elastic isotropic half-plane

contact strip, implicitly given by a relation involving the uniform pressure p_0 applied to the indenter and the geometrical and mechanical properties of the system:

$$\sin^2\left(\frac{\pi a}{\lambda}\right) = \frac{p_0 \lambda}{\pi E g_0}. \tag{3.6}$$

Equation (3.5) is plotted in Fig. 12, together with results related to the equivalent problem solved with the proposed approach. The numerical simulation is performed under force control, applying a pressure linearly increasing with time up to a value correspondent to incipient full contact, a situation given by $p_0/E = 0.015$. A square block of side 2λ mimics the half-plane, meshed with standard bi-linear quadrilateral element. Periodic boundary conditions have been applied to the vertical sides of the mesh, while a perfect bond between the bottom side and a rigid boundary holds. The embedded profile is stored inside a single layer of interface finite elements, deployed over the upper side of the block and perfectly matching its boundary nodes. At the interface, $n_\Gamma = 128$ finite elements have been used to discretise the sine wave and store its elevation field, measured from the flat boundary of the half-plane. Since the attention is focused on the interface only, to obtain fast computational times, the mesh has been graded starting from the interface, changing its characteristic size h from $h = 2\lambda/n_\Gamma$ at the interface to $h = \lambda$ in corre-

spondence of the bottom.

3.2.2 Frictional Hertzian contact problem between a cylinder and a half-plane under a monotonic normal load

In order to assess the performance of the method concerning tangential tractions, a semi-coupled[*] Hertz contact problem is simulated. This benchmark is found to be particularly suitable for testing the validity of the proposed implementation for two specific reasons:

- despite its conceptual simplicity, the solution of this problem via a standard FEM discretisation of the curved geometry usually requires very refined meshes, especially at the edges of the contact strips;
- the present problem is characterised by a closed-form solution in terms of tangential tractions, thus providing an easy to implement and fast way of comparison and verification[†].

Analytical solution

For a given value of normal load and neglecting the influence of tangential tractions $q(x)$ on the normal contact traction distribution $p(x)$, the analytic solution can be written as [82]:

$$q(x) = \frac{\mu p_0}{K(c)} \left(\sqrt{1 - \frac{x^2}{a^2}} F(\theta, c) - \frac{x}{2b} \log \frac{1 - \sqrt{1 - x^2/b^2}}{1 + \sqrt{1 - x^2/b^2}} \right), \quad b \leq |x| \leq a, \tag{3.7}$$

where p_0 is the value of the vertical tractions, a and b are the extension of the contact radius and slip zone respectively, $c = b/a$, $\sin(\theta) = x/b$ and $K(c)$ and $F(\theta, c)$ are the first complete and incomplete elliptic integral of

[*]Hereinafter, the label *semi-coupled* will be referred to as a system in which the effect of the tangential tractions over the vertical pressure is neglected but not the opposite. This hypothesis has been introduced by Goodman [96].

[†]To the best of the author's knowledge, even under the hypothesis of semi-coupling, a closed-form solution in terms of tangential contact tractions can be found in literature only for the flat punch and for the Hertz problem, both under purely normal load.

the first kind, respectively. The extent of the slip zone can be evaluated using Spence's relation [97], which is valid for every initial contact gap defined by a power law relation, and is given by:

$$\mu K(c) = \beta K(\sqrt{1-c^2}), \tag{3.8}$$

where β is the second Dundurs' constant, expressed by:

$$\beta = \left(\frac{1-2\nu_1}{G_1} - \frac{1-2\nu_2}{G_2}\right) \Big/ \left[\frac{2(1-\nu_1)}{G_1} + \frac{2(1-\nu_2)}{G_2}\right] \tag{3.9}$$

This parameter governs the level of coupling of the system: for $\beta = 0$, the problem is uncoupled, while its maximum admissible value is 0.5, proper of the highest degree of coupling and related to $\nu = 0$, cfr. Eq. (3.9): in the limiting case of a contact problem involving a rigid parabolic profile (which is, as customary, the first-order approximation of a cylindrical shape) indenting an elastic half-plane, we have $\beta = (1 - 2\nu)/[2(1-\nu)]$, being ν the Poisson's ratio of the half-plane. A value of $\beta = 0.286$ is herein chosen, which corresponds to $\nu = 0.3$. While this value is kept constant, four different values for the friction coefficient have been used to investigate the accuracy of the model predictions. The comparison has been carried out in terms of normal and tangential tractions, exploiting Eq. (3.7) and comparing our fully coupled numerical approach with the semi-coupled analytical solution.

FEM implementation and results

In the present framework, the contact profile's actual shape is embedded in the interface finite element. The profile elevation is given by its analytical form and evaluated at every Newton-Cotes integration point. One of the contacting profile is flat, while the other is characterised by the expression $z(\mathbf{x}) = x^2/(2R)$. This defines a normal gap in the initial undeformed condition given by $g^*_{\mathrm{n,lc}} = z(\mathbf{x})$, being R the radius of the cylinder. We analyze the problem under plane strain assumptions. The mesh is structured on three different levels, Fig. 13:

- the lower models $\mathcal{B}_1$, which mimics a half-space approximated by a circular sector clamped along the curved side and free to undergo

vertical displacements in correspondence of the vertical boundary. An extension of its radius of $2R$ is enough for mimicking the elastic properties of a semi-infinite half-plane under plane strain assumptions. A Young's modulus $E_1 = 100\,\mathrm{Pa}$ and a Poisson's ratio $\nu_1 = 0.3$ have been assigned to the standard *quad* finite elements employed for the bulk discretization, to approach the semi-coupling condition proper of Eq. (3.7);

- the interface $\partial\mathcal{B}_{\mathrm{C}}^{*}$ is modelled using a single layer of $n_\Gamma = 100$ modified *quad* elements; the penalty stiffness has been set to $\varepsilon_{\mathrm{n}} = 10^2 E_1/R$, a value considered sufficiently high as to give an acceptable material compenetration.

- finally, the geometry of the indenting cylinder which represents $\mathcal{B}_2$ can be replaced by a regular array of standard *quad* linear finite elements, with an assigned elastic modulus $E_2 = 10^3 E_1$; Neumann boundary conditions are applied as a uniform distribution of vertical pressure p_0 resulting in a unitary vertical force N.

The problem is solved considering normal loading only, with the load

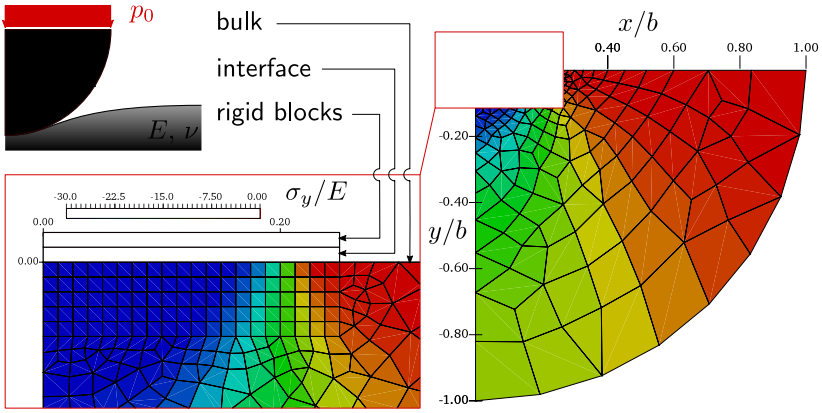

Figure 13: The actual geometry of the benchmark contact problem together with its finite element model, set up with the present approach based on the MPJR interface finite element.

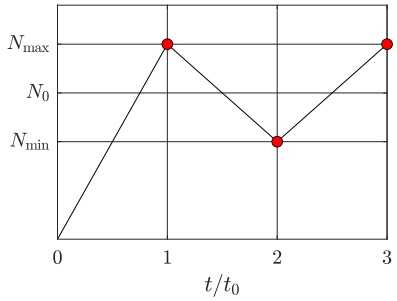

Figure 14: Load path chosen for the validation in presence of friction.

path plotted in Fig. 14. The results of the simulations are shown in Fig. 15a for $\beta = 0.286$, in terms of dimensionless tangential tractions $\sqrt{R/(EN_0)}q(x)/\mu$, where a_0 is the radius of contact related to the semi-coupled case. Results of Fig. 15a are related to the normal force N_0 belonging to the first branch of the loading path. Still, since they are self-similar in the case of a monotonic load path, they are valid for any other load level of the first branch of the loading path, provided that the correspondent value of N and a is prompted. For both the analytical semi-coupled and the FEM model, five different values of the coefficient of friction, $\mu = [0.1, 0.2, 0.3, 0.4, 0.5]$ are applied. The solution related to normal tractions is highlighted by circle markers only and not fully reported for graphical purposes. The interested reader is referred to [79] for a thorough analysis of the instance. For what concerns the tangential tractions, excellent accordance can be observed for all the coefficient of friction employed.

The coupling effect observed in the curve related to the numerical approach is in line with the theory, which predicts a stiffening effect that increases the maximum value of the tractions, compensated by a slight decrease of the contact radius. The deviation between the two sets of $q(x)$ that can be observed in Fig. 15a can be ascribed to coupling. The FEM model predicts smaller values for the ratio of b/a concerning the semi-coupled approach, and the effect can be quantitatively analysed, with

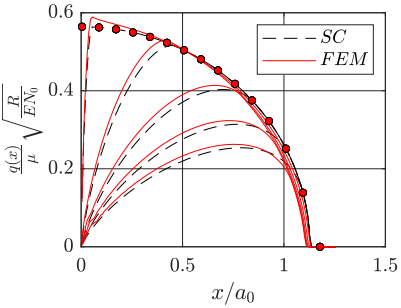

(a) Normal and tangential contact tractions.

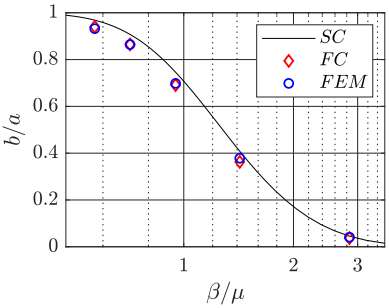

(b) Ratio between slip and stick contact strips width.

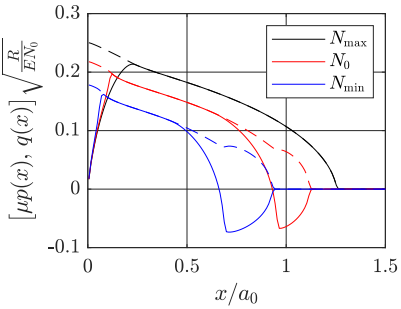

(c) Tangential tractions distribution at selected time steps of the unloading branch.

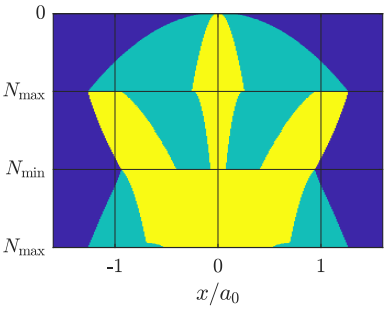

(d) Phase state diagram for the stick/slip regions.

Figure 15: Benchmark test with low values of coupling, $\beta = 0.286$.

results shown in Fig. 15b. In this figure, the black solid curve represents the values of b/a for the semi-coupled case, as expressed by Eq. (3.8), corresponding to the dashed black curves of Fig. 15a; the red diamonds mark the values for the fully coupled case, evaluated using an asymptotic solution provided in Nowell, Hills, and Sackfield [82] and the blue circles the outcomes of the simulation. Better accordance is found for the ratio b/a calculated in the fully coupled case. The deviation between the two sets of tangential tractions of Fig. 15a can be justified. The impor-

tance of the outcome of Fig. 15a lies in the fact that, for some specific instances, care should be taken in neglecting coupling effects since this could lead to underestimating the maximum magnitude of tractions. As a final remark, it can be noticed that even if a regularized friction law has been used, an adequate choice of the stiffness parameter $\dot{\varepsilon}_\tau$ guarantees results that are very close to the solution based on the Coulomb friction law, which the semi-analytical model has exploited.

Figure 15c shows numerical results related to the descending branch of the load path. This simulation have been performed with $\beta = 0.5$, $\mu = 0.2986$ and $N_{\min}/N_{\max} = 0.5$. These particular values have been chosen to match the results presented in [98], and provide a further means of comparison, even if only qualitative. The interested reader is referred to Fig. 4a and 4b of the reference for a confrontation. Finally, Fig. 15d shows a phase state diagram that reports the variation of the stick/slip domain during the whole loading path. Non-contact zones are shaded in dark blue, stick regions in yellow and slip regions in light blue. As the load increases from a null value up to $N_{\max}$, the contact area increases and two slip regions grows to encompass a central strip where a stick condition holds. As the load is reversed, the contact area recedes and two bands of stick form on the edge of the contact zone, growing as the normal load decreases, while the central one shrinks. As the load is rose again during the last loading branch, the increase in normal tractions is enough to instantly prevent any further slip and, for an instant, all the section sticks. After the turning point, new regions of slip start to grow in correspondence of the contact edge, reaching a maximum amplitude in correspondence of $N_{\max}$.

3.2.3 Hertzian contact problem between a cylinder and a half-plane under constant normal loading and cyclic tangential loading

Compared to the previous test problem, now a downward displacement is imposed on the cylinder, starting from zero and linearly increasing up to a maximum value of Δ_0. At this point, the vertical displacement

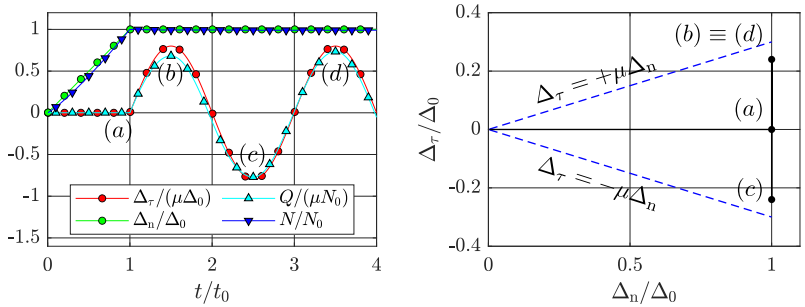

(a) Load in the $t\Delta$ space. **(b)** Load in the $\Delta_n\Delta_\tau$ space.

Figure 16: Tangential cycling load history.

is held constant, and a tangential load is applied, as a horizontal far-field displacement which harmonically oscillates with amplitude $\Delta_{\tau,0} = 0.8\mu\Delta_0$. A normalized load history plot is shown in Fig. 16a, together with the corresponding values of the total normal load N and tangential load Q, evaluated as the resultant of the interface tractions. The imposed displacements are also plotted in the load space $\Delta_n\Delta_\tau$, in which the black solid curve represents the variation of the tangential load concerning the normal one. At the same time, the blue dashed curves represent the limit of gross sliding. In the present case, the curve identifying the load path consists of a straight line lying on the horizontal axis, from the origin to point (a) and then becomes a collapsed ellipse with the major axis bounded by the points (b) and (c), Fig. 16b. The results in term of tractions distributions are shown in Fig. 17. In Fig. 17a, the normal load is linearly increased from zero to its maximum value. A self-similar symmetric central stick area encompassed by two regions of forwarding slip (positive tangential tractions) and backward slip (negative tangential tractions) develops. Then, Fig. 17b, the tangential load is applied (point (a) of Fig. 16a and 16b), which results in:

(i) an increase in the tangential tractions at the *leading* edge of contact;

(ii) a reduction of the tangential tractions at the *trailing* edge of contact;

(iii) a sudden change from backward slip to stick at the trailing edge, from which tractions start increasing again, but with opposite sign. Simultaneously, the stick zone shrinks, reaching its minimum at the point (b) of the loading history.

If the far-field displacement is now reversed, an instantaneous stick zone is created again. It shrinks to a minimum value in correspondence of point (c), Fig. 17c. The system reaches a stationary state condition after point (d), but with a steady-state value of the stick area, which is, for a positive load, sensibly different from the one related to the first application of the load Fig. 17d. It retains almost the same extension, but it is shifted towards the centre of the contact zone. As a final remark, the system maintains a significant difference between the positive and negative stick areas, even though the steady-state is reached after one loading cycle. It can be noticed that this is directly related to the level of coupling. The current results are obtained with a high level of coupling, corresponding to $\beta = 0.5$. The same load history, applied to a system with $\beta = 0.286$, shows a greater similarity between the positive and negative steady stick area, Fig. 18, showing again that the degree of coupling has an important effect on the contact response.

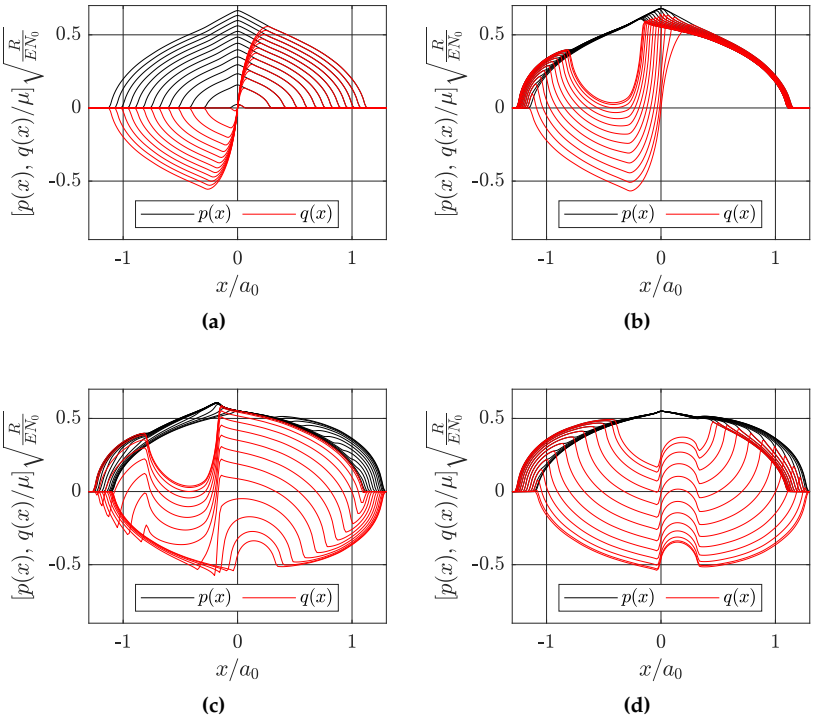

Figure 17: Tangential cycling load history for high values of coupling, $\beta = 0.50$.

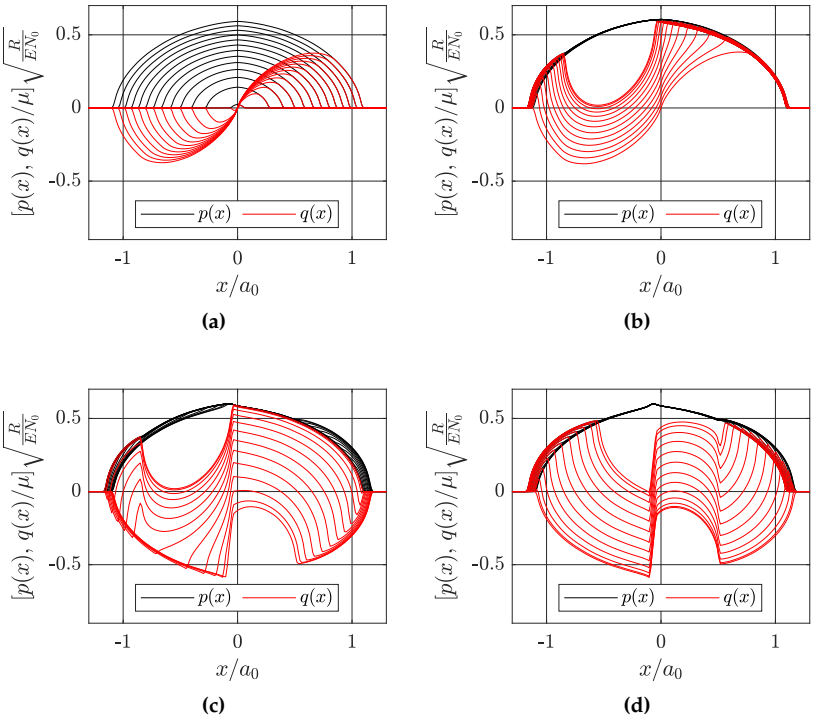

Figure 18: Tangential cycling load history for low values of coupling, $\beta = 0.286$.

3.3 Contact between a rough profile and an elastic layer

The capability of the proposed approach is now tested in the case of a more complex profile. The formulation's strength is particularly evident in contact problems involving profiles with complex shapes. Despite any elevation field might be taken into consideration in the computational framework, without any restriction, even rough profile or any numerically generated height field, a Weierstrass profile is herein used as a possible example. The height field is described by Eq. (5.2):

$$z(x) = g_0 \sum_{i=0}^{\infty} \gamma^{(D-2)i} \cos\left(2\pi \frac{\gamma^i x}{\lambda_0}\right), \tag{3.10}$$

wherein practical applications the summation is carried on up to a certain n_w, thus obtaining a *pre-fractal* profile (see for example Ciavarella et al. [99], and Ciavarella et al. [100]), which consists in the superposition of n_w sinusoidal functions, each of them presenting a decreasing wavelength $\lambda_i = \lambda_0/\gamma^i$ and amplitude $z_i = z_0\gamma^{(D-2)i}$, with $\gamma > 1$ and fractal dimension $1 \leq D \leq 2$.

In this section, four different indentation problems are solved with the aforementioned contacting profiles. Each of them is tested against a rectangular elastic block with a height-to-width ratio $h_\mathrm{b}/\lambda_0 = 1$. Such a bulk is characterised by the same elastic parameters employed for the model validation of Sec. 3.2, i.e. $E_1 = 100\,\mathrm{Pa}$ and $\nu_1 = 0.3$. Each indenter profile can be considered rigid and is made of the superposition of one, two, three and four terms, respectively, according to Eq. (5.2) and reported in Fig. 19. As in the previous section, the lower boundary, i.e. $\partial\mathcal{B}_1^*$, is flat, and the elevation field is coincident with a normal gap in the initial undeformed condition given by $g_{\mathrm{n,lc}}^* = z(x)$. Finally, to simulate a contact problem indefinite in the x direction, periodic boundary conditions have been applied to both the mesh's vertical edges at a distance of λ_0. A classical ironing-type load history is applied for solving the contact problem. First, a purely normal far-field displacement Δ_n is applied, starting from zero up to $\Delta_0 = 2g_0$. Then, a horizontal tangential dis-

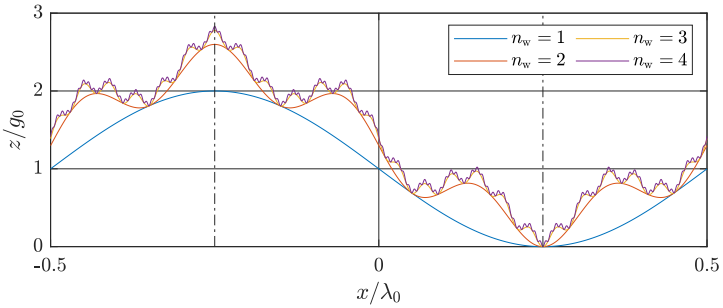

Figure 19: Weierstrass quasi-fractal multi-scale profile, characterised by $\gamma = 5$ and $H = 2 - D = 0.8$, unitary fundamental wavelength λ_0 and fundamental amplitude $g_0 = 10^{-2}\lambda$. In function of n_w, respectively 128, 512, 512 and 2500 interface finite elements have been employed in the meshing process for discretising each profile.

placement Δ_τ is applied, linearly varying from zero up to the maximum of $\Delta_{\tau,0} = 2\mu\Delta_0$, a value that guarantees an incipient gross slip for the single harmonics profile, given a friction coefficient $\mu = 0.2$. For what concerns the interface discretisation, the number of interface elements employed has been a function of the shortest wavelength employed. To adequately capture the profile's geometric features, at least 20 elements have been considered for modelling the shortest wavelength. This has resulted in a minimum number of interface finite elements employed in function of the number of terms in the Weierstrass series given by:

$$n_{\Gamma,\min} = 20\gamma^{n_w - 1} \tag{3.11}$$

A full parametric study of the problem should involve a thorough evaluation of the sensitivity of the system concerning the main governing physical parameters, such as β, μ, λ_0/h_b, g_0, γ, Δ_τ and Δ_n, but this is left for further investigation since the main purpose is to show the feasibility of treating complex interface problems within the present finite element framework.

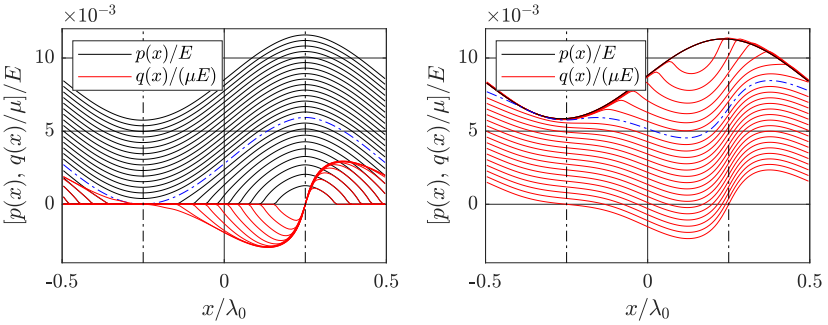

(a) Purely normal load stage

(b) Constant normal load, increasing tangential load stage

Figure 20: Ironing test, single harmonic profile.

3.3.1 Single harmonics profile in full contact

The case of $n_w = 0$ is shown in Fig. 20. The main difference with the results obtained for the previous Hertzian test problem is that now we are dealing with an infinitely long profile that makes contact at an infinite set of spots. Under purely normal loading, the vertical tractions $p(x)$ present two axes of symmetry, highlighted by the dash-dotted lines in the figure, which correspond to anti-symmetry axes for the shearing tractions $q(x)$. In each of these points, shearing tractions must be strictly null. They show the backward and forward slip zones typical of the Hertzian problem until the full contact condition is reached, which corresponds to a value of $p(x)$ highlighted by the blue dash-dotted curve in Fig. 20a.

After that point, a full stick condition holds, and $q(x)$ remains constant until the maximum value of the vertical far-field displacement is reached. After that point, the horizontal displacement is applied, and the tangential tractions grow until a condition of partial slip is reached; see the blue dotted line in Fig. 20b. As expected, the last point of the interface coming into contact is also the first one that undergoes partial slip. After this point, the system's state is such that there is an alternation of shrinking stick islands bordered by increasing zones of full slip. When the transient regime ends, a perfect overlapping between $\mu p(x)$ and $q(x)$

is observed.

3.3.2 Multiple harmonics profile contact

The addition of a length-scale in the Weierstrass function has the immediate effect of increasing the peak values of the normal tractions, which are localised in correspondence of the local maxima of the profile, and of reducing the contact area for a given level of the external load: the full contact condition is almost but completely achieved, see Fig. 21a. The same considerations on the tangential tractions distribution can also be made in this case, with the remark that now the contact domain is multiply-connected.

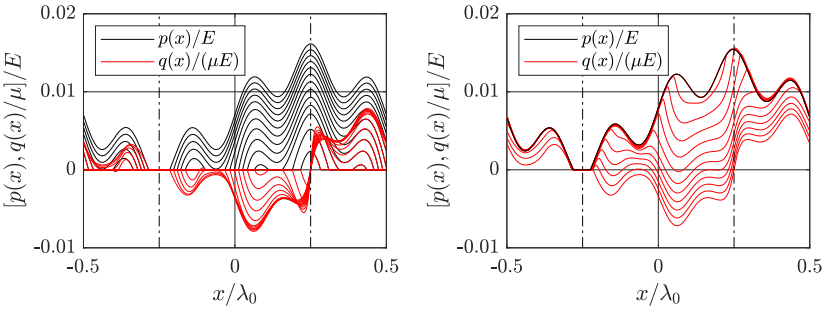

(a) Purely normal load stage

(b) Constant normal load, increasing tangential load stage

Figure 21: Ironing test for double harmonics profile.

In this case, an approximated study of $q(x)$ and of the extension of the stick and slip areas can still be possible, exploiting, e.g. the Ciavarella-Jäger theorem (Ciavarella [21], Ciavarella [22]), but under the limiting assumptions of uncoupling and half-plane approximation. An interesting feature that could be appreciated thanks to having taken into account coupling effects is that if under purely normal loading, two asperities, each of them generating a separate contact island, are characterised by a severe gradient in terms of vertical tractions, the less loaded one might experience a tangential tractions field which is very far from the typical

anti-symmetric distribution proper of an isolated asperity. If the vertical tractions in the leading asperity are high enough, the horizontal displacement generated by them might be so high compared to the ones generated by the secondary asperity that the latter is negligible, thus resulting in horizontal tractions which are all negative or positive valued from the beginning. With suitable boundary conditions or values of μ, there might also be a gross slip condition from the beginning of the contact process, Fig. 22a.

At the same time, when the second asperity comes into contact, it exerts a stiffening effect on the bulk, which reflects in a decrease of the magnitude of the increment rate of the horizontal displacements towards the high asperity, which in the final place determines a relaxing of the tangential tractions at the level of the leading asperity. This characteristic is depicted in Fig. 22a and 22b.

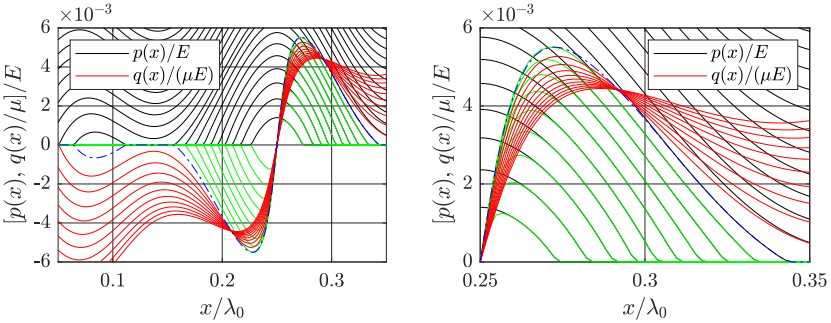

(a) The left contact island, highlighted by the blue dash-dotted line, comes in contact experiencing from the beginning a condition of full backward slip, a condition which can be appreciated thanks to the coupling effect.

(b) After the instant the second minor contact island comes in contact, the tangential tractions magnitude decreases, despite the applied normal load is still increasing.

Figure 22: Evolution of contact tractions.

The tangential tractions over the leading asperity, green curves, increase in extension and magnitude as long as the second asperity comes into contact, where they reach their maximum value, see the blue dash-

dotted line. After that moment, they continue growing in extension since the contact area is still increasing, but they decrease in magnitude due to the interaction between the different contact islands. Finally, when the tangential far-field displacement is applied, they start growing in magnitude again, gross slip starts, and the transition between full stick and full slip takes place, see Fig. 21b. The same trend can also be observed for the profile characterised by $n_{\mathrm{w}} = 2$, Fig. 23, where the same comments apply for the increase in vertical tractions, reducing the contact area and the evolution of the stick and slip zones. Finally, Fig. 24, the same problem is solved for $n_{\mathrm{w}} = 3$. In this final case, the reduction in the contact area is so high that it is limited to half the fundamental wavelength of the profile.

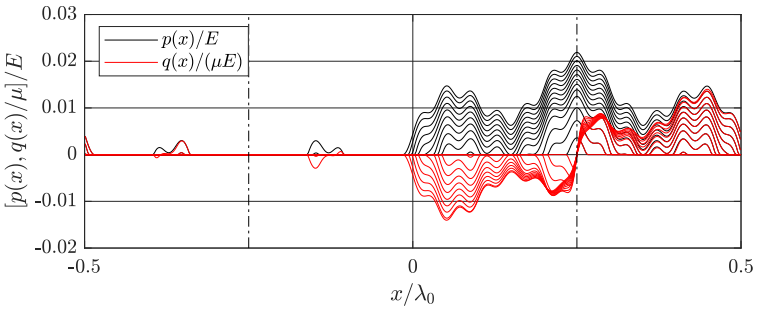

(a) Purely normal load stage

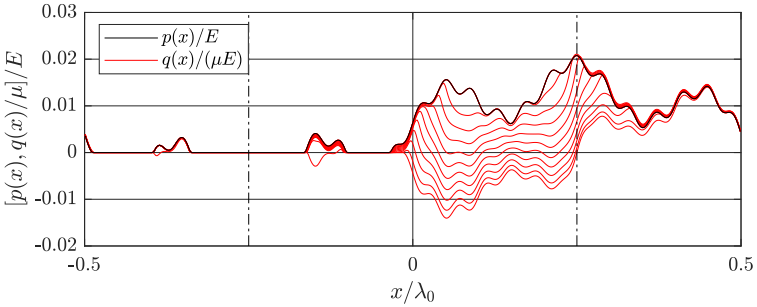

(b) Constant normal load, increasing tangential load stage

Figure 23: Ironing test for a double harmonics profile.

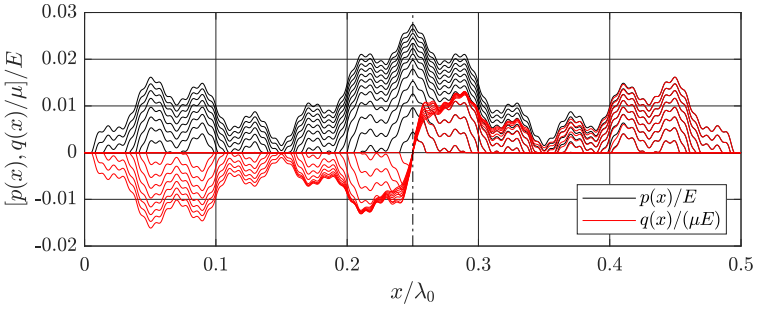

(a) Purely normal load stage

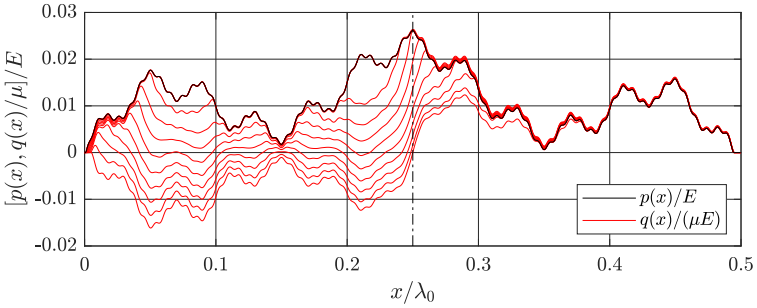

(b) Constant normal load, increasing tangential load stage

Figure 24: Ironing test for a triple harmonics profile.

3.4 Comparison with BEM

In conclusion of the chapter, a preliminary test against a self-affine rough profile is presented. The profile has been extracted from a rough surface in correspondence of its highest peak. The surface has been generated using a Random Midpoint Displacement algorithm (RMD), a numerical procedure employed to generate fractal rough surfaces with self-affine properties; see [89, 101] for more details. The parameters required by the generation algorithm are limited to the desired surface fractal dimension, in the present case $D = 2.2$; a random number, the grid lateral size $2b$ and a grid spacing δ, the last chosen to generate a height distribution of $N = 2049$ points equally spaced over a contact interface discretised with $n_\Gamma = N - 1$ interface finite elements. The obtained profile is considered the boundary of a rigid body acting over an elastic layer of finite depth, characterised by $E = 100\,\mathrm{Pa}$ and $\nu = 0$. The problem is solved under displacement control, applying a downward imposed displacement linearly increasing from zero up to the value of $\Delta_0 = 2g_0$, being g_0 the maximum height of the profile measured from its lowest valley. The shape of the profile can be appreciated in Fig. 25 (blue line), which also presents the solution in terms of surface displacements obtained both within the FEM framework, and a BEM algorithm specifically developed for the solution of a $2D$ plane-strain problem under displacement control. Good

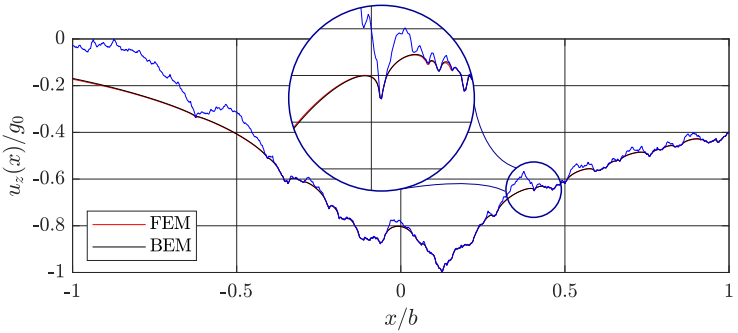

Figure 25: Indentation of the elastic frontier by the rigid profile.

agreement is observed between the two vertical displacement fields. A comparison is also made in terms of interface normal tractions $p(x)$, with results shown in Fig. 26. Here, the whole interface normal traction field is plotted for the last time step of the analysis. A general good accordance between the two different sets of results can be observed. If the attention is focused on the top-right magnified window, some scatter in the results can be observed. Still, given the very different assumptions underlying the two numerical frameworks, this preliminary result can surely be considered promising.

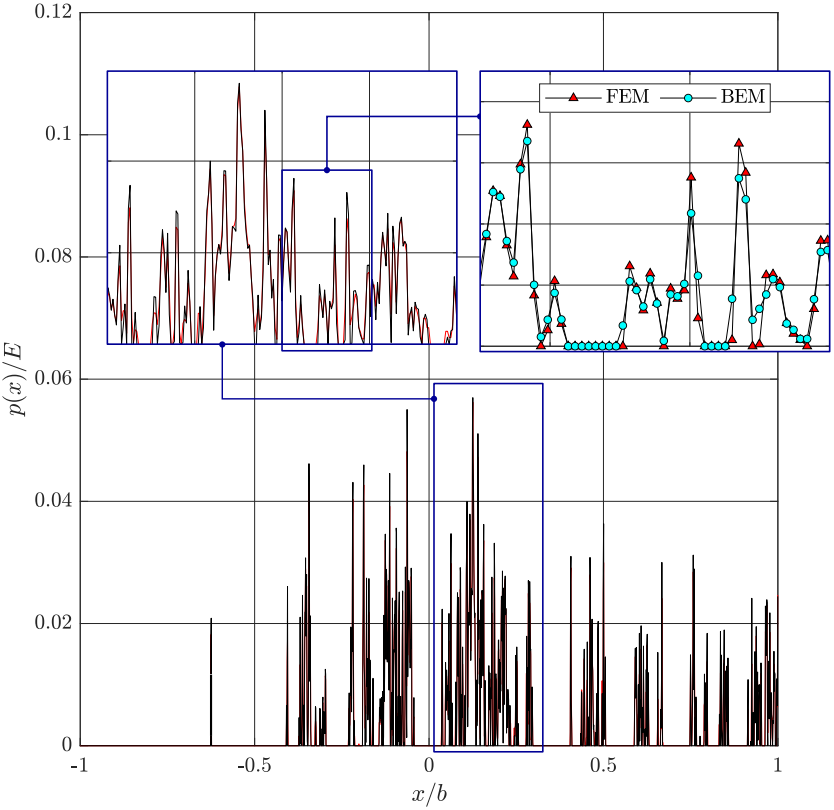

Figure 26: Resultant interface normal tractions field.

Chapter 4

A multi-scale FEM-BEM formulation for contact mechanics between rough surfaces

In this chapter, a *multi-scale* combined formulation for simulating contact between *nominally smooth* but *microscopically rough surfaces* is proposed. The approach integrates the interface finite element derived in Ch. 2 For modelling interface interactions at the *macro-scale* with the boundary element method (BEM) for the solution of the contact problem at the *micro-scale*. The use of BEM allows to exactly reconstruct the microscopic rough surface geometry, without the necessity to adopt interpolation techniques to discretise the interface, proper of FEM, which could lead to an undesired smoothing of the fine-scale roughness characteristics. On the other hand, the use of FEM permits to overcome some of the limitations proper of BEM, which is usually restricted to linear elastic isotropic materials and infinite geometries, with exceptions that are possible but not straightforward. The contents of this chapter are partially extracted from Bonari et al. [57].

4.1 General framework

The proposed method can solve the frictionless normal contact problem of a rigid rough indenter and a deformable body.*

If the rough surface's elevation field is small compared to the bulks' characteristic dimension, a separation of the two scales can be performed. This could be quantitatively assessed by comparing, for example, the root mean square σ of the rough surface, measured from its lowest point, with the deformable bulk's depth h_{b}, and imposing the condition:

$$(\sigma_{\mathrm{p}}, \sigma_{\mathrm{s}}) \ll h_{\mathrm{b}}, \tag{4.1}$$

where the subscripts p and s stand for *profile*, if a 2D problem is addressed, or *surface*, for the 3D case. If Eq. (4.1) holds, a macro-scale can be identified, consisting of the two bulks and the interface, which at this level is considered to be perfectly smooth. At the same time, at the micro-scale, the rough contact problem is restored. From the computational perspective, the problem is tackled using FEM at the macro-scale and BEM at the micro-scale. The coupling between the two different scales is enforced by the interface contact law, which is shared between the macro- and the micro-scale in terms of the compenetration function g_{n} and is used as input for the BEM routine. In turn, the traction field $p_\mu(\mathbf{x}_\mu)$, solution of the micro-scale problem is homogenised over the rough surface area and passed to the upper scale. At this level, the smooth interface is discretised using a set of the interface finite elements derived in Ch. 2. The tractions field $p_\mu(\mathbf{x}_\mu)$ defines the contact traction $p_{\mathrm{n}} = \langle p_\mu(\mathbf{x}_\mu) \rangle$, evaluated at the element's Gauß point, together with the related normal contact stiffness $\partial p_{\mathrm{n}} / \partial g_{\mathrm{n}}$.

The proposed pipeline characterises the method as a FE^2 approach, thus rather expensive concerning other multi-scale approaches exploiting pre-computed contact laws that rely on statistical models. In this regard, the interested reader is referred to Zavarise et al. [80] and Wriggers and Reinelt [102], where modified interface contact laws based on

*As pointed out in Sec. 3.1.3, this scenario could also be exploited, under suitable assumptions, for the solution of the contact problem of two elastic bodies, both characterised by a rough contact boundary.

micromechanical theories were proposed. These approaches involved a statistical representation of the micro-scale roughness. The presented framework allows for more versatility and accuracy since an actual rough geometry can be taken into account without any simplifying assumption. On the other hand, the computation cost associated with this problem is much higher than in the reference above. Therefore, some possible acceleration strategies are presented in Secs. 4.5.1, 4.5.2 and 4.5.3, and their effect compared.

An analogous approach can be found in Waddad et al. [103], but with a simplified semi-analytical approach for solving the problem at the micro-scale and without explicitly specifying the strategy followed in the derivation of the macro-scale system tangent matrix.

4.2 Micro-scale analysis

The unknown value of p_{n}[†] at each Gauss Point is herein computed by solving the normal contact problem of a rigid rough surface indenting an elastic half-space with suitable elastic parameters, using a BEM algorithm. The framework could directly assess a rigid-deformable contact problem *as is* or be seen as the recast of a contact problem involving two linear elastic isotropic bulks with rough contacting interfaces. In the latter case, both the resulting boundary geometries and the half-space elastic moduli must be regarded as composite quantities, i.e. functions of the geometric and mechanical parameters of the original problem, following the same procedure exposed in Sec. 3.1.3.

For each Gauß point of the interface elements, the following micro-scale contact problem is solved under displacement control, where the far-field displacement applied corresponds to $-g_{\mathrm{n}}$ from the macro-scale model. For $g_{\mathrm{n}} = 0$, we assume the surfaces touch only at the tallest height of the composite topography, with a resulting zero normal traction. For each $g_{\mathrm{n}} > 0$, a non-vanishing contact area has to be computed and the corresponding total normal force equivalent to the integral of the normal contact tractions obtained. To do so, the BEM implementation proposed

[†]Employing the same notation used in Ch. 2 is $p_{\mathrm{n}} = \tilde{p}^{e}_{\mathrm{n}}(\boldsymbol{\xi}_{G,k})$.

in Bemporad and Paggi [34] is employed. In particular, the *Warm-Started Non-Negative Least Squares (NNLS)* algorithm is exploited.

For a given far-field displacement g_{n} in the direction perpendicular to the half-space frontier, the solution of the normal contact problem in terms of vertical displacements $w_\mu(\mathbf{x}_\mu)$, and normal contact tractions $p_\mu(\mathbf{x}_\mu)$ must satisfy the convolution integral equation:

$$w_\mu(\mathbf{x}_\mu, g_{\mathrm{n}}) = \frac{1-\nu^2}{\pi E} \int_{\mathcal{S}} \frac{p_\mu(\mathbf{y}_\mu)}{\|\mathbf{x}_\mu - \mathbf{y}_\mu\|} \, \mathrm{d}\mathbf{y}_\mu, \tag{4.2}$$

where $\mathbf{x}_\mu$ and $\mathbf{y}_\mu$ represent, in a micro-scale Cartesian reference system, the coordinates at which displacements are evaluated and the points where a pressure is applied, respectively. Eq. (4.2) must be equipped with the unilateral Karush-Kuhn-Tucker (KKT) conditions:

$$w_\mu(\mathbf{x}_\mu, g_{\mathrm{n}}) \geq 0, \qquad p_\mu(\mathbf{x}_\mu) \geq 0, \qquad w_\mu(\mathbf{x}_\mu, g_{\mathrm{n}}) p_\mu(\mathbf{x}_\mu) = 0. \tag{4.3}$$

The set of equalities and inequalities above have already been introduced in Sec. 2.3.1. In contrast, a relaxation over this set of constraints has been performed at the macro-scale during the interface finite element's derivation. The contact problem is tackled rigorously by the BEM algorithm at the micro-scale through a related optimisation problem.

In Eq. (4.3), $w_\mu(\mathbf{x}_\mu, g_{\mathrm{n}}) = v_\mu(\mathbf{x}_\mu) - \bar{v}_\mu(\mathbf{x}_\mu, g_{\mathrm{n}})$, where $\bar{v}_\mu(\mathbf{x}_\mu, g_{\mathrm{n}})$ denotes the known indentation of the half-space at the points in contact. A $2D$ sketch is shown in Fig. 27, where the black solid line represents the elastic half-spaces deformed configuration corresponding to the imposed far-field displacement. The red dash-dotted line represents the rigid body motion of the elastic body under the imposed displacement. The solution of the contact problem determines three possible states for the rough indenter's peaks. They could be:

(a) not in contact from the beginning;

(b) losing contact due to elastic interactions;

(c) in contact after considering elastic interactions.

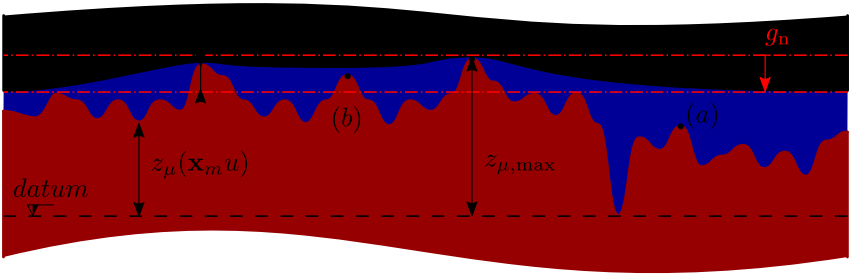

Figure 27: Contact sketch.

A routine for this continuous problem has been implemented by discretizing the rough surface with a square grid with lateral size l and resolution parameter n. The grid is composed of N^2 cells with $N = 2^n$ boundary elements per side. The lateral size of each boundary element is $\mathrm{d}x_{1,\mu} = \mathrm{d}x_{2,\mu} = l/2^n$. For the cases treated in the present chapter, a *random midpoint displacement* (RMD) algorithm has been used to generate the elevation field $z_\mu^{i,j}$, $(i,j) = [1,\ldots,N+1]$ of the selected rough surface, although any data field obtained from experiments can be used in the input, without any restriction, Fig. 28. For each microscopically rough surface, the mean elevation $\bar{z}_\mu$, the maximum elevation $z_{\mu,\max}$, and the root mean square roughness σ are also available from a preliminary sta-

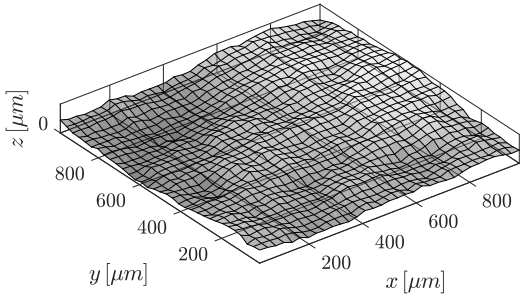

Figure 28: Example of a discretised rough surface. The input rough surface could be, without any restriction, analytical, numerical or only consist in a sampled height field, like profilometric data.

tistical characterization. The discretised matrix form of the problem thus reads:

$$\mathbf{w} + \bar{\mathbf{v}} = \mathbf{H}\mathbf{p}, \qquad \mathbf{w} \geq \mathbf{0}, \qquad \mathbf{p} \geq \mathbf{0}, \qquad \mathbf{w}^{\mathsf{T}}\mathbf{p} = 0, \tag{4.4}$$

where $\mathbf{w}$ is the vector of elastic corrections, $\mathbf{p}$ the unknown average contact forces, $\bar{\mathbf{v}}$ the vector of compenetrations and finally $\mathbf{H}$ the matrix collecting the compliance coefficients in its approximated form as derived in Love [29] with the notation borrowed from Pohrt and Li [37]:

$$H_{ij,kl} = \begin{cases} \frac{1}{\pi E} & \text{if } i = k \text{ and } j = l, \\ \frac{1}{\pi E} \arcsin \frac{1}{\|\mathbf{x}_\mu^{i,j} - \mathbf{x}_\mu^{k,l}\|} & \text{if } i \neq k,\, j \neq l, \end{cases} \tag{4.5}$$

Due to linear elasticity, $\mathbf{H}$ is symmetric and positive definite. This guarantees that the contact problem has a unique solution for any $g_{\mathrm{n}} \geq 0$. The problem corresponds to the conditions for optimality of the convex quadratic program:

$$\min_{\mathbf{p}} \ \frac{1}{2}\mathbf{p}^T\mathbf{H}\mathbf{p} - \bar{\mathbf{v}}^T\mathbf{p}, \qquad \text{s.t. } \mathbf{p} \geq \mathbf{0}. \tag{4.6}$$

4.3 Macro-scale analysis

The solution of Eq. (4.6) determines the evaluation of the contact area at the micro-scale, together with the distribution of the normal contact tractions $\mathbf{p}$. The final value to be passed to the macro-scale is evaluated as its mean value, $p_{\mathrm{n}} = \langle \mathbf{p} \rangle$, together with the related contact stiffness necessary for the evaluation of the tangent matrix $\mathbf{S}$, *cfr.* (2.7.1) and (2.7.1). At the macro-scale, the underlying difference concerning the derivation presented in Ch. 2 is that the normal contact traction is not linearly dependent on the penalty parameter ε_{n}. Still, it is evaluated according to the inner scale problem's solution, together with the required contact stiffness. This latter quantity requires a differentiation, and it can not be evaluated in a single shot. Different strategies for its evaluation will be treated in Sec. 4.5

4.4 Computation of the contact pressure related to roughness

The normal contact stiffness and the contact pressure predicted by the boundary element algorithm account for two separate effects: one associated with the surface's roughness, and another related to the deformation of the half-space, see for example Paggi and Barber [89]. The system's overall compliance results from the superposed effects related to the presence of roughness and the bulk elasticity.

In our framework, we need to extract only the effect of roughness since the surrounding continuum's elastic contribution is already computed in the macro-scale model. Therefore, a correction to the resulting pressure field is required. To this aim, as a preliminary step, we need to compute the elastic deformation associated with our micro-scale contact problem and subtract this contribution from the overall system.

If we consider the contact of a perfectly flat rigid indenter, with a $l \times l$ square size, acting on an elastic half-space under a vertical force P, an average uniform nominal pressure $\overline{p} = P/l^2$ will cause, under the contact area, a uniform vertical displacement w_0 equal to:

$$w_0(\overline{p}) = \alpha \frac{(1-\nu^2)}{E} \overline{p} l, \tag{4.7}$$

where α is a numerical coefficient. Its exact value can not be derived for a square punch, but different approaches for its approximate evaluation can be found in Galin [104], Conway and Farnham [105] and Barber [88, Ch. 4, pp. 48–50]. An accurate analysis permits us to conclude that an excellent approximation can be found simply considering the same relation for an indenter with a circular section and equivalent area, characterised by an analytical solution. This approach leads to $\alpha = 0.887$.

This value is reliable for a continuum. If the same problem is solved using a numerical approach, α will be influenced more and more as the level of accuracy decrease. In our case, it is dependent on the half-space boundary discretization, and to evaluate it for a given mesh resolution, different BEM simulations have been performed, each with a different number of square patches, all solving the problem of a perfectly flat rigid

indenter with square section acting on the half-space. Since such a model only includes linear elastic effects, the resulting displacement-pressure relation is linear. The shape factors obtained are given in Tab. 1 for different resolutions. Their expression read:

$$\alpha = \frac{E}{1-\nu^2}\frac{w_0}{l}\overline{p}. \tag{4.8}$$

Once the values are known for a given resolution level, we can use the relation between the nominal pressure and the elastic indentation given in Eq. (4.7) for computing the gap-pressure curve related to roughness only. This curve can be obtained by evaluating the values of the pressure $\overline{p}$ for a given set displacements $\bar{\Delta}$, considering both the elastic and the roughness contributions through the BEM and then applying (4.7) for computing the roughness related displacement $g_{\mathrm{n}} = \bar{\Delta} - w_0(\overline{p})$ in order to obtain the curve $\overline{p} = \overline{p}(g_{\mathrm{n}})$. The result of this correction procedure is graphically shown in Fig. 29, where we can notice that the identified roughness contribution (red curve) causes a stiffer response of the system concerning the one resulting from the overall system (blue curve). It is obtained by subtracting the elastic contribution (green line) from the numerical simulation's total curve. Conceptually, it is equivalent to assume that for a given level of indentation g_{n}, the correct value of $\overline{p}$ to be taken into account for considering only the effect of roughness corresponds to the one related to an imposed displacement of $g_{\mathrm{n}} + w_0(\overline{p})$, Fig. 29.

It must be underlined that this subtracting procedure is not directly applicable to the multi-scale model since it requires knowing *in advance* the evaluation of the *entire* pressure-gap curve without correction. At the same time, the macro-scale model provides the micro-scale model a single displacement g_{n} for each Newton-Raphson iteration, at each

n	1	2	3	4	5	6	7	8
α	0.778	0.806	0.826	0.841	0.852	0.858	0.862	0.865

Table 1: Values of the coefficient α computed by solving the problem of a rigid flat indenter in contact with an elastic half space with the BEM algorithm, for different values of the surface resolution parameter n

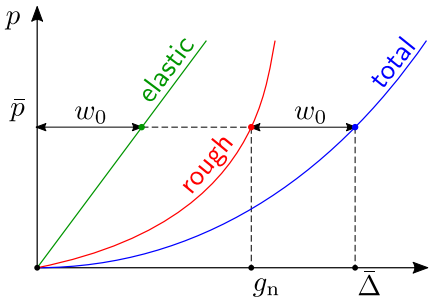

Figure 29: Qualitative representation of pressure vs. imposed displacement curve considering the elastic contribution, the roughness contribution, and their combined effect.

Gauß point, for each time step. Since g_n is meant to be related to roughness only, a pressure $\bar{p}$ higher than the one obtained by the unmodified curve must be found, accordingly to Fig. 30. The required value can be identified considering an augmented displacement $\bar{\Delta} = g_\mathrm{n} + w_0$ where the value of w_0 can not be evaluated directly, depending on the unknown pressure $\bar{p}$. A fixed point iterative scheme has served the purpose.

The BEM algorithm takes g_n as input from the macro-scale model and computes the related pressure $p^{(0)}(g_\mathrm{n})$, that allows for the computation of a tentative correction $w_0^{(0)}(\overline{p}^{(0)})$. The input displacement is then updated as $g_{\mathrm{n,c}}^{(1)} = g_\mathrm{n} + w_0^{(0)}$ and a new value of the pressure $\overline{p}^{(1)}$ is computed. The relative error on the average pressure is evaluated and eventually the procedure is repeated. At the i-th generic iteration, the corrected displacement reads:

$$g_{\mathrm{n,c}}^{(i)} = g_\mathrm{n} + w_0^{(i)}(\overline{p}^{(i)}) \tag{4.9}$$

corresponding to a pressure $\overline{p}^{(i)}$. The relative error between two subsequent iterations is updated, and the iterative procedure stops when the relative error is less than an imposed tolerance. The identified value of pressure is the required value $\bar{p}$ to be read by the macro-model at the Gauß point.

The tolerance value has been obtained after a convergence study: the iterative procedure has been tested for a set of imposed displacements,

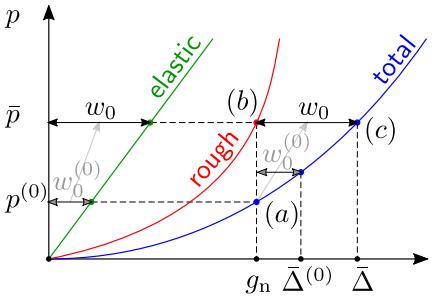

Figure 30: Since point (b) is not directly derivable in the element routine, starting from point (a) the iterative procedure evaluates the pressure in (c) which guarantees equilibrium between w_0, g_n and δ_c and gives the corrected pressure $\bar{p}$ related to g_n.

varying the value of the tolerance to achieve good accordance with the corrected gap-pressure curve evaluated with the subtracting procedure. As shown later in Sec. 4.6, perfect accordance has been found between the two curves even for a loose tolerance for all the values of separation taken into account, in line with the results shown in Ciavarella, Delfine, and Demelio [14] and Ciavarella, Greenwood, and Paggi [15].

4.5 Multi-scale coupling

The coupling between the micro- and the macro-scales has been implemented investigating three alternative approaches. Two of them foresee a total embedding of the boundary element algorithm inside the finite element routine. The third approach evaluates separately a pressure-displacement curve, which is then fitted with an analytical function in the last instance exploited at the macro-scale.

4.5.1 FBEM-QN

In the first approach, a full integration of FEM and BEM is proposed, hereinafter referred to as *FEM BEM Quasi-Newton* (FBEM-QN) since a numerical approximation of the Jacobian is used for the iterative solution

scheme. The interface finite element has been coded according to Ch. 2. At each time step and for each Gauß point, the contact pressure $p_{\mathrm{n}}(g_{\mathrm{n}})$ and the contact stiffness $\partial p_{\mathrm{n}}/\partial g_{\mathrm{n}}$ are computed by calling the BEM subroutine, embedded in the finite element routine. Such BEM subroutine reads the rough surface height field at the first time step from an input file (the height field is stored in a standard x, y, z three columns format) and saves it in a history variable for all the next time steps, to avoid continuous access to external files. The BEM subroutine is called once to compute p_{n} and then a second time to compute the normal contact stiffness via a finite difference approximation obtained by a perturbation of the initial value g_{n}:

$$\left[\frac{\partial p_{\mathrm{n}}}{\partial g_{\mathrm{n}}}\right]^{(k)} \simeq \frac{p_{\mathrm{n}}^{(k+1)} - p_{\mathrm{n}}^{(k)}}{g_{\mathrm{n}}^{(k+1)} - g_{\mathrm{n}}^{(k)}}, \tag{4.10}$$

where $g_{\mathrm{n}}^{(k)}$ is the far-field displacement of the macro-scale model for the current k-th Newton-Raphson iteration, and $g_{\mathrm{n}}^{(k+1)} = g_{\mathrm{n}}^{(k)} + \Delta g_{\mathrm{n}}^{(k)}$ is a small perturbation of its value, for which the pressure values $p_{\mathrm{n}}^{(k)}$ and $p_{\mathrm{n}}^{(k+1)}$ are computed by BEM.

4.5.2 FBEM-CQN

The approach presented is computationally demanding, and therefore a second methodology is also proposed for the numerical evaluation of the normal contact stiffness to save CPU time. In such an approach, referred to as *FEM BEM Cheap Quasi-Newton* (FBEM-CQN), the contact stiffness at the current Newton-Raphson iteration is computed using the displacement and the pressure corresponding to the previous converged time step as the reference values for the application of the finite difference formula. The procedure requires using Eq. (4.10) only at the first time step, and then the following equation is used subsequently:

$$\left[\frac{\partial p_{\mathrm{n}}}{\partial g_{\mathrm{n}}}\right]^{(k,t)} \simeq \frac{p_{\mathrm{n}}^{(k,t)} - p_{\mathrm{n}}^{(t-1)}}{g_{\mathrm{n}}^{(k,t)} - g_{\mathrm{n}}^{(t-1)}}, \tag{4.11}$$

where t and $t-1$ denote, respectively, the current and the previous time steps. This procedure requires storing the values of g_{n}^{t-1} and p_{n}^{t-1} in another appropriate history variable.

4.5.3 FBEM-SAN

In the last approach, which is referred to as *FEM-BEM semi-analytical* (FBEM-SAN), the normal contact problem at the micro-scale is solved offline with BEM, based on the generated height field given in input, for a sequence of far-field displacements. The solution of the problem in terms of predicted average contact pressure vs the imposed far-field displacement is finally fitted with a power-law continuous function of the type:

$$p_{\mathrm{n}}(g_{\mathrm{n}}) = c_1 g_{\mathrm{n}}^{c_2}, \tag{4.12}$$

which provides a closed-form expression for the normal tractions. Its derivative $\partial p_{\mathrm{n}}/\partial g_{\mathrm{n}}$ entering the linearized interface stiffness matrix $\mathbb{C}$ is also available in analytic form.

The choice of a power-law type fitting function is justified by the argument exposed in Paggi and Barber [89]. Let us assume to have two rough surfaces in contact, with specific dimensionless contact conductance $\tilde{C}$, dimensionless mean plane separation $\tilde{d}$ and dimensionless nominal contact pressure $\tilde{p}$. Making the hypothesis of incomplete similarity on $\tilde{p}$, a power-law dependence can be postulated between $\tilde{C}$ and $\tilde{p}$, in the form:

$$\tilde{C} = \Phi \tilde{p}^{\beta}, \tag{4.13}$$

where Φ is a coefficient depending on the fractal geometry of the surface and β is an exponent that real or numerical experiments can obtain. This hypothesis holds for physical systems which are in an intermediate situation between two limit conditions, which in the present set are the high and low separations regime, respectively. Together with the previous hypothesis, the electrical-mechanical analogy (Barber [88, Ch. 4, pp. 44-47]) states that:

$$\tilde{C} = -2\frac{\mathrm{d}\tilde{p}}{\mathrm{d}\tilde{d}}. \tag{4.14}$$

By combining Eq.s (4.13) and (4.14), the result is an ordinary differential equation with separable variables, with solution, for $\beta \neq 1$:

$$\frac{\tilde{p}^{1-\beta}}{1-\beta} = -\frac{\Phi}{2}(\tilde{d}_0 - \tilde{d}), \tag{4.15}$$

which is a power-law relation between the nominal pressure and the plane separation. Following this formulation, the function (4.12) has been chosen as fitting function.

A major drawback of this approach arises when the system's state is far from intermediate, i.e. for very high or very low separations. Scatter in the contact pressures is usually observed in the first case. The contact response is ruled by the statistics of extremes of the lower tail of the asperity elevations distribution. An artificial smoothing is inevitably introduced by fitting the data with a regular curve. The opposite condition corresponds to very high pressures, where distinct asperities start merging and form large contact islands. This condition is not reached in the present case, where the maximum displacement imposed for acquiring the curve employed in the SAN approach is 3σ, being σ the root mean square value of the surface elevations field measured from its lowest point and corresponds to a mean planes separation still far from the region of very high pressures.

On the other hand, a great advantage of the FBEM-SAN is its speed. It is expected to be the fastest of the three procedures if the representative rough surface is the same for all the integration points of the macroscale model (uniform spatial roughness) or when the same surface topography is used in several load cases. In these conditions, the time required by the BEM to solve the normal contact problem is spent only once, during the off-line stage. However, it is not difficult to imagine different scenarios where one method's convenience concerning another is not given for granted. For example, in the case of a realistic macroscale model where roughness is not homogeneous but depends on the point, the semi-analytic method is still applicable, but fitting a different curve for every required Gauß point is necessary. Furthermore, when a different kind of topology is present, e.g. a complex or textured rough surface, the power-law expression of the pressure-displacement relation could reasonably fail in predicting the trend of the curve under examination. Therefore this kind of interpolation could introduce an undesirable approximation to the problem. In such a different scenario, the Semi-Analytic implementation can still be applied, provided that a more

suitable and perhaps more complex interpolating function is determined. The other two approaches are expected to be more competitive when the gap-pressure range involved in the problem is unknown from the beginning, and in general, when the off-line stage becomes expensive. Testing the efficiency of the FBEM-SAN concerning the integrated FBEM-QN and CQN in these and other different scenarios would be worthy of interest and is left for further investigations.

4.6 Numerical examples

This section proposes a benchmark test to illustrate the proposed FEM-BEM multi-scale approach's capabilities and compare the different solution strategies' performances. Two square blocks of lateral size $L = 10^{-2}\mathrm{m}$[‡] are discretised by a single finite element, see Fig. 31. An interface finite element connects the common face of the two bodies.

The two materials have Young's moduli $E_1 = E_2 = 10^{12}\mathrm{Pa}$ and Poisson's ratios $\nu_1 = \nu_2 = 0.0$, where the subscripts 1 and 2 identify the lower and upper bodies, respectively. Choosing the same elastic properties for the two blocks avoids the coupling between the normal and the tangential contact problems. A frictional constitutive response for the interface is not specified in this chapter. Using Eqs. (3.4a) and (3.4b), we end up with a composite Young's modulus $E = 0.5 \times 10^{12}\mathrm{Pa}$ and a composite Poisson's ratio $\nu = 0.0$ to be used as input parameters for BEM.

Horizontal and vertical restraints are applied at the top-left nodes of both bodies and to the lower nodes of the lower blocks to avoid rigid body motion. An imposed downward vertical displacement Δ acts on the upper side of body 1, monotonically increasing with a pseudo-time variable to simulate the quasi-static normal contact problem, starting from 0 up to a maximum value of 3σ, denoting σ the root mean square of the surface roughness used to represent the rough surface.

The simulations have incorporated three different rough fractal surfaces generated using the RMD algorithm, see Paggi and Barber [89] and

[‡]Hereinafter, every length is expressed in metres, times in seconds and forces in Newton, unless differently specified.

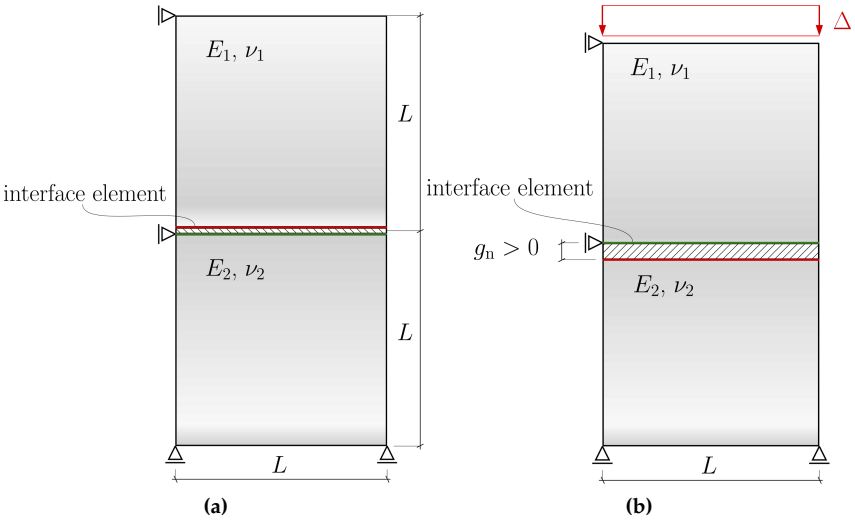

Figure 31: Geometry and boundary conditions of the benchmark test in uniaxial compression.

Peitgen, Saupe, and Barnsley [106]. The Hurst exponent has been set equal to $H = 0.7$, while three resolutions corresponding to $n = 6$, 7 and 8 have been considered, which implies having 65, 129, and 257 heights per side, respectively. The aim is to compare the computational complexity by increasing the dimension of the contact problem solved by BEM at each Gauß point and assessing how different coupling strategies affect the accuracy of the contact predictions.

For applying the present method, which hinges on the assumption of scale-separation between the micro and the macro scales, all the rough surfaces input for BEM should be statistically representative of roughness. Their lateral size l should be much smaller than the macroscopic lateral size L. In the present case, the ratio $l/L = 0.1$ has been chosen. The maximum height of the rough surface is $z_{\mu,\max} = 5 \times 10^{-5}\,\mathrm{m}$. An example of the generated surface is shown in Fig. 32.

The proposed tolerance value used to control the error in Eq. (4.9) is equal to 10^{-2}, which gives good accordance between the gap-pressure

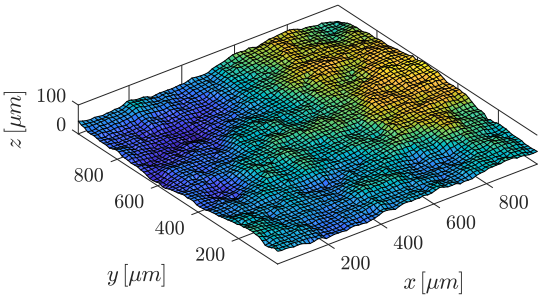

Figure 32: Example of a RMD rough surface ($n = 6$).

curves evaluated in the convergence study as shown in Fig. 33 for the given dimensionless displacements Δ/σ and the example surface with $n = 6$.

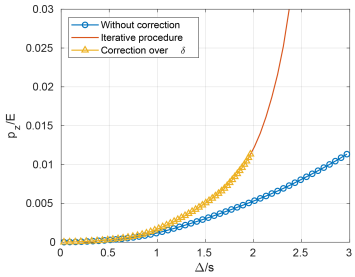

Figure 33: Comparison of the gap-pressure curves evaluated using two different procedures with tolerance set as 10^{-2}.

The FBEM-QN, FBEM-CQN and FBEM-SAN solution strategies are herein compared in terms of dimensionless force $P/(EA)$ vs h/σ, where P is the total normal load computed from the sum of the vertical reactions forces at the constrained nodes of the macro-scale finite element model, E is the composite Young modulus, A is the macro-scale nominal contact area, and $h = z_{\mu,\max} - \sigma + g_{\mathrm{n}}$ is the actual distance between the flat plane and mean plane of the rough surface, i.e. the mean planes separation. For the FBEM-QN approach, for each iteration, a value of the

Table 2: Coefficients of the power-law function $p(g_n) = c_1 g_n^{c_2}$, together with goodness of fit parameters.

n	c_1 [N/μm^2]	c_2	SSE	SSR	SST	R^2
6	1.416×10^{-06}	2.831	5.677×10^{-07}	3.773×10^{-04}	3.722×10^{-04}	0.9985
7	1.240×10^{-06}	2.862	4.073×10^{-07}	3.576×10^{-04}	3.537×10^{-04}	0.9988
8	1.064×10^{-06}	2.905	3.407×10^{-07}	3.461×10^{-04}	3.437×10^{-04}	0.9990

perturbation $\Delta g_n = 0.01 g_n$ has been chosen.

For the FBEM-SAN scheme, the curve used to fit the off-line BEM contact predictions is chosen as a power-law function given by Eq. (4.12) and the fitting has been performed employing MATLAB's built-in `fitnlm` function[§] for performing non-linear regressions. The resulting curve coefficients are collected in Tab. 2 for the three different surface resolutions distinguished by the value of n, together with the sum of squares due to error (SSE), the sum of squares of the regression (SSR), the total sum of squares (SST) and finally the R-square (R^2) coefficients. Improvements in all the estimators can be observed as the resolution gets higher. Another critical point regards the number of time steps n_Δ to be employed during the off-line computation of the fitting coefficient. Fig. 34a and Fig. 34b show, respectively, the variation of R^2 and the CPU time required by the off-line stage concerning the number of discretization steps. The value of 10^2 steps, used in the present benchmark example, represents a good trade-off between fitting accuracy and computational time spent during the operation.

The $P/(EA)$ vs. h/σ contact predictions are shown for rough surfaces with resolution parameter $n = 6, 7$ and 8 in Figs. 35a, 35c and 35e, respectively. The same results are collected for each value of n in Figs. 35b, 35d and 35f to compare FBEM-QN, FBEM-CQN and FBEM-SAN schemes. Overall, we notice that the three approaches provide almost coincident results for the highest surface resolution (surface with $n = 8$). Simultaneously, the semi-analytical scheme leads to slightly different predictions for lower resolutions (surfaces with $n = 6$ and $n = 7$). As anticipated

[§]See `https://uk.mathworks.com/help/stats/fitnlm.html` for documentation.

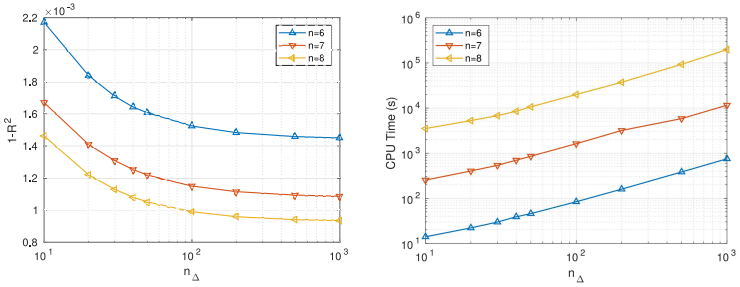

(a) R-square coefficient. **(b)** Computational time.

Figure 34: Parametric study over the number of time steps used in the fitting, for the same imposed far field displacement Δ.

before, the reason for that is related to the power-law function used to approximate the contact response in the FBEM-SAN scheme, which does not exactly reproduce the actual BEM contact response for coarse meshes or large separations, being affected by a scatter induced by statistics of extremes of the asperity height distribution.

This trend is even more evident by examining the dimensionless normal contact stiffness $C_{\mathrm{mat}}\sigma/E$ vs. the dimensionless normal tractions p_{n}/E depending on the resolution parameter $n = 6$, 7 and 8 shown in Figs 36a, 36c and 36e, respectively. The same results are again collected for each n in Figs 36b, 36d and 36f to compare FBEM-QN, FBEM-CQN and FBEM-SAN schemes. Overall, we notice that the three approaches provide almost coincident results for the highest surface resolution (surface with $n = 8$) and the low-separations regime. The smoother response predicted by the FBEM-SAN scheme for coarse surfaces and high separations is primarily due to the artificial smoothing of the actual contact response introduced by the power-law best-fitting equation. For large separations, the actual contact behaviour is governed by few asperities in contact. Therefore the contact response should present oscillations and a non-smooth behaviour by increasing the number of contact spots (increasing the pressure or the surface resolution). The power-law best-fit approximation becomes much more reliable.

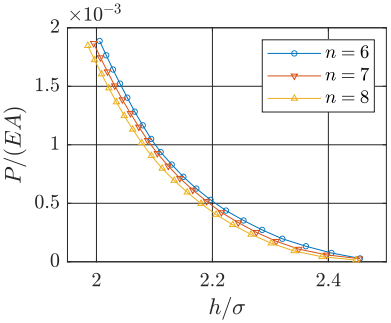

(a) FBEM-QN

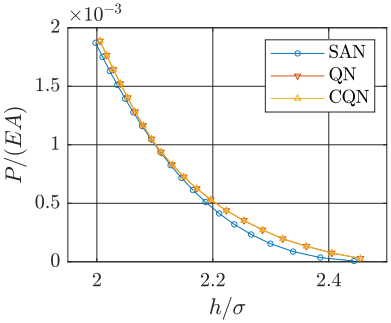

(b) $n = 6$

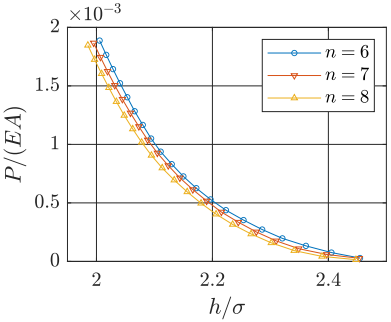

(c) FBEM-CQN

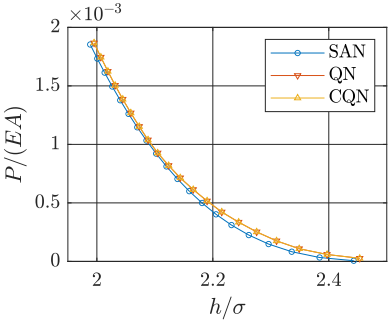

(d) $n = 7$

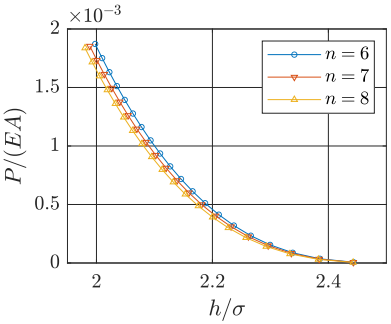

(e) FBEM-SAN

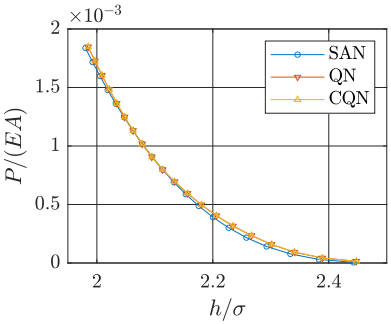

(f) $n = 8$

Figure 35: Dimensionless contact pressure vs. dimensionless normal gap predictions depending on the solution scheme and the surface resolution.

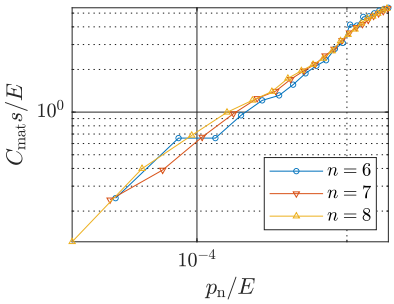

(a) FBEM-QN

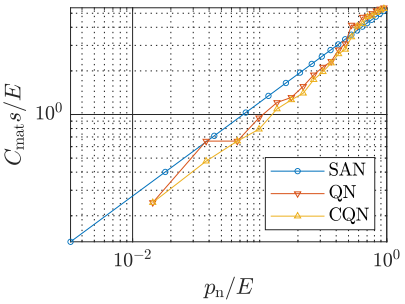

(b) $n = 6$

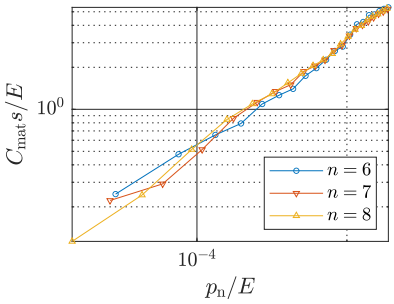

(c) FBEM-CQN

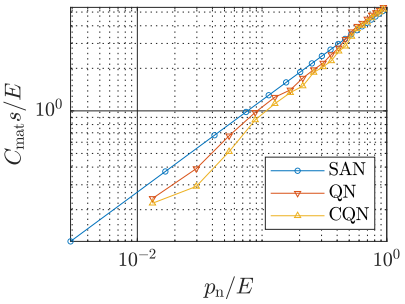

(d) $n = 7$

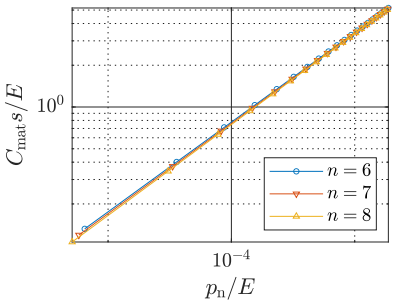

(e) FBEM-SAN

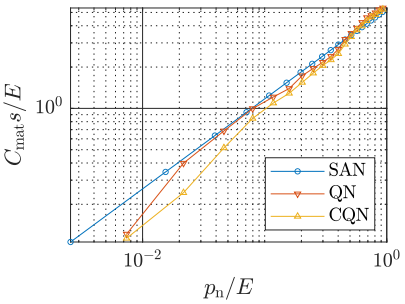

(f) $n = 8$

Figure 36: Dimensionless contact stiffness vs. dimensionless normal gap predictions depending on the solution scheme and the surface resolution.

The evolution of the residual norm vs the number of iterations of the numerical scheme used to solve the set of nonlinear algebraic equations is highlighted in Figs. 37b, 37d and 37f, for the FBEM-QN, FBEM-CQN and FBEM-SAN solution strategies applied to surfaces with different resolution parameter n. Furthermore, Figs. 37a, 37c and 37e compare the three numerical strategies' convergence rate for the same surface resolution. These results correspond to the last time-step ($\Delta = 3\sigma$), with a convergence tolerance of 10^{-9}. As expected, the FBEM-SAN displays a quadratic convergence, regardless of the resolution, since the tangent stiffness is computed exactly from the derivative of the pressure-separation relation, given in the analytic form. FBEM-QN and FBEM-CQN display a slower convergence rate than FBEM-SAN, requiring at least one iteration more than the semi-analytic approach due to the numerical approximation of the tangent stiffness matrix.

The CPU time required to solve the contact problem is shown in Figs. 38a, 38c and 38e for the FBEM-QN, FBEM-CQN and FBEM-SAN solution strategies and in Figs. 38b, 38d and 38f for the three different resolutions. The CPU time for the FBEM-SAN strategy includes only the time required for FEM to solve the macro-scale contact problem without the time for the off-line execution of BEM since this preparatory step is very case-specific and depends not only on the maximum value of pressure required but also on the accuracy requested to the fitting operation, as already shown in Fig. 34b.

The FBEM-SAN is much faster than the other two strategies, especially for intermediate and low separations when the time required for the micro-scale BEM computations spent to predict the contact pressure and the contact stiffness in the QN and the CQN schemes is significant. Both the integrated approaches become more expensive as the number of contact points increases, for the higher resolution or the decreasing separation between the surfaces. These last two strategies show almost the same CPU time, with slight differences: the QN is faster at the beginning for high separation while the CQN allows saving time in the low separation range.

Compared to the semi-analytical approach, the fully integrated FEM-

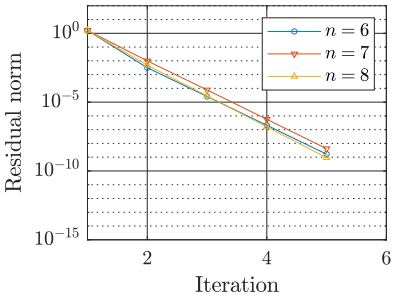

(a) FBEM-QN

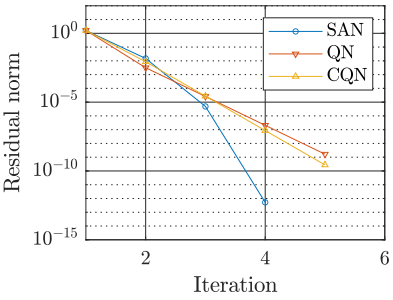

(b) $n = 6$

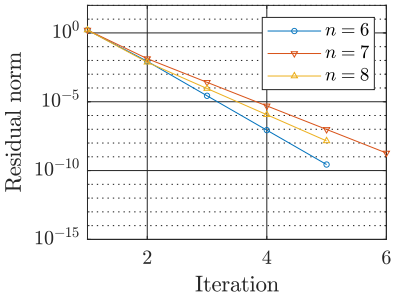

(c) FBEM-CQN

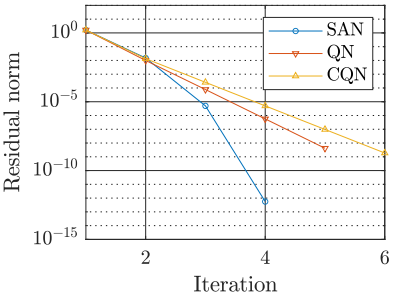

(d) $n = 7$

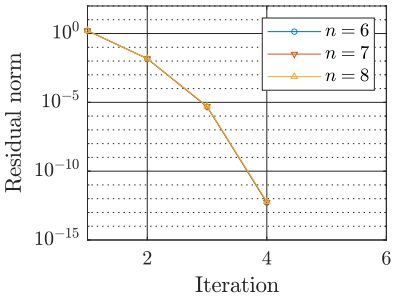

(e) FBEM-SAN

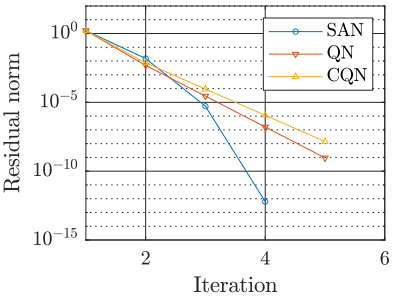

(f) $n = 8$

Figure 37: Residual norm vs. iteration step depending on the solution scheme and the surface resolution.

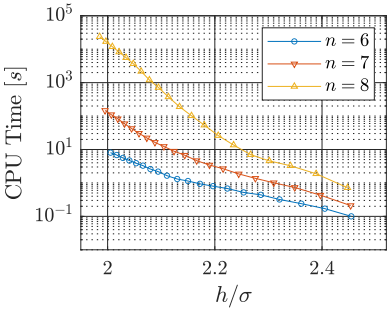

(a) FBEM-QN

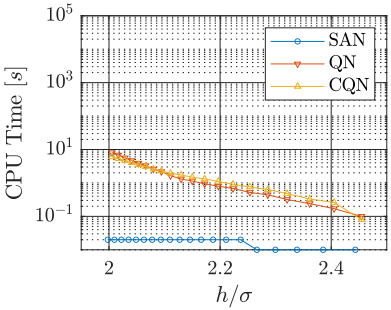

(b) $n = 6$

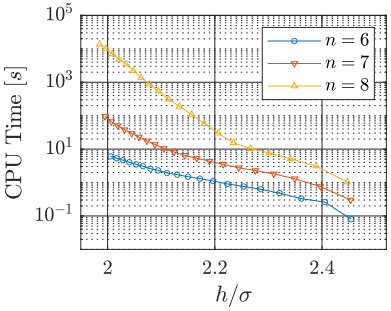

(c) FBEM-CQN

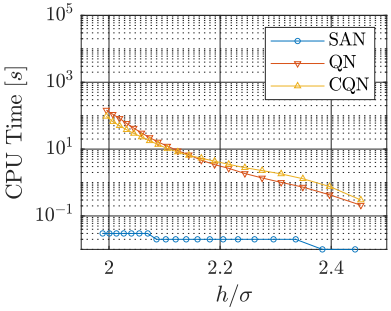

(d) $n = 7$

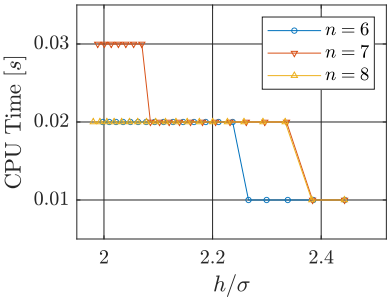

(e) FBEM-SAN

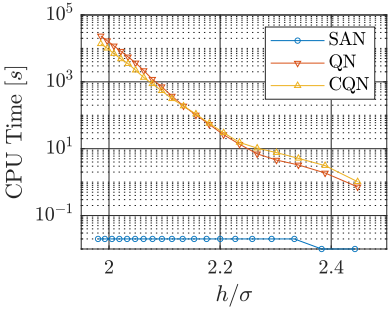

(f) $n = 8$

Figure 38: CPU time (s) vs. dimensionless normal gap predictions depending on the solution scheme and the surface resolution.

BEM strategies are more expensive. Their versatility allows them to solve a wider range of situations, e.g. more complex load cases involving concurrent normal and tangential loading. A pre-computation of the contact response would be very expensive, given the infinite number of possible case scenarios. In general, the proposed approach can be applied using the algorithm best suited for the analysed system. Possible scenarios of application of the three routines is an open issue for subsequent studies.

In addition to the three approaches' examined computational performance, it is important to notice that FBEM-QN and FBEM-CQN allow extracting local information about the micro-scale contact problem. For example, the pressure field and the free volume evolution can be easily extracted at each time step from the model without any additional effort (see Fig. 39). Their values can benefit multi-field problems involving heat transfer or reaction-diffusion phenomena and simulations, including wear and friction, where the knowledge of contact islands and actual pressure distribution plays a key role. On the other hand, in the FBEM-SAN approach, the information about the percentage of contact area can be easily recovered using an additional interpolating function during the off-line stage to obtain the relation between the total contact area and the average contact pressure.

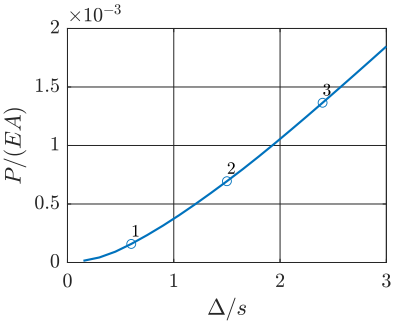

(a) Dimensionless overall reaction force against the imposed displacement.

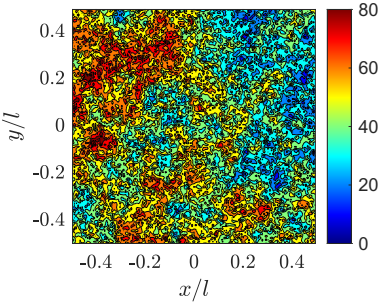

(b) Point 1, $A/A_{\mathrm{n}} = 0.38\%$.

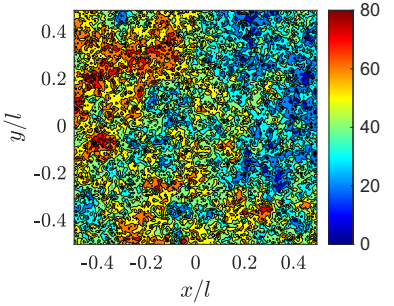

(c) Point 2, $A/A_{\mathrm{n}} = 1.66\%$.

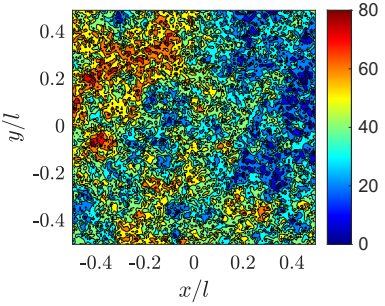

(d) Point 3, $A/A_{\mathrm{n}} = 3.12\%$.

Figure 39: Evolution of the free volume of the real geometry at the micro-scale for three different levels of imposed displacement, for the $n = 7$, FBEM-QN case. For every one of the three contour plots the ratio between the actual contact area A and the nominal one A_{n} is provided, while the dark blue islands show the contact area, the deepest valleys are marked in red.

Chapter 5

Advanced applications

In this Chapter, two possible further applications of the previous chapters' computational methods are discussed to inspire further research directions. The first is the solution of 3D contact problems using the embedded surface geometry strategy. The second tackles the problem of an inelastic bulk, more precisely the indentation of a linear viscoelastic material by a rigid body that undergoes finite sliding.

5.1 Application to 3D surfaces

The concept exposed in Ch. 3 for 2D geometries is applied here to complex contacting surfaces in 3D by considering an equivalent interface discretised by a structured mesh of 8-nodes *hex* elements in which the opposite facets belong one to the indenter and one to the deformable bulk. First of all, a patch test consisting of three elements only is performed. The lower one models the deformable bulk, the intermediate one consists of the interface element and the upper one models the rigid indenter. An ironing test is performed, first compressing the element and then applying horizontal far field displacements along with the two horizontal directions x and y. The stresses are transmitted along with the three main directions, as highlighted by comparing the nodal reactions at the restrained base nodes.

Subsequently, the model is validated against a classic Hertz problem. Some interesting considerations about the method's applicability can be drawn from this basic example for both the friction and frictionless case, which are useful for the latter practical application.

Finally, the method is tested against complex surfaces under general loading conditions. First, the frictionless normal contact considering a set of RMD rough surfaces is considered. The contact between a rigid indenter characterised by a *Weierstrass-Mandelbrot* self-affine surface is set, accounting for friction and an imposed tangential far-field displacement. In both cases, the parameters that characterise the surface are compliant with the ones that could be identified for a real surface obtained via profilometer sampling. Also, the chosen level of discretisation is suitable for a practical application. The analytical surface is discretised over different square grids, made of 32×32, 64×64 and 128×128 interface elements, a choice that keeps computational times under a reasonable threshold for the machine employed, whose characteristics are listed in Fig. 40. Of course, this is just a design choice, being the proposed approach applicable to any resolution desired. For example, this limit could be lifted, employing specific *HPC* resources comprehensive of a dedicated iterative solver instead of the direct one employed, together with code par-

```
Architecture:          x86_64
CPU op-mode(s):        32-bit, 64-bit
Byte Order:            Little Endian
CPU(s):                80
On-line CPU(s) list:   0-79
Thread(s) per core:    2
Core(s) per socket:    10
Socket(s):             4
NUMA node(s):          4
Vendor ID:             GenuineIntel
CPU family:            6
Model:                 79
Model name:            Intel(R) Xeon(R) CPU E5-4620 v4 @ 2.10GHz
Stepping:              1
CPU MHz:               1200.000
CPU max MHz:           2100.0000
CPU min MHz:           1200.0000
BogoMIPS:              4197.54
Virtualization:        VT-x
L1d cache:             32K
L1i cache:             32K
L2 cache:              256K
L3 cache:              25600K
NUMA node0 CPU(s):     0-9,40-49
NUMA node1 CPU(s):     10-19,50-59
NUMA node2 CPU(s):     20-29,60-69
NUMA node3 CPU(s):     30-39,70-79
```

Figure 40: Server properties.

allelization rather than the sequential approach applied throughout the dissertation. The results for both the RMD and the WM surfaces are compared in terms of computational time required and convergence properties.

5.1.1 Patch test

A patch test is performed to assess the element's capability to transfer normal and tangential stresses across the interface under uniform loading. To do so, a basic geometry is modelled, made of three staggered $8-$nodes *hex* elements. The lower one is linear elastic, the upper one mimics a rigid block, and finally, the central one coincides with a single interface element. In this example, no correction is made on the normal gap in such a way to simulate a flat interface. Friction is still accounted for, with a friction coefficient $\mu = 0.2$. The elastic and rigid blocks share the same geometry. The height h is unitary, the horizontal cross-section is square, and width-to-height ratio is 2. The thickness (height) of the interface, nevertheless a dummy dimension according to the element formulation, has been set equal to $0.1h$. The base nodes have been restrained by a proper set of Dirichlet boundary conditions. A uniform imposed displacement is applied to the top facet, following a loading path sketched in Fig. 41 in the displacement space $\mathbf{\Delta}$, parametrised in time and normalised concerning the height of blocks and the friction coefficient. First,

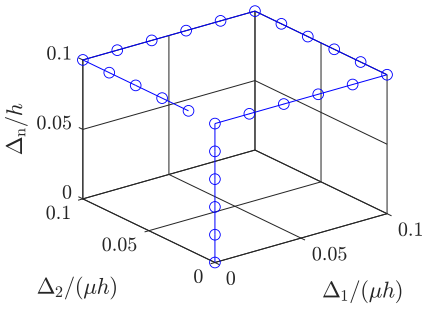

Figure 41: Load path in $\mathbf{\Delta}$ space.

a vertical displacement is applied, which is then held constant while two non-concurrent horizontal displacements acting along x and y directions complete a square loop.

The simulation results in terms of vertical displacements and normal stress σ_z are qualitatively shown in Fig. 42. The results are relative to the last time step of the simulation when only the vertical load acts. The rigid body motion of the upper rigid block can be appreciated in Fig. 42a, together with the displacements transfer across the interface and the lower block's linear deformation, characterised by a null Poisson's ratio $\nu = 0$ and Young's modulus $E = 100\,\mathrm{Pa}$. Fig. 42b shows the stress transfer across the interface, still concerning the simulation's last time step. The result is a uniform stress field as required by equilibrium considerations. Results in term of forces transfer across the interface are shown in Fig. 43a. The normal force P and the horizontal forces Q_1 and Q_1 are represented by a solid black, red and blue line, respectively. All the quantities are scaled by EA, being A the cross-section of the blocks. The horizontal forces only are further divided by μ to easily spot a gross slip condition, which under the current imposed load does not occur. For every time step, the forces are also evaluated as the sum of the base nodal reaction forces, upward-pointing triangle marker, and directly from the displacement field, applying the interface constitutive

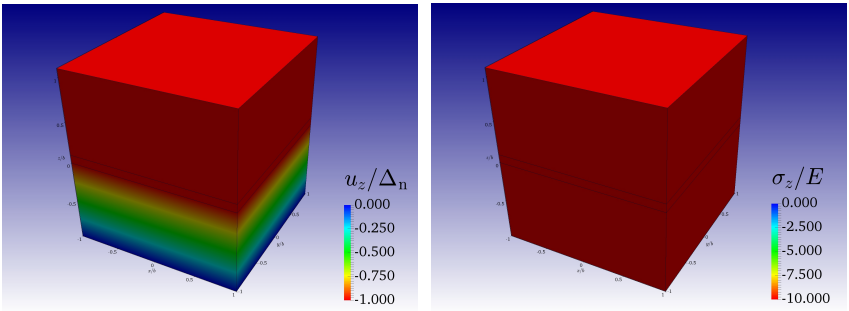

(a) Displacements contour plot. **(b)** Stresses contour plot.

Figure 42: Patch test results (qualitative).

equations, downward-pointing triangle marker, showing perfect accordance between the three quantities of interest. Finally, Fig. 43b shows the convergence rate of the Newton-Raphson iterative scheme for a selected time step of integration, coincident with a point of concurrent application of both horizontal displacements and considered more challenging for the solver. The error related to the residual norm and the energy norm are both depicted, solid blue and red line respectively, together with their respective tolerance threshold above which convergence is assumed. In all the two cases considered, convergence is achieved in six iterations. The order of convergence q is shown related to the fifth iteration of the Newton-Raphson scheme. In both cases, it is superlinear,

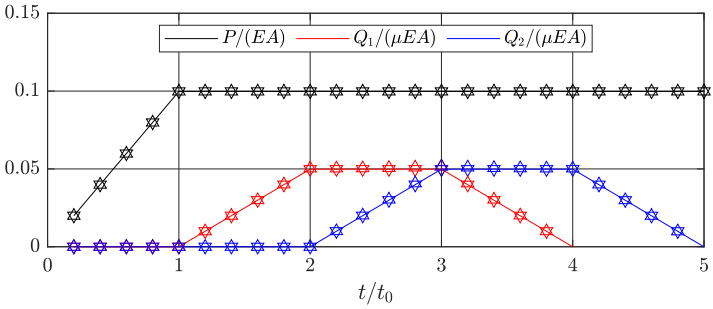

(a) Applied load and reaction forces.

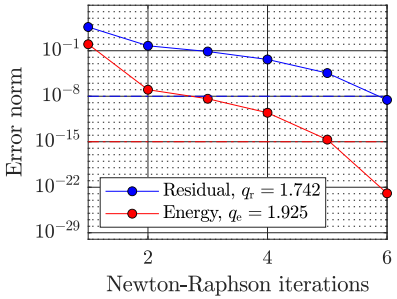

(b) Convergence analysis.

Figure 43: Patch test results (quantitative).

almost quadratic, if the rate of convergence of the energy norm is considered.

5.1.2 Model validation

A 3D Hertzian contact is used for validating the presented implementation. In the classic formulation of the problem, a paraboloid is employed as a first-order approximation of a rigid spherical surface with radius R, which comes into contact with a deformable, linear elastic half-space, no friction is assumed at the interface. The problem is radially symmetric, and the solution is given in terms of contact radius a and ellipsoidal normal contact tractions distributions $p(\mathbf{x})$, being P their resultant. Given a vertical imposed displacement Δ_{n}, the above quantities read:

$$a = \sqrt{R\Delta_{\mathrm{n}}}, \qquad P = \frac{4}{3}\frac{E}{1-\nu^2}\sqrt{R\Delta_{\mathrm{n}}^3}, \tag{5.1}$$

being E and ν Young's elastic modulus and Poisson's ratio of the half-space. The comparison is carried on under the application of a monotonically increasing vertical displacement, starting from zero up to a value of $\Delta_0 = 5 \times 10^{-5} R$ with constant time steps. Finally, the values chosen for the bulk's characterisation are $E = 1\,\mathrm{Pa}$ and $\nu = 0.0$. Numerical simulations are performed, assuming both frictionless and frictional interfaces to highlight the differences that arise due to coupling and affect the normal response in the absence of a direct tangential load.

A close up of the FEM implementation focused on the contact zone can be seen in Fig. 44.

Since no parallelisation of the code has been performed yet, a constraint is present on both the contacting surface's active set and the bulk's mesh discretisation for attaining reasonable computational time on the machine whose specifications have been given in Fig. 40. The contact active set comprehends a square patch of interface elements, discretised using three different resolutions, with 2^3, 2^4 and 2^5 contact elements per side, respectively. Given the problem symmetry, only a quadrant of the problem has been actually modelled. The elastic bulk must reproduce the behaviour of a half-space. It has been modelled with a cylinder, with

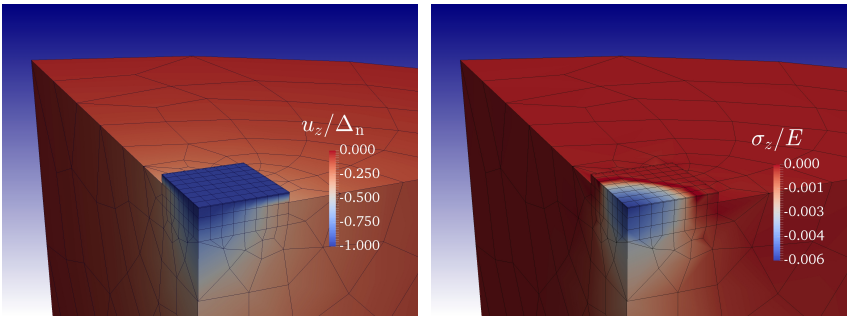

(a) Bulk and interface discretisation, to be replaced with ParaView.

(b) Contact patch magnification, to be replaced with paraview.

Figure 44: Problem set up (a) and close look on the contact quarter patch (b), with the parabolic profile embedded in the upper layer, characterised by constant displacement.

constrained nodes on the base and a contact patch located at the top surface's centre. The cylinder's radius and height have been increased until the vanishing of their influence on the simulation results, thus guaranteeing the equivalence of the FEM model of the bulk with a half-space. To reduce the problem degrees of freedom, the mesh has been graded starting from the contact patch, where a single interface element has a characteristic length $h_i = 2^{1-n_i}$, being $n = [3, 4, 5]$ the resolution coefficient. The mesh elements reach a characteristic dimension of $h = 20$ in correspondence with the bottom base and the lateral surface. The mesh dimension gradient is determined by trial and error, seeking the highest one still guaranteeing the absence of ill-shaped elements.

The solution in terms of contact reaction force, against the analytic reference solution, can be observed in Fig. 45, for the finest resolution employed. Both the frictionless ($\mu = 0.0$) and frictional ($\mu = 0.4$) numeric solutions show a stiffer behaviour compared with the exact one. As expected, the frictional case is the stiffest since the application of the vertical load cause in-plane horizontal displacements, which are counteracted by the presence of friction. The highest coupling effect can be appreciated for $\nu = 0.0$, while as Poisson's ratio tends to 0.5, uncoupling

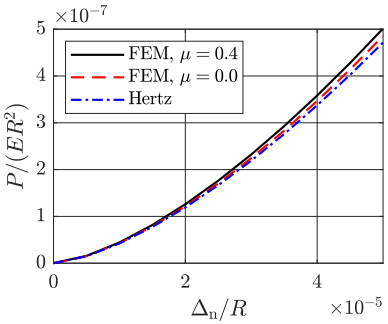

Figure 45: Model validation.

conditions are met, and the effect is supposed to vanish. The differences in percentage between the case for $\mu = 0.4$ and $\mu = 0.0$ are in line with the theory. The interested reader is addressed to Barber [88, Ch. 7, pp. 129–130] for a comparison between the presented application and the corresponding coupled axisymmetric problem without slip, which represents the opposite scenario concerning the absence of friction. An appreciable difference still holds between the frictionless case and the reference solution. The relative error is plotted in Fig. 46 for every simulation performed. A marker defines the resolution, while black solid lines depict

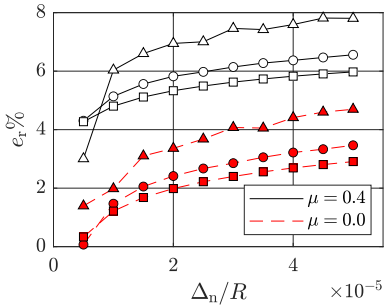

Figure 46: Variation of the relative error with the applied normal displacement and the resolution. Triangle markers depicts a coarser mesh, star markers a finer one.

the frictional case and dashed red lines the frictionless case. As already said, the shift between red lines and black lines can be ascribed to the effect of coupling. Even if the error gets lower as the resolution increase, non-negligible differences still hold, growing with the load. A possible explanation for this could be found in the combination of the penalty approach and a condition of imposed displacements. If the system is loaded only by surface tractions, correct transmission of forces at the interface is guaranteed by equilibrium, and the effect of displacements is limited. If the surface, such in the present case, is loaded by a far-field displacement, the stress transfer will be influenced by the displacements, as can be evinced by Fig. 46.

As stated in Wriggers [42, Ch. 6, p. 119], the influence of the penalty parameter is also affected by the mesh resolution. In the current simulations, for the finest mesh employed, the penalty has been chosen to obtain $\varepsilon_{\mathrm{n}} h/E = 3.125$, being $h = 3.125 \times 10^{-2}$ units the characteristic mesh size, leading to an average relative error in terms of reaction forces of about 3%. Unlike the $2D$ case presented in Ch. 3, numerical issues are now found for sensibly lower values of ε_{n}, and the one chosen represents an upper threshold above which ill-conditioning is met*. Even if the results of the validation test can be considered fully satisfactory since they have been obtained with a rather coarse mesh, the use of a different and more accurate contact strategy appears more appealing for future systemic use of the method, for which the exploitation of the penalty approach is not a strict prerequisite.

The solution in terms of contact radius is also checked. For the finest mesh, a relative error of 1.612% concerning the last loading step is found. This result is shown in Fig. 47, where the exact value of the contact radius, thick solid red line, is superposed to the normal contact tractions' contour plot.

*Actually, the system doesn't seem to be ill-conditioned, and the Newton-Raphson algorithm properly converges. However, the solution obtained is manifestly wrong, with sharp spikes in the contact tractions distribution in the proximity of the frontier between contact and non-contact region. An explanation of this is necessary to be investigated but has not been found despite an intense effort. A solution to this problem would permit increasing ε_{n} up to values leading to negligible errors and approaching the usual ill-conditioning threshold.

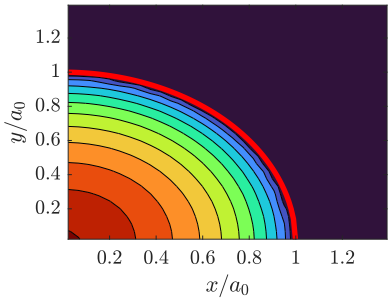

Figure 47: Contact radius.

In conclusion, the surface plot of the surface tractions is shown in Fig. 48. The numerical simulation accurately reproduces the characteristic ellipsoidal shaped distribution. The test is run considering a value of the friction coefficient $\mu = 0.4$, with a consequent stiffening effect due to geometrical coupling that can be appreciated by comparing the ratio between the maximum value predicted by the analytical model and the one obtained by the simulation, $p_0/p_{\max} = 0.8105$.

In Fig. 49, the tangential contact tractions are shown. Fig. 49a and Fig. 49b show the tangent vector's projection over the coordinate directions x and y, respectively. Since only normal loading is involved, and the profile is symmetric, they represent self equilibrated distributions,

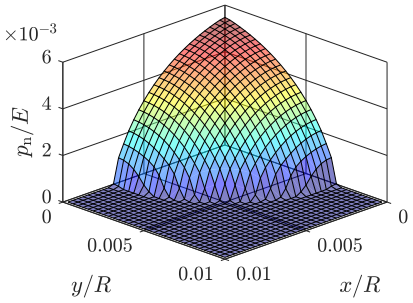

Figure 48: Normal contact tractions.

symmetrical to $y = 0$ and $x = 0$. Their magnitude $\|\mathbf{q}\| = \sqrt{q_1^2 + q_2^2}$ is represented in Fig. 49c. Again, because of the loading conditions, the distribution is characterised by polar symmetry, with a null value only in correspondence with the origin. This point is the only one that does not experience in-plane tractions. The remaining domain is split in the circumferential direction into two annular regions, an inner one for which $\|\mathbf{q}\| < \mu p$ which is therefore in a state of stick, and an outer one which radially slips under the action of the load. The stick/slip region can be determined by evaluating the ratio between the stick radius and the contact radius, with result $r_a/r_b = 0.9130$. This implies that roughly 15% of the contact area is in a partial slip state, even for this rather high coefficient of friction and no application of tangential load. This fact might be of relevance in cases where micro-slip related phenomena are considered, for example, in the study of fretting wear and fretting fatigue.

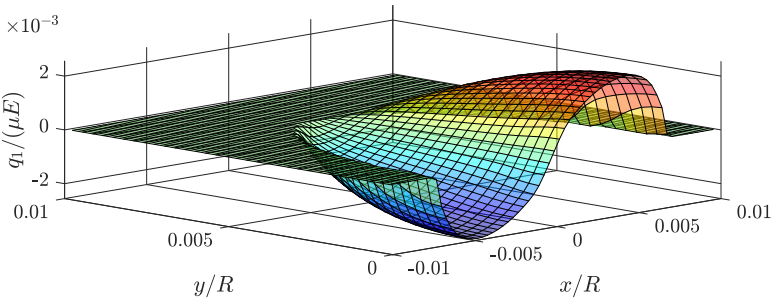

(a) q_1 contact tractions distribution.

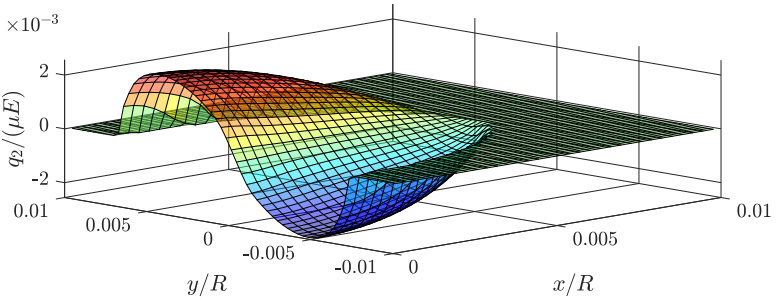

(b) q_2 contact tractions distribution.

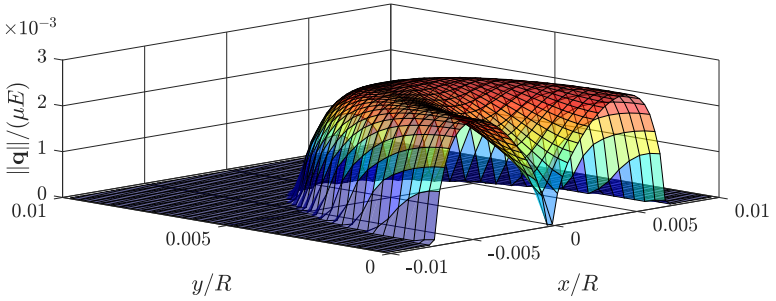

(c) Resulting $\|\mathbf{q}\|$ distribution.

Figure 49: Surface plot of tangential tractions for the Hertz problem with friction.

5.1.3 Full-scale application

In this section, the contact of a rough surface over a thin elastic layer bonded to a rigid substrate is performed. The indenter is discretised with a mesh composed of 32×32, 64×64 and 128×128 square elements. The bulk is composed of a structured grid of standard tri-linear *hex* elements, disposed over two layers of equivalent depth. The bulk elements have a height-to-width ratio of 5, which, given the square nominal contact area of unitary side L and the number of elements employed, gives an overall depth of $h_\mathrm{b} = 0.1563L$. A single layer of interface elements is disposed over the bulk elements, and, finally, a single layer of rigid elements on the top of it complete the mesh. The rigid indenter has been modelled as a linear elastic material with Young's modulus E_2, 3 orders of magnitude higher concerning the bottom layer modulus, together with a penalty parameter $\varepsilon_\mathrm{n} = E_2/L$. Fig. 50 shows the resulting mesh for the finest case.

Surface heights field reading

The rough surface employed in the contact simulation is stored in an external file. An extract of the routine employed for the height field reading

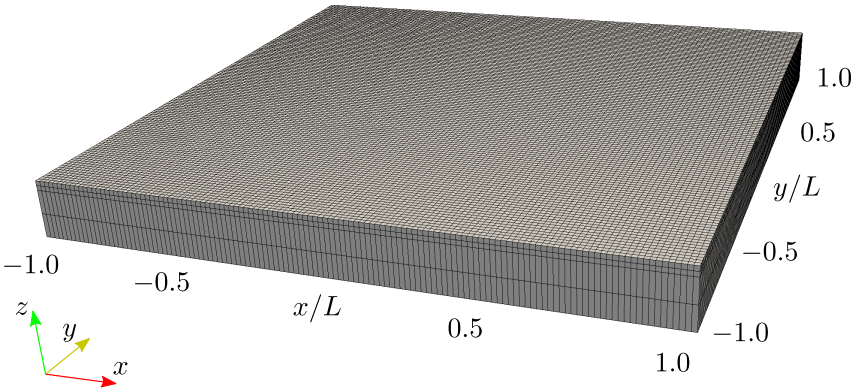

Figure 50: FEM mesh, interface discretised with 128×128 interface finite elements.

is shown in Fig. 51. The routine inputs are the surface dimension in terms of the number of subdivisions per side, and a tolerance value, stored in the array `d`. The surface height field is provided in a *.dat* file where the sampled points are stored column-wise accordingly to their x, y and z coordinates. This format coincides with the output of surface property acquirement instrumentation, as the Leica DCM confocal profilometer is present in the laboratory research group.

When an interface element composing the active set is called *for the first time*, the external surface file is read, and the points' locations are stored in a proper array, lines 352 to 356. Then, given the nodal coordinates `xm`, *cfr.* Eq. (2.32) from Ch. 2, the matching points for each node are identified and assigned to the *history variable* array `hr`, lines 358 to 372. The nodes are supposed to match the surface points if a deviation less than the imposed tolerance holds for the respective coordinate for each

```
347         if(hr(nh3-1+5).eq.0.0d0) then
348
349           mx = int(d(4) + 1)
350           my = int(d(5) + 1)
351
352           open(250,file='surf.dat',status='old')
353           do i=1,int(my*mx)
354             read(250,*) (surf_data(i,j), j=1,3)
355           end do
356           close(250)
357
358           do i=1,int(my*mx)
359             if (abs(xl(1,1)-surf_data(i,1)).lt.d(6) .and.
360      &          abs(xl(2,1)-surf_data(i,2)).lt.d(6)) then
361               hr(nh3-1+1) = surf_data(i,3)
362             else if (abs(xl(1,2)-surf_data(i,1)).lt.d(6) .and.
363      &               abs(xl(2,2)-surf_data(i,2)).lt.d(6)) then
364               hr(nh3-1+2) = surf_data(i,3)
365             else if (abs(xl(1,3)-surf_data(i,1)).lt.d(6) .and.
366      &               abs(xl(2,3)-surf_data(i,2)).lt.d(6)) then
367               hr(nh3-1+3) = surf_data(i,3)
368             else if (abs(xl(1,4)-surf_data(i,1)).lt.d(6) .and.
369      &               abs(xl(2,4)-surf_data(i,2)).lt.d(6)) then
370               hr(nh3-1+4) = surf_data(i,3)
371             end if
372           end do
373
374           hr(nh3-1+5) = 1.0d0
375
376         end if
```

Figure 51: Code snippet for external surface reading.

of them. After the proper value of elevation has been assigned to each of the four nodes, a flag is activated, line 374, which prevents the process from being repeated in subsequent calculations, such that the external surface is red only once for each element, and each element stores only the four elevation values directly affecting it.[†] A surface plot showing the heights distribution for the two cases is shown in Fig. 52, both plots are related to the finest resolution employed. The latter case, Fig. 52b is considered particularly interesting, since a contact problem involving such surface, solved with standard computational contact mechanics arguments appears very difficult, given the scatter in the heights distribution and the total lack of smoothness. The next two paragraphs present all the details related to the geometrical features of the problem, for repeatability purposes.

Problem set up for the WM surface

The Weierstrass-Mandelbrot quasi-fractal surface is evaluated as:

$$z(x,y) = A \sum_{n=1}^{N} \sum_{m=1}^{M} \gamma^{(D-3)(n-1)} \Big[\cos \phi_{m,n} - \cos \frac{2\pi\gamma^{n-1}}{\lambda_0} \Big(x \cos \frac{\pi m}{M} + y \sin \frac{\pi m}{M} + \phi_{m,n} \Big) \Big], \quad (5.2)$$

is characterised by the parameters in Tab. 3 and shown in Fig. 52a. The matrix in Eq. (5.3) collects the random phase angles employed during the surface generation process.

[†]A different approach, perhaps more efficient, could be tempted by assigning the elevation to each node index-wise, but this would affect the robustness of the implementation since care should be taken in the ordering of the entries of the external file, which would be cumbersome in the current case of a $3D$ surface, and the situation would rapidly degenerate considering interface elements where the heights are sampled in more than four nodes.

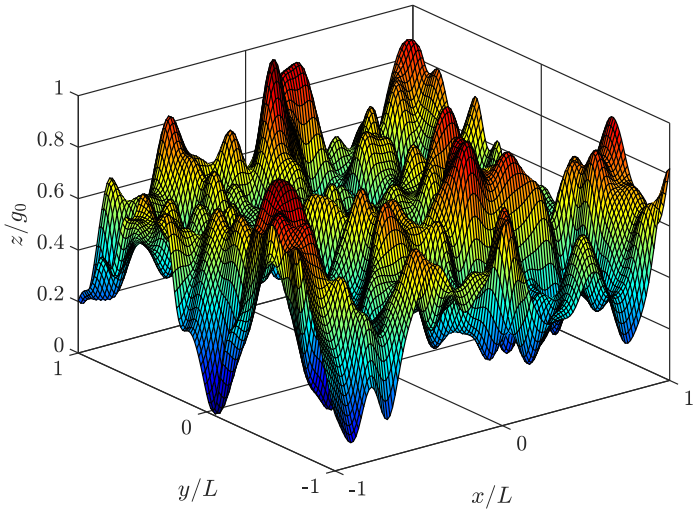

(a) Surface generated with the Weierstrass Mandelbrot function.

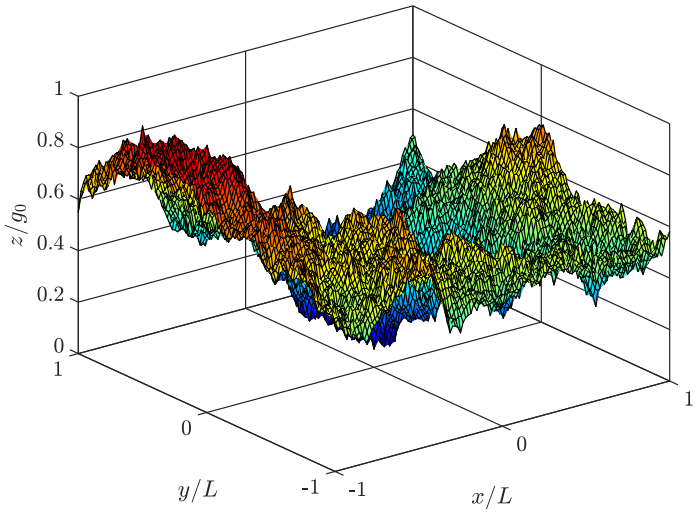

(b) Surface generated with the Random Midpoint Displacement algorithm.

Figure 52: Plots for the highest resolution surfaces tested.

$$\boldsymbol{\Phi} = \begin{bmatrix} 5.9698 & 3.8669 & 0.3637 & 0.0960 & 5.2661 & 1.2154 & 3.1199 & 4.5686 \\ 1.4523 & 4.9759 & 2.2171 & 4.6922 & 0.1234 & 4.2865 & 5.6534 & 1.9433 \\ 3.8129 & 5.7919 & 5.1093 & 2.7966 & 4.2806 & 1.9023 & 5.1624 & 5.2684 \\ 3.0535 & 4.6383 & 0.0620 & 5.8548 & 2.3843 & 3.4034 & 4.0521 & 3.5693 \\ 5.6002 & 1.1075 & 0.8727 & 2.9279 & 5.2263 & 0.9480 & 5.1395 & 2.3274 \\ 4.7884 & 2.5491 & 1.2740 & 2.6305 & 3.1593 & 4.3850 & 4.1483 & 4.4154 \\ 2.8681 & 5.8777 & 1.2486 & 5.3170 & 4.4577 & 2.3774 & 2.1487 & 3.4342 \\ 0.1163 & 5.7611 & 3.7937 & 3.2996 & 2.6948 & 5.4036 & 1.8204 & 2.7953 \\ 5.1611 & 2.5778 & 1.7102 & 1.2733 & 1.9140 & 5.3637 & 2.1438 & 4.3641 \\ 2.7942 & 5.6150 & 1.2492 & 4.2232 & 1.1916 & 3.7295 & 3.3557 & 3.9038 \end{bmatrix}$$

The load is applied as a far-field displacement subdivided into three different stages of equal duration. In the first one, a purely normal displacement Δ_{n} is imposed, starting from zero and reaching its final value $\Delta_0 = 3.00 \times 10^{-3} L$ at $t_1 = 1.00\,\mathrm{s}$. The normal load is then held constant, while the indenter is translated along x direction with constant positive velocity, reaching a maximum value $\Delta_{\tau,0} = \mu\Delta_0$ at $t_2 = 2.00\,\mathrm{s}$, being $\mu = 0.2$ the coefficient of friction. Finally, in the third phase, the indenter is linearly shifted back to its original position, reached for $t_3 = 3.00\,\mathrm{s}$. Fig. 53 shows the applied far-field displacement history, together with the resultant interface overall reactions, evaluated as the integral of the interface normal and tangential tractions. The ratio between the normal indentation and the elastic layer thickness is $\Delta_0/h_{\mathrm{b}} = 1.92\,\%$, in line with

Table 3: Weierstrass-Mandelbrot surface coefficients. The values of the random phase angle matrix $\boldsymbol{\Phi}$ can be found in Eq. (5.3).

z_0	λ_0	G	D	γ	N	M
[m]	[m]	[−]	[−]	[−]	[−]	[−]
1.00×10^{-3}	1.00×10^{0}	3.00×10^{0}	2.25×10^{0}	1.30×10^{0}	8	10

the assumption of elastic deformation of the bulk. Still, the surface characteristics have been tailored to obtain a high final actual contact area to have the possibility of investigating the contact response from high to low mean-planes separations.

Problem set up for the RMD surface

A self-affine rough surface obtained employing the same procedure exposed in Sec. 3.4 is now used for testing the $3D$ implementation. Three different magnifications are considered, defined on the same block of Fig. 50, but discretised in turn with 32, 64 and 128 elements per side, respectively. The mechanical properties of the bulk are the same employed for the former example, and so is the overall height of the surface, measured from the lowest valley to the highest peak. For repeatability, all the three surfaces tested are characterised by the same random seed $rnd = 5.4688$ and the same Hurst exponent $H = 0.75$. The resulting elevation field is shown in Fig. 52b for the highest resolution level. Since for the RMD surface, only frictionless normal contact has been considered, the load history is coincident with the first branch of Fig. 53, from $t = 0$ to $t = t_1$.

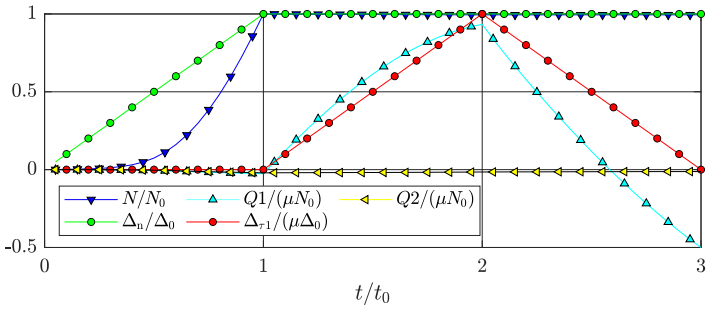

Figure 53: Far field displacement and resultant load vs. time.

Results

Considering the WM related simulations, the outcome in terms of forces response is also shown in Fig. 53. The vertical reaction force P follows the characteristic power-law behaviour as long as the load is incremented, then remains constant. During the first stage, parasitic reaction forces Q_1 and Q_2 arise due to the simulation's displacement controlled nature and the lack of symmetry of the indenting profile. During the second stage, Q_1 increases and a condition of full slip is almost reached, with the maximum value obtained ed at $t = t_2$ approximately equal to $0.85\mu P$. Over this point, the displacement is reversed, and the indenter is taken back to its original position. We observe a residual horizontal negative force, a function of the system hysteresis that can be directly linked to the frictional energy dissipation.

The contour plot of the normal tractions $p(\mathbf{x})$ at t_1 is qualitatively shown in Fig. 54. It can be seen that for the selected level of indentation, the contact area ratio $A_c/L^2 \simeq 45\%$ is reached. A clear distinction holds between the contact islands and the domain that does not experience contact, homogeneous dark blue zones.

A quantitative analysis of the displacements and contact tractions fields' evolution can be performed if a section cut is considered along a selected direction. The result of this operation at constant $\overline{y}/L = -0.65$ is shown in Fig. 55, for three different time steps covering the normal loading stage. The solid black lines represent the indenter, while the red ones the elastic bulk, for $t/t_1 = 0.50$, 0.75 and 1.00 respectively.

A quantitative evaluation of the error resulting from the relaxation of the normal contact constraints resulting from applying the penalty method can be observed in Fig. 56. The solid blue line shows the absolute level of compenetration, evaluated for a point located in correspondence of the highest pressure recorded at the end of the normal loading stage. As expected, the value of compenetration grows with the normal displacement almost linearly, but with a lower gradient concerning the normal far-field displacement, such that the relative error, in terms of the ratio between compenetration and imposed displacement, decreases

with time, solid red line of the same figure.

The evolution of the tangential reactions along x direction can be traced in Fig. 57. The green lines represent snapshots of $q_1|_{\overline{y}}$ for selected time steps. The time window chosen in Fig. 57a spans from $t = t_1$ to $t = t_2$, covering the tangential loading stage. Investigating the plot, it can be seen how the tangential tractions grow, almost reaching a condition of full slip, where they overlap with the solid black line, representing the normal tractions. The unloading phase is depicted in Fig. 57b, where

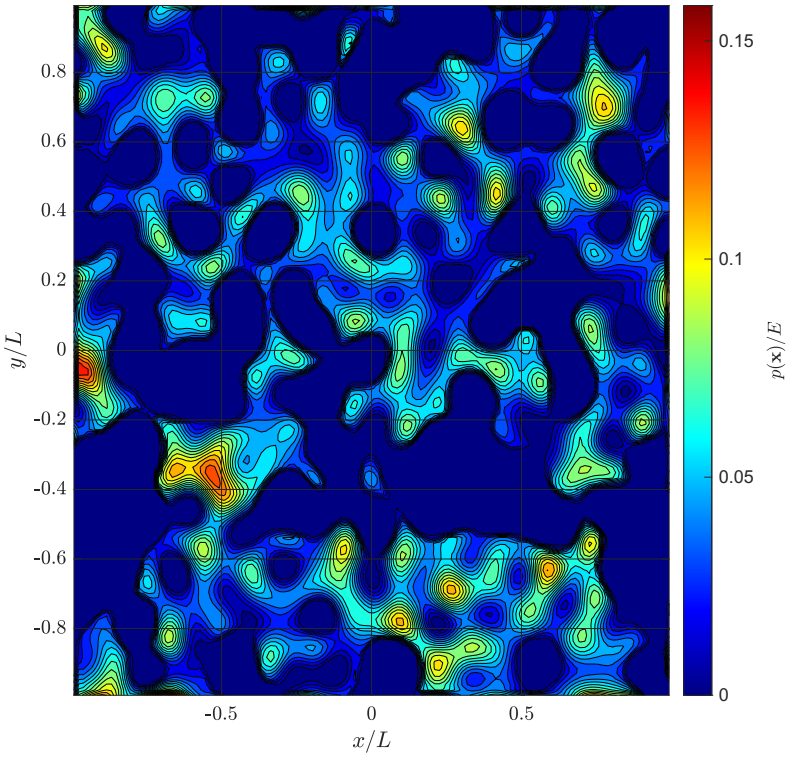

Figure 54: Contour plot of normal tractions $p(\mathbf{x})$.

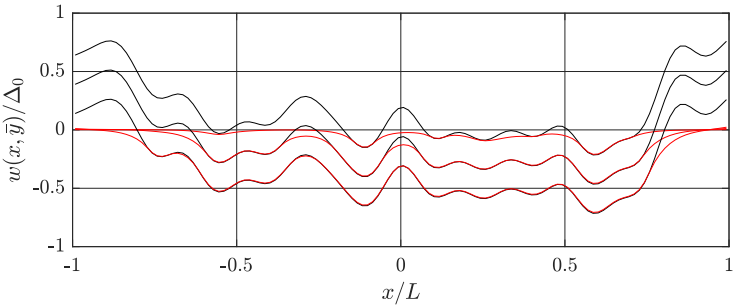

Figure 55: Vertical displacements under the action of the indenter.

the imposed horizontal far-field displacement is reversed. The system final traction distribution along $\overline{y}$ coincides with the bottom green line.

In conclusion, the performances of the framework are compared for both the RMD and the WM surfaces, along the first load branch ($fromt = 0$ to $t/t_1 = 1$). Fig. 58 shows the time employed by a complete run of all the simulations performed. As expected, the most critical factor is the number of degrees of freedom that characterises the different examples. The 32×32 elements surface is characterised by a run time of the order of seconds. For what concerns the finer scale problems, all the simulations with an equivalent number of degrees of freedom have almost identical

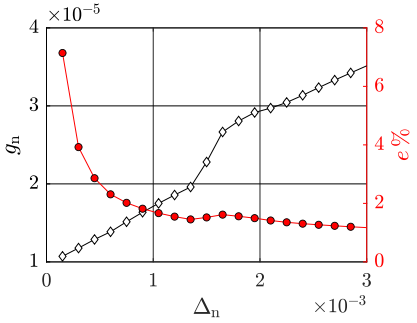

Figure 56: Quantitative assessment of the compenetration error resulting from the penalty contact enforcement.

CPU times, regardless the surfaces' smoothness. In contrast to the WM surface, the RMD surface is made of a scattered elevation field, which would result in very challenging scenarios for standard contact search algorithms. In order to investigate how the presence of friction affects the performances of the code, the same problem with the WM surface is solved also setting $\mu = 0.0$. Comparing the results, a slight difference is encountered, but the effect is remarkable for the finest resolution only, with an increase of about 12% concerning the overall computational time, and convergence properties as well are not particularly affected.

In the conclusion of this section, Fig. 59 reports, for each time step of each simulation, the total number of iterations of the Newton-Raphson

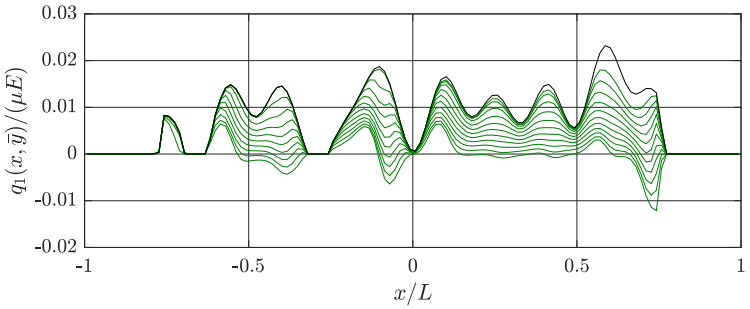

(a) Loading phase.

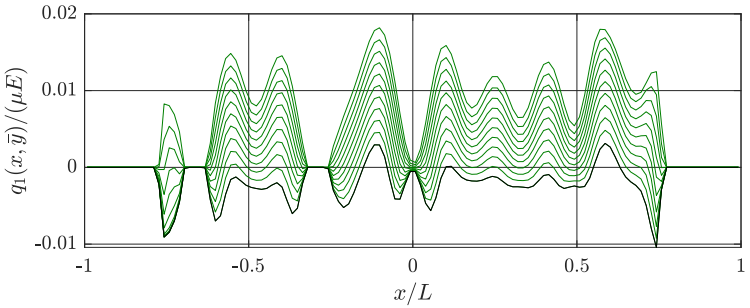

(b) Unloading phase.

Figure 57: Tangential traction distribution q_1, evaluated at $y = \overline{y}$.

algorithm employed to solve the non-linear system of equations that governs the problem. Again, no significant discrepancy is encountered despite the remarkable differences in terms of smoothness characteristics. Furthermore, in the case of the WM surface, not even friction significantly alters the convergence properties, requiring at most two additional iterations for reaching convergence.

5.2 Application to inelastic materials

The proposed formulation is herein extended and applied to the analysis of both the transient and steady-state sliding of a rigid indenter over a viscoelastic bulk. It is shown that the chosen approach is capable of dealing with arbitrarily complex profiles together with, thanks to the flexibility of the finite element method, different kinds of material constitutive

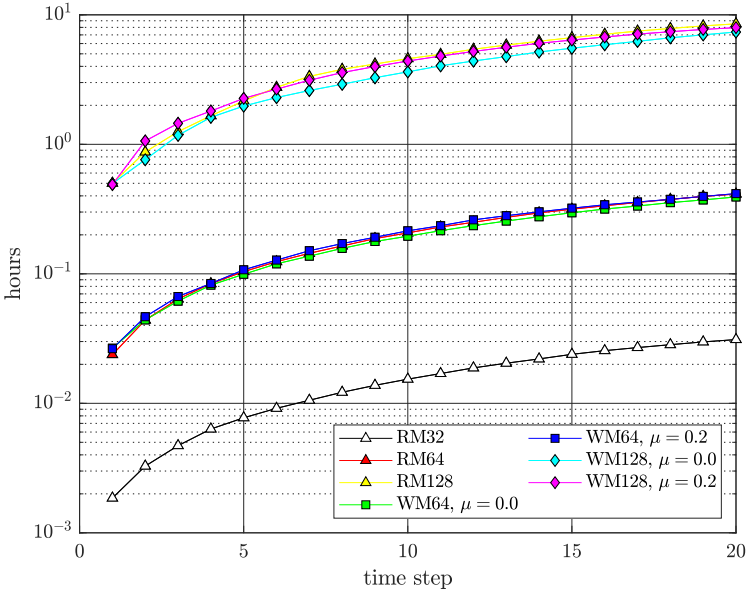

Figure 58: CPU time.

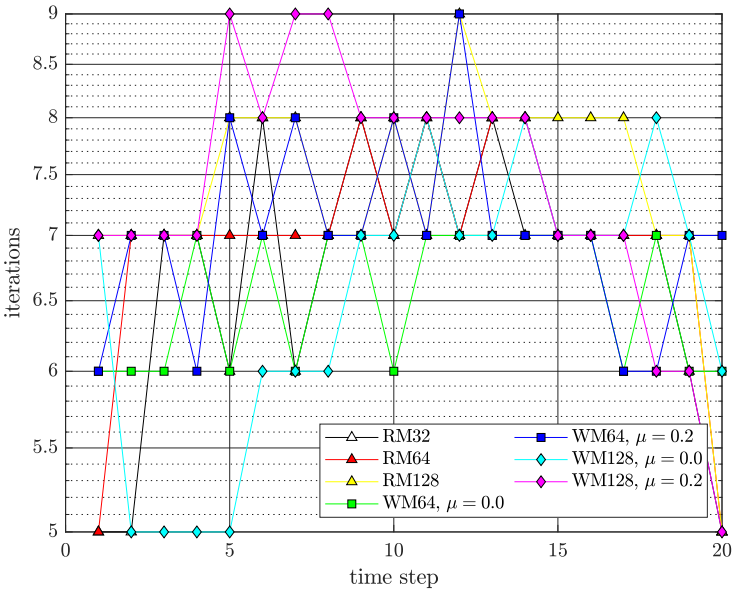

Figure 59: Newton Raphson iterations required for each time step.

behaviours. In this section, we propose a further possible exploitation of the method, which comprehends the analysis of finite interface sliding displacements.

A linear viscoelastic material has been chosen as a paradigm for more general bulk constitutive behaviours. Real viscoelastic materials present a time-dependent mechanical response that varies across several orders of magnitude of time and intensity. Therefore, a simple model with a linear Hookean spring in series with a single Newtonian dashpot is far from representative. For instance, for Ethylene Vynil Acetate (EVA) used as an encapsulating material for photovoltaics, a power-law decay of Young's modulus with time has been reported Eitner et al. [107] and Eitner [108], which can be well-modelled by a fractional viscoelastic model Paggi, Kajari-Schröder, and Eitner [109], Paggi and Sapora [110], and Gagliardi, Lenarda, and Paggi [111] as a limit of a Prony series representation with several arms. Its approximation for engineering applications usually requires at least three arms in the Prony series to provide meaningful stress analysis predictions.

A representative contact problem involving a rigid indenter with harmonic profile acting over a viscoelastic layer of finite depth, perfectly bonded to a rigid substrate, is addressed to demonstrate the proposed approach's capabilities. The loading history includes an applied displacement normal to the contacting interface during the first stage, with a progressive increase in the contact area. Afterwards, normal displacement is held constant. A horizontal far-field displacement in the sliding direction is applied to simulate the stick-slip transition and the constant sliding regime. Friction is considered along the interface, and it is mathematically treated with the same regularised friction law exploited in the former chapters. Different sliding velocities, which are relevant for the behaviour of a viscoelastic material, are examined. Numerical simulations provide useful insight into the tangential tractions' distribution in all of the phases of the sliding process. When considering different Prony series representations with several arms varying from one to three, the computational approach quantifies the effect of refining the viscoelastic constitutive model by introducing additional relaxation times. This sec-

tion is part of the work presented in Bonari and Paggi [58].

5.2.1 Rheological Model

Three different Prony series models with a number of arms increasing from one to three are examined in order to assess the effect of viscoelasticity modelling on the overall contact mechanical response. The general equation for the shear relaxation modulus reads:

$$\frac{G(t)}{G^{\infty}} = \mu_0 + \sum_{n=1}^{3} \mu_n \exp\left(-\frac{t}{\tau_n}\right), \tag{5.3}$$

where G^{∞} is the instantaneous shear modulus (evaluated at $t = 0$), μ_n are the relaxation coefficients, and τ_n are the corresponding relaxation times. Equation (5.3) has been tuned to fit the experimental values of EVA Paggi and Sapora [110]. The model parameters for 1, 2 and 3 arms are collected in Table 4. The identification of the above parameters has

Table 4: Rheological parameters for Ethylene Vynil Acetate (EVA), where n is the number of Prony series' arms.

n [–]	G^{∞} [Pa]	μ_0 [–]	μ_n [–]	τ_n [s]
1	568.498	0.421	0.579	0.817
2	674.606	0.306	0.398	0.212
			0.296	2.458
3	749.386	0.254	0.310	0.102
			0.226	0.545
			0.210	4.104

been carried out through a regression over the experimental data, acquired in the time range $t = 10^{[-1,\dots,+1]}$. The following approach has been pursued to attain a high degree of accuracy. Firstly, trial relaxation times have been set, and a preliminary linear regression has been performed involving G^{∞} and μ_i only. The objective function to be min-

imised reads:

$$\Pi(\mathbf{x}) = \sum_{k=1}^{N} \left(\mathbf{g}_k \cdot \mathbf{x} - G_k\right)^2, \tag{5.4}$$

where, for the three arms model, $\mathbf{g}_k = \left[1, e^{(-t_k/\tau_1)}, \ldots, e^{(-t_k/\tau_3)}\right]$, G_k is the value of the objective function at the sampling point and N is the number of samplings. The global minimiser $\mathbf{x}^* = \arg\min_{\mathbf{x}} \Pi(\mathbf{x})$ is evaluated and the constants μ_i and G^∞ are obtained according to:

$$G^\infty \begin{bmatrix} \mu_0 \\ \mu_1 \\ \mu_2 \\ \mu_3 \end{bmatrix} = \mathbf{x}^*, \tag{5.5}$$

together with the condition $\sum_i \mu_i = 1$, related to the shear modulus at $t = 0$. The obtained coefficients, together with their respective relaxation times, have been used to define a vector of guess values $\mathbf{x}_0$ for a second nonlinear regression, in which the relaxation times were also included in the optimisation vector $\mathbf{x}$. The problem has been solved iteratively, updating the starting vector $\mathbf{x}_0$ every cycle using the previous results. Convergence is achieved within 5 iterations at most, considering a relative error given by $(\mathbf{x}^* - \mathbf{x}_0)/\mathbf{x}_0$ and a tolerance $\varepsilon = 10^{-15}$. This procedure has been repeated in the same way for the 1 and 2 arms models.

Once the parameters are identified, the Young's relaxation modulus $E(t)$ can be obtained from $G(t)$, and the behaviour of the three models can be investigated in time and frequency domains. The analysis in the frequency domain can be performed by defining a complex modulus $\hat{E}(\omega)$, obtained via the Fourier transform of $E(t)$, which can be expressed as:

$$\frac{\hat{E}(\omega)}{E^\infty} = \mu_0 + \sum_{i=1}^{n} \mu_i \frac{\tau_i^2 \omega^2}{1 + \tau_i^2 \omega^2} + \imath \sum_{i=1}^{n} \mu_i \frac{\tau_i \omega}{1 + \tau_i^2 \omega^2}. \tag{5.6}$$

In the expression above, $\imath$ denotes the imaginary unit and the index k defines the number of arms being considered. It can be easily noticed that, for the single-arm model, the maximum viscoelastic effect manifests in correspondence to the critical excitation frequency $\omega^\star = \sqrt{\mu_0}/\tau_1$.

Fig. 60a shows a plot of $E(t)$. Figs. 60b,c show the values of the loss modulus and the storage modulus, obtained as the imaginary part

$\Im\hat{E}(\omega)$ and the real part $\Re\hat{E}(\omega)$ of the complex modulus $\hat{E}(\omega)$, respectively. Finally, Fig. 60d shows the loss tangent, given as the imaginary part over the real part ratio. As a comparison, the same quantities are also plotted for the relaxation modulus, obtained for a model that is based on fractional calculus, which reads:

$$E_{\mathrm{f}}(t) = \frac{E_{\mathrm{f},\alpha} t^{-\alpha}}{\Gamma(1-\alpha)}. \tag{5.7}$$

In Equation (5.7), $E_{\mathrm{f},\alpha} = 814.7\,\mathrm{Pa\,s}^{\alpha}$ and $\alpha = 0.226$ have been chosen in order to fit the experimental data of Paggi and Sapora [110], being $\Gamma(\cdot)$ the Euler gamma function.

The simulation of the power-law viscoelastic response seen in the experiments, which the fractional calculus model well approximates, is progressively improved by increasing the number of terms in the Prony series representation. It has to be remarked that, since the Fourier transform of a power-law is a power-law itself, both loss and storage modulus in the frequency domain are represented, on a logarithmic scale, as straight lines.

Their trend can be satisfactorily modelled with the Prony series only for a narrow band of the whole spectrum, based on the relaxation time(s) employed. Therefore, the relaxation times entering the Prony series have to be regarded as design parameters, to be chosen based on the loading history experienced by the viscoelastic material, rather than material parameters. With the values chosen here, an accurate estimation of the material response can be expected, at most, over two orders of magnitude, centred on a frequency of 1 Hz.

5.2.2 Problem Set Up

The attention is focused on a displacement controlled problem under plane-strain assumptions. Concerning the formulation presented in 3, the profile fixed shape has been made time-dependent to account for the indenter's finite sliding. In presence of a flat interface, the result of the indenter sliding with a given constant velocity v_0 can be achieved by setting $h(\xi, t) = h(\xi - v_0 t)$. In the given test problem, the indenter profile is

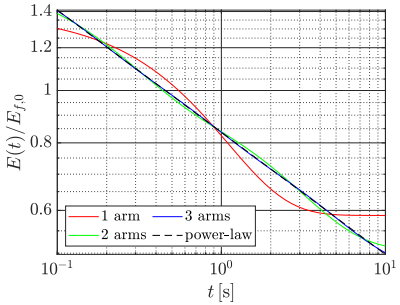

(a) Relaxation modulus.

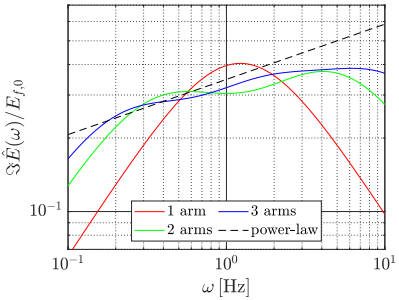

(b) Loss modulus.

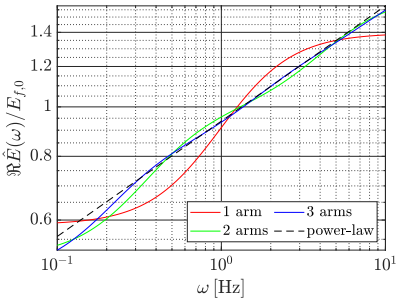

(c) Storage modulus.

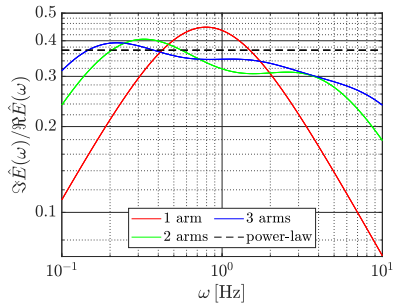

(d) Tangent modulus.

Figure 60: Relaxation modulus in time and frequency domain.

analytically expressed by:

$$\frac{h(x,t)}{g_0} = 1 - \cos\left[\frac{2\pi}{\lambda_0}(x - vt)\right] \tag{5.8}$$

In the first stage, a displacement linearly increasing with time is applied along the direction normal to the finite layer, up to a given final value of $\Delta_{n,0} = 2g_0$, reached at $t = t_0$, which is then held constant. At this point, a tangential displacement with a constant horizontal velocity is applied to the indenter, sliding.

While the velocity of the application of normal load is the same for all the simulations and assumed to be quasi-static, for what concerns the

horizontal load, different sliding velocities have been considered in the range $v_i = 10^{(i-10)/3}$, $i = [1, \ldots, 10]$, with their numerical value being summarised in Tab. 5.

Table 5: Range of horizontal velocities employed.

$\boldsymbol{v}$ **[m/s]**
1.000×10^{-03}
2.154×10^{-03}
4.642×10^{-03}
1.000×10^{-02}
2.154×10^{-02}
4.642×10^{-02}
1.000×10^{-01}
2.154×10^{-01}
4.642×10^{-01}
$1.000 \times 10^{+00}$

A friction coefficient of $\mu = 0.2$ is considered. Fig. 61 lists the remaining geometric parameters that describe the problem set, together with the rheological model employed for modelling viscoelasticity, already discussed in Sec. 5.2.1: three different simulations are performed, each of them characterised by one, two, or three terms of a Prony series used for modelling a linear viscoelastic material. The model geometry, together with the applied velocities, is the same in all cases considered. Finally, periodic boundary conditions have been introduced in correspondence with the two vertical sides of the domain to simulate a semi-indefinite contact in the horizontal direction.

5.2.3 Results

Bulk Stresses

Fig. 62 shows the results of FEM simulations for the boundary value problem shown in Fig. 61. They refer to the single-arm model, but from

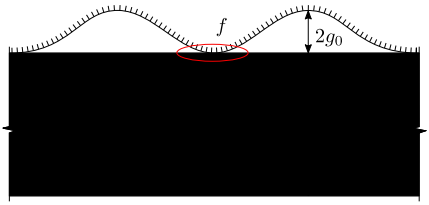

Figure 61: Sketch of the model, $b = 1$, $\lambda_0 = b$, $g_0 = 5 \times 10^{-4}\lambda_0$.

a qualitative point of view, the considerations that are drawn below for the bulk stress also apply to the other two models herein considered.

Fig. 62a,b display the stresses developing in the bulk at the end of the normal loading stage, and they display three distinct areas with high stresses where the harmonic profile comes into contact. Because of the presence of friction and coupling effects, an anti-symmetric distribution of τ_{xz} arises, even in the pure normal loading stage, see Fig. 62b. The following two figures represent the same quantities at a subsequent load stage, where the normal imposed displacement has reached its maximum, and the indenter slides at a constant velocity. Fig. 62c,d show the stresses during the next stage of sliding, corresponding to a lateral shift of the harmonic profile of about half of its wavelength. The advantage of the finite element method is evident from the possibility of considering any finite-size problem geometry and boundary conditions. In this case, the output automatically includes not only contact tractions but also bulk stresses.

Interface Tractions

Fig. 63 highlights the evolution of contact tractions in time for the single-arm model and selected contact simulation stages. The curves in Fig. 63a correspond to the purely normal loading sequence, where normal contact tractions progressively increase along with the value of the applied normal displacement, which linearly rises from zero up to the final value of $2g_0$. Black curves denote the symmetric distribution of normal contact tractions $p_{\mathrm{n}}(x)$ scaled by $E_{f,0}$, while red curves represent the anti-

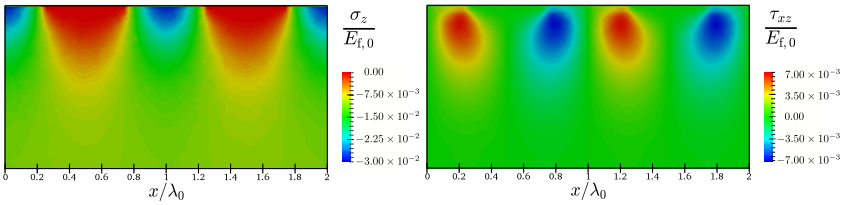

(a) σ_z, normal loading stage. **(b)** τ_{xz}, normal loading stage.

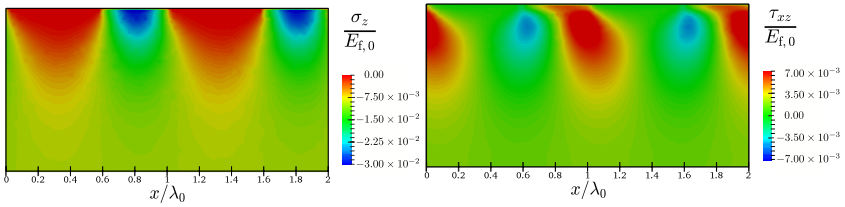

(c) σ_z, tangential loading stage. **(d)** τ_{xz}, tangential loading stage.

Figure 62: Model predictions: bulk stresses during the normal approach, (**a**,**b**), and during full sliding, (**c**,**d**), all scaled by a reference elastic modulus $E_{f,0} = 8.147 \times 10^2$ Pa.

symmetric distribution of tangential contact tractions $q_1(x)$, scaled by $\mu E_{f,0}$. Points along the interface, where $|q_1(x)|/(\mu E_{f,0}) = p_\mathrm{n}(x)/E_{f,0}$, are in a state of slip. On the other hand, the inequality $|q_1(x)|/(\mu E_{f,0}) < p_\mathrm{n}(x)/E_{f,0}$ is the condition that must be respected for having a state of stick.

Fig. 63b refers to the next stage of the contact problem when, keeping the normal displacement constant, a far-field displacement linearly increasing with time is applied in the tangential direction. For the given rheological model, the results shown in Fig. 63a are evaluated in a condition of zero tangential velocity, Fig. 63b–d are referred to $v = 2.154 \times 10^{-2}$. This specific value has been chosen amid the other entries of Tab. 5, because it is in the middle of the range, determining the highest viscoelastic effects, and it is also low enough for accurately capture the transition from *stick/slip* to *full sliding*, Fig. 63b. Here, tangential traction distributions change their shape from the classical anti-symmetric form towards

a state of increasing slip, which terminates in the full slip condition. The transition from *stick-slip* to *full slip* is strongly affected by the velocity of the horizontal displacement: the faster the slip, the more abrupt such a transition.

Fig. 63c refers to the situation of sliding after full slip (*gross sliding*) and, in particular, it shows the evolution over time of the normal contact tractions. We assist to a transition from the symmetric contact tractions distribution over the whole interface at the onset of full slip, as shown in black, towards other distributions in different scales of grey shifted along the interface to the right, as long as the tangential displacement increases. A certain degree of relaxation is observed after the onset of full slip. As the sliding proceeds in time, virgin material is perturbed, and stiffness' recovery takes place.

Finally, Fig. 63d captures the first overlapping of a new contact zone with a previously loaded portion of the interface. Here, the relaxation time role is important since viscoelastic effects do alter the solution that corresponds to a linear elastic material with no memory effects.

The resultant tangential force Q_1, integral of tangential contact tractions along the interface, is plotted vs time in Fig. 64a–c for the three viscoelastic models herein investigated. Different curves correspond to different far-field horizontal displacement velocities in each subfigure, with darker curves corresponding to slower velocities.

In all of the cases, for $t/t_0 \leq 1$, tangential tractions are vanishing since, in that stage, the imposed displacement is only acting in the normal direction. Therefore, tangential contact tractions are due to frictional coupling effects, and their sum over the whole contact zones is vanishing by definition since they correspond to self-equilibrated distributions. For $t/t_0 > 1$, the indenter starts sliding, and we assist to a transition from *stick-slip* to *full slip* with an oscillatory behaviour when the contact profile enters in contact with unrelaxed material portions. When the velocity is low, no rate effects are evident, and the mechanical response is smooth. On the other hand, by increasing the applied velocity, the importance of viscoelasticity increases and oscillating responses do appear.

The integral of tangential tractions related to two linear elastic models

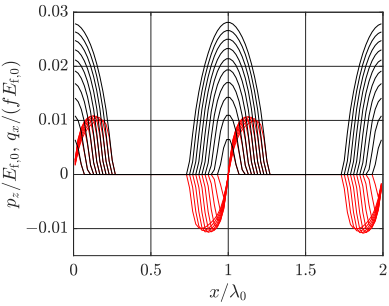

(a) p_z and q_x during the normal loading stage.

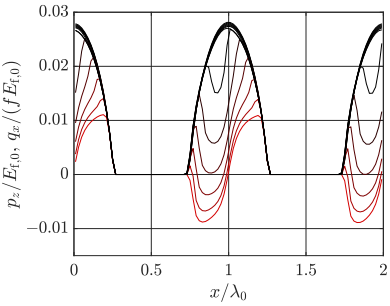

(b) Tractions in the partial-slip regime.

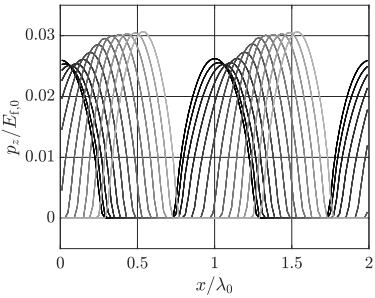

(c) Normal traction during full sliding.

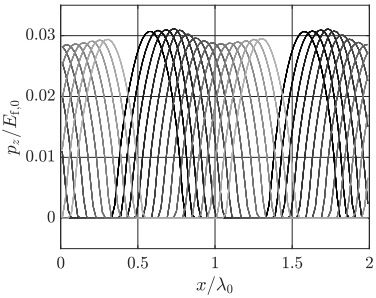

(d) Normal traction during interaction with an already stressed portion of the interface.

Figure 63: Selected distributions of normal and tangential contact tractions during the different stages of loading.

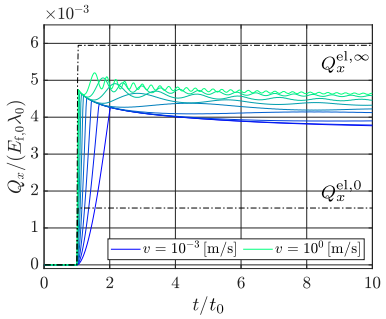

(a) Three arms.

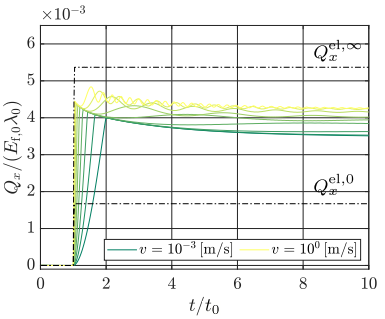

(b) Two arms.

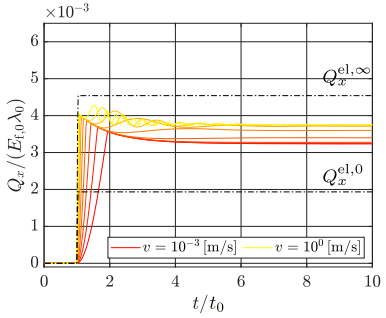

(c) One arm.

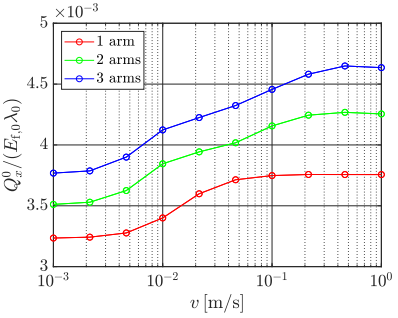

(d) Trend for the steady-state values at $t \to \infty$.

Figure 64: Time evolution of the resultant tangential force Q_x for different rheological models.

characterised by short and long term modulus are also plotted in Fig. 64: for comparison, see black dash-dotted lines. The elastic moduli are evaluated as:

$$E^{\mathrm{el},\infty} = \lim_{t\to 0} E(t) = E^{\infty} \qquad E^{\mathrm{el},0} = \lim_{t\to \infty} E(t) = E^{\infty}(1 - \sum_{i=1}^{n} \mu_i) \tag{5.9}$$

The curves $Q_1^{\mathrm{el},\infty}$ and $Q_1^{\mathrm{el},0}$ are evaluated under the assumption of linear elasticity, neglecting the dynamic effects. For this reason, they lead to constant values as soon as the horizontal far-field displacement is ap-

plied, without any oscillation. The only factor that plays a role is the velocity, which governs the transition from *stick/slip* to full sliding. In the figures, only the curves that correspond to the highest value of v are plotted. In all three models, the instantaneous (higher) and long term (lower) curves are extreme bounds to the values related to viscoelastic simulations, with a gap increasing from the single-arm to the three arms model, consistent with their respective stiffness.

The steady-state solution strongly depends on the rheological properties of the material, as shown in Fig. 64d. In general, for the present case study, the higher the number of arms, the higher the total tangential force. In all cases, the highest velocity determines the highest value of the steady-state Q_1^0. This follows that, in a condition of *gross slip*, $Q_1 = \mu P$. For high velocities, the material is excited in its high-frequency region, resulting in a vertical response governed by the higher *glassy* Young's modulus. The increased stiffness leads to higher P^0 and, in turn, higher Q_1^0 values.

Chapter 6

Conclusions and further developments

The formulations proposed in the present dissertation provide a way to overcome some of the shortcomings and difficulties encountered during the definition and the solution of contact problems between rough or generically complex profiles and surfaces.

In Ch. 2, the complete $2D$ and $3D$ formulations of an interface element, initially employed in the context of non-linear fracture mechanics, is presented. Starting from the strong form of equilibrium, the related weak form has been derived, down to the non-linear system of equations which could be directly embedded in a standard FEM software.

An extension of the interface element is exposed in Ch. 3. Following the framework originally proposed in [79] and further extended in [56], its capabilities have been enriched to deal with rough contact problems, still maintaining a smooth interface that allows for a straightforward meshing, requiring low-order linear finite elements. In contrast, the actual geometry is stored in terms of its analytical expression and passed to the system as a correction of the initial gap function under the assumption of having a rigid indenting body. The major advantages obtained by exploiting this approach are the possibility of using a low-order finite element discretisation scheme and a regular mesh at the interface, with

a reduction of the number of nodal degrees of freedom and ease of mesh definition. A classical benchmark test has been used for validating the model, with excellent results obtained even for coarse interface discretisations. The method has been successfully tested concerning the more complex scenarios of contact problems involving quasi-fractal self-affine Weierstrass profiles and surfaces with multiple harmonics, resulting in a useful tool for investigating the behaviour of idealized $2D$ interfaces in the presence of frictional forces.

The assumption which has been made a priori are rather strict if compared to the current scenario of computational contact mechanics, and they can be summarised here:

(i) requirement of a matching interface that results in the necessity of a node-to-node approach;

(ii) small displacements;

(iii) one of the body is assumed to be rigid, where the complexities related to the geometry are supposed to be localised;

(iv) penalty strategy for contact.

Nevertheless, it has to be remarked that none of them represents a strict prerequisite, thus leaving broad possibilities of extending the model and its capabilities. Non-matching interfaces could be considered, for example, defining, in analogy with [65], a node-to-segment based interface element. The hypothesis of small displacements could be lifted, easily for what concerns frictionless contact, with a proper definition of the tangent stiffness matrix, cfr. Eq. (2.7.1), taking into account the dependence of $\mathbf{Q}$ on the interface displacements, resulting in an additional geometric term composing the linearised local gap vector. Also, the use of a penalty approach is not cogent. It presents several features that make it preferable concerning other techniques that guarantee the exact respect of contact conditions. Above the others, its implementation is straightforward and does not add additional variables to the problem. Secondly, it easily allows for the extension of the model towards studying multiphysics phenomena, e.g. thermomechanical contact. Assumption *(iv)* is

probably the most conceptually difficult to be relaxed, but some useful considerations can be drawn here as well. As a starting point, it is good to remark that in the context of rough surfaces contact analysis via FEM, the use of two sets of materials, one of which is rigid, is a prevalent practice thanks to the exploitation of the composite topography and composite mechanical assumptions made in Sec. 3.1.3. Moreover, the rigidity requirements only involve the surface's shape, which is fixed and defined initially. Thus, the remaining part of the bulk could be characterised by a different constitutive law, with the confinement of the rigid part in the interface's correspondence. From the tribological perspective, this is a reasonable assumption since surfaces manufacturing processes involve plastic deformations that generate surface layers that can be orders of magnitude harder than the rest of the bulk. Given all these considerations, the proposed approach appears to be entitled to an accurate systematic analysis of several important engineering applications classes.

In Ch. 5, the model has also been successfully tested in the presence of an inelastic material [58]. In the specific, the bulk has been modelled using a linear viscoelastic material with three relaxation times. Compared to many models available in the literature that neglect the effect of Coulomb friction, focusing on viscoelastic dissipation only, here viscoelastic effects and frictional effects can be simultaneously investigated since they are inherently coupled in the formulation. Neglecting interface tangential tractions, together with their coupling effect, is reasonable when a condition of incompressibility is approached since it determines de-coupling between the normal and tangential directions. On the other hand, several pieces of evidence can be found that, as Young's modulus of viscoelastic material changes with time, so does the Poisson's ratio. Since this latter quantity governs the coupling between normal and tangential tractions, a fully coupled model is worth to be analysed for fine precision engineering applications.

In addition to the embedded interface model, a multi-scale FEM-BEM contact mechanics formulation [57] has been proposed to address frictionless contact problems involving a nominally smooth surface at the macro-scale and a microscopically rough topology at the micro-scale,

Ch. 4. The assumption of scale separation is put forward, which assumes that a statistically representative rough surface can be defined at each point along the macroscopic contact surface. The coupling of the two scales is enforced by passing the normal gap at each integration point of the interface finite element to the boundary element code to solve the microscopical frictionless contact problem. In return to the macro-scale, the homogenised normal contact traction and the related tangent stiffness matrix are provided.

Compared to the previous literature, the approach does not exploit a closed-form solution at the micro-scale which relies on a micromechanical contact model that implies assumptions on the roughness statistics. BEM can, in fact, be applied to any height field without any simplifying assumption. The approach is only focused on linear elastic contact, and the study of the effects of plasticity go beyond the scopes of the dissertation. Future developments might consider integrating the BEM, using appropriate Green functions, and the FEM solutions considering a general elastoplastic behaviour with a constant yielding strength.

In conclusion, two main different strategies have been presented in this dissertation to solve contact problems involving complex contacting interfaces. Rather than giving new insights over the problems addressed, this work has aimed to provide a sound support scheme for easier and straightforward implementation in the given context, together with the perspectives of possible future developments, which are supposed to add further value to the work that has been carried on so far.

Bibliography

[1] F. P. Bowden and D. Tabor. *The friction and lubrication of solids*. Oxford: Clarendon Press, 1950.

[2] H. Hertz. "Über die Berührung fester elasticher Körper(On the contact of elastic solids)". In: *Z. Reine Angew. Mathematik* **92** (1881), pp. 156–171.

[3] J. F. Archard. "Elastic deformation and the laws of friction". In: *Proceedings of the Royal Society A* **243**.1233 (Dec. 1957), pp. 190–205. DOI: https://doi.org/10.1098/rspa.1957.0214.

[4] Benoit Mandelbrot. "Fractal Geometry of Nature". In: 1977.

[5] B. N.J. Persson. "On the fractal dimension of rough surfaces". In: *Tribology Letters* **54**.1 (2014), pp. 99–106. DOI: 10.1007/s11249-014-0313-4.

[6] J. A. Greenwood and J. B. P. Williamson. "Contact of nominally flat surfaces". In: *Proceedings of the Royal Society of London A: Mathematical, Physical and Engineering Sciences* 295 (1966), pp. 300–319. DOI: 10.1098/rspa.1966.0242.

[7] A.W. Bush, R.D. Gibson, and T.R. Thomas. "The elastic contact of a rough surface". In: *Wear* **35**.1 (1975), pp. 87–111. DOI: https://doi.org/10.1016/0043-1648(75)90145-3.

[8] Majumdar A. and B. Bhusan. "Fractal Model of Elastic-Plastic Contact Between Rough Surfaces". In: *Journal of Tribology* **113** (1991), pp. 1–11. DOI: 10.1115/1.2920588.

[9] B. N. J. Persson. "Theory of Rubber Friction and Contact Mechanics". In: *The Journal of Chemical Physics* **115** (2001), p. 3840. DOI: 10.1063/1.1388626.

[10] J. A. Greenwood and J. H. Tripp. "The elastic contact of rough spheres". In: *Journal of Applied Mechanics, Transactions ASME* **34**.1 (1967), pp. 153–159. DOI: 10.1115/1.3607616.

[11] Roman Pohrt and Valentin L. Popov. "Contact mechanics of rough spheres: Crossover from fractal to Hertzian behavior". In: *Advances in Tribology* **2013**.1 (2013), pp. 1–5. DOI: 10.1155/2013/974178.

[12] Vladislav A. Yastrebov. "The Elastic Contact of Rough Spheres Investigated Using a Deterministic Multi-Asperity Model". In: *Journal of Multiscale Modelling* **10**.1 (2018). DOI: 10.1142/s1756973718410020.

[13] J. A. Greenwood. "A simplified elliptic model of rough surface contact". In: *Wear* **261**.2 (2006), pp. 191–200. DOI: 10.1016/j.wear.2005.09.031.

[14] Michele Ciavarella, V. Delfine, and G. Demelio. "A "re-vitalized" Greenwood and Williamson model of elastic contact between fractal surfaces". In: *Journal of the Mechanics and Physics of Solids* **54** (2006), pp. 2569–2591. DOI: 10.1016/j.jmps.2006.05.006.

[15] Michele Ciavarella, J. A. Greenwood, and Marco Paggi. "Inclusion of "interaction" in the Greenwood and Williamson contact theory". In: *Wear* **265**.5-6 (2008), pp. 729–734. DOI: 10.1016/j.wear.2008.01.019.

[16] Carlo Cattaneo. "Sul contatto di due corpi elastici: distribuzione locale degli sforzi." In: *Rendiconti dell'Accademia nazionale dei Lincei* **27** (1938), 342–348,
bibrangessep 431–436,
bibrangessep 474–478.

[17] R. D. Mindlin. "Compliance Of Elastic Bodies In Contact". In: *ASME Journal of Applied Mechanics* **16**.3 (1949), pp. 259–268.

[18] R. D. Mindlin and H. Deresiewizc. "Elastic Spheres in contact under varying oblique forces". In: *ASME Journal of Applied Mechanics* **20**.3 (1953), pp. 327–344.

[19] J. Jäger. "Stepwise Loading of Half-Spaces in Elliptical Contact". In: *Journal of Applied Mechanics* **63**.3 (Sept. 1996), pp. 766–773. DOI: 10.1115/1.2823361.

[20] J. Jäger. "A New Principle in Contact Mechanics". In: *Journal of Tribology* **120**.4 (Oct. 1998), pp. 677–684. DOI: 10.1115/1.2833765.

[21] Michele Ciavarella. “The generalized Cattaneo partial slip plane contact problem. I–Theory”. In: *International Journal of Solids and Structures* **35**.18 (1998), pp. 2349–2362. ISSN: 0020-7683. DOI: https://doi.org/10.1016/S0020-7683(97)00154-6.

[22] Michele Ciavarella. “The generalized Cattaneo partial slip plane contact problem. II–Examples”. In: *International Journal of Solids and Structures* **35**.18 (1998), pp. 2363–2378. ISSN: 0020-7683. DOI: https://doi.org/10.1016/S0020-7683(97)00155-8.

[23] AI Vakis et al. “Modeling and Simulation in Tribology Across Scales: an Overview”. In: *Tribology International* (2018). DOI: 10.1016/j.triboint.2018.02.005.

[24] M.H. Müser et al. “Meeting the Contact-Mechanics Challenge”. In: *Tribology Letters* 65.4 (Aug. 2017), p. 118. DOI: 10.1007/s11249-017-0900-2.

[25] Torbjörn Andersson. “The Boundary Element Method applied to Two-Dimensional Contact Problems with Friction”. In: *Boundary Element Methods*. Ed. by Carlos A. Brebbia. Berlin, Heidelberg: Springer Berlin Heidelberg, 1981, pp. 239–258. ISBN: 978-3-662-11270-0.

[26] T. Andersson and B. G. Allan-Persson. “The boundary element method applied to two-dimensional contact problems”. In: *Progress in Boundary Element Methods: Volume 2*. Ed. by Carlos A. Brebbia. New York, NY: Springer New York, 1983, pp. 136–157. ISBN: 978-1-4757-6300-3. DOI: 10.1007/978-1-4757-6300-3_5.

[27] Yang Xu and Robert L. Jackson. “Boundary element method (BEM) applied to the rough surface contact vs. BEM in computational mechanics”. In: *Friction* **7**.4 (2019), pp. 359–371. DOI: 10.1007/s40544-018-0229-3.

[28] K. L. Johnson. *Contact Mechanics*. Cambridge University Press, Cambridge, UK, 1985.

[29] A. E. H. Love. “The stress produced in a semi-infinite solid by pressure on part of the boundary”. In: *Philosophical Transactions of the Royal Society of London. Series A, Containing Papers of a Mathematical or Physical Character* **228**.659-669 (1929), pp. 377–420. DOI: 10.1098/rsta.1929.0009.

[30] Junshan Li and Edward J. Berger. "A Boussinesq-Cerruti solution set for constant and linear distribution of normal and tangential load over a triangular area". In: *Journal of Elasticity* **63**.2 (2001), pp. 137–151. DOI: 10.1023/A:1014013425423.

[31] H. D. Conway et al. "Normal and shearing contact stresses in indented strips and slabs". In: *International Journal of Engineering Science* **4**.4 (1966), pp. 343–359. DOI: 10.1016/0020-7225(66)90036-x.

[32] R. H. Bentall and K. L. Johnson. "An elastic strip in plane rolling contact". In: *International Journal of Mechanical Sciences* **10**.8 (1968), pp. 637–663. DOI: 10.1016/0020-7403(68)90070-2.

[33] J. A. Greenwood and J. R. Barber. "Indentation of an elastic layer by a rigid cylinder". In: *International Journal of Solids and Structures* **49**.21 (2012), pp. 2962–2977.

[34] Alberto Bemporad and Marco Paggi. "Optimization algorithms for the solution of the frictionless normal contact between rough surfaces". In: *International Journal of Solids and Structures* **69–70** (2015), pp. 94–105.

[35] E. A.H. Vollebregt. "A new solver for the elastic normal contact problem using conjugate gradients, deflation, and an FFT-based preconditioner". In: *Journal of Computational Physics* **257**.PA (2014), pp. 333–351. DOI: 10.1016/j.jcp.2013.10.005. URL: http://dx.doi.org/10.1016/j.jcp.2013.10.005.

[36] Marco Paggi, Roman Pohrt, and Valentin L. Popov. "Partial-slip frictional response of rough surfaces". In: *Scientific Reports* **4** (2014), pp. 1–6. DOI: 10.1038/srep05178.

[37] Roman Pohrt and Qiang Li. "Complete boundary element formulation for normal and tangential contact problems". In: *Physical Mesomechanics* **17** (Oct. 2014), pp. 334–340. DOI: 10.1134/s1029959914040109.

[38] Giuseppe Carbone and Carmine Putignano. "A novel methodology to predict sliding and rolling friction of viscoelastic materials: Theory and experiments". In: *Journal of the Mechanics and Physics of Solids* **61**.8 (2013), pp. 1822–1834. DOI: https://doi.org/10.1016/j.jmps.2013.03.005.

[39] C. Putignano and G. Carbone. "A review of boundary elements methodologies for elastic and viscoelastic rough contact mechanics". In: *Physical Mesomechanics* **17**.4 (2014), pp. 321–333. DOI: 10.1134/S1029959914040092.

[40] C. Putignano, T. Reddyhoff, and D. Dini. "The influence of temperature on viscoelastic friction properties". In: *Tribology International* **100** (2016), pp. 338–343. DOI: https://doi.org/10.1016/j.triboint.2016.03.018.

[41] Jing Zhao, Edwin A.H. Vollebregt, and Cornelis W. Oosterlee. "Extending the BEM for Elastic Contact Problems Beyond the Half-Space Approach". In: *Mathematical Modelling and Analysis* **21**.1 (2016), pp. 119–141. DOI: 10.3846/13926292.2016.1138418.

[42] Peter Wriggers. *Computational Contact Mechanics*. Springer-Verlag Berlin Heidelberg, 2006. DOI: 10.1007/978-3-540-32609-0.

[43] Vladislav A. Yastrebov and Piotr Breitkopf. *Numerical Methods in Contact Mechanics*. 2013. ISBN: 9781848215191. DOI: 10.1002/9781118647974.

[44] Alexander Popp. "Mortar Methods for Computational Contact Mechanics and General Interface Problems". In: September (2012), p. 34.

[45] Laura De Lorenzis, Peter Wriggers, and Thomas J.R. Hughes. "Isogeometric contact: A review". In: *GAMM Mitteilungen* **37**.1 (2014), pp. 85–123. DOI: 10.1002/gamm.201410005.

[46] S. Hyun et al. "Finite-element analysis of contact between elastic self-affine surfaces". In: *Physical Review E - Statistical Physics, Plasmas, Fluids, and Related Interdisciplinary Topics* **70**.2 (2004), p. 12. DOI: 10.1103/PhysRevE.70.026117.

[47] Alex Alves Bandeira, Peter Wriggers, and Paulo de Mattos Pimenta. "Numerical derivation of contact mechanics interface laws using a finite approach for large 3D deformation". In: *International Journal for Numerical Methods in Engineering* **59**.2 (2004), pp. 173–195. DOI: 10.1002/nme.867.

[48] Vladislav A. Yastrebov et al. "Rough surface contact analysis by means of the Finite Element Method and of a new reduced model". In: *Comptes Rendus - Mecanique* **339**.7-8 (2011), pp. 473–490. DOI: 10.1016/j.crme.2011.05.006. URL: http://dx.doi.org/10.1016/j.crme.2011.05.006.

[49] A. M. Couto Carneiro, R. Pinto Carvalho, and F. M. Andrade Pires. "Representative contact element size determination for micromechanical contact analysis of self-affine topographies". In: *International Journal of Solids and Structures* **206** (2020), pp. 262–281. DOI: 10.1016/j.ijsolstr.2020.09.006. URL: https://doi.org/10.1016/j.ijsolstr.2020.09.006.

[50] Xianzhang Wang et al. "The effect of resolution on the deterministic finite element elastic-plastic rough surface contact under combined normal and tangential loading". In: *Tribology International* **144**.December 2019 (2020), p. 106141. ISSN: 0301679X. DOI: 10.1016/j.triboint.2019.106141. URL: https://doi.org/10.1016/j.triboint.2019.106141.

[51] Mary Kathryn Thompson and John M. Thompson. "Considerations for the incorporation of measured surfaces in finite element models". In: *Scanning* **32**.4 (2010), pp. 183–198. DOI: 10.1002/sca.20180.

[52] Mary Kathryn Thompson. "A comparison of methods to evaluate the behavior of finite element models with rough surfaces". In: *Scanning* **33**.5 (2011), pp. 353–369. DOI: 10.1002/sca.20252.

[53] Vladislav A. Yastrebov, Guillaume Anciaux, and Jean François Molinari. "On the accurate computation of the true contact-area in mechanical contact of random rough surfaces". In: *Tribology International* **114** (2017), pp. 161–171. ISSN: 0301679X. DOI: 10.1016/j.triboint.2017.04.023. arXiv: 1701.02727.

[54] Fabian Loth et al. "Surface roughness in finite element meshes". In: *arXiv* (2020). arXiv: 2002.00894.

[55] Christophe Geuzaine and Jean-François Remacle. "Gmsh: A 3-D finite element mesh generator with built-in pre- and post-processing facilities". In: *International Journal for Numerical Methods in Engineering* **79**.11 (2009), pp. 1309–1331. DOI: https://doi.org/10.1002/nme.2579. URL: https://onlinelibrary.wiley.com/doi/abs/10.1002/nme.2579.

[56] Jacopo Bonari, Marco Paggi, and José Reinoso. "A framework for the analysis of fully coupled normal and tangential contact problems with complex interfaces".

[57] Jacopo Bonari et al. “A multi-scale FEM-BEM formulation for contact mechanics between rough surfaces”. In: *Computational Mechanics* **65** (2019), pp. 731–749. DOI: https://doi.org/10.1007/s00466-019-01791-3.

[58] Jacopo Bonari and Marco Paggi. “Viscoelastic Effects during Tangential Contact Analyzed by a Novel Finite Element Approach with Embedded Interface Profiles”. In: *Lubricants* **8**.12 (2020). ISSN: 2075-4442. DOI: 10.3390/lubricants8120107. URL: https://www.mdpi.com/2075-4442/8/12/107.

[59] Michael Ortiz and Anna Pandolfi. “Finite deformation irreversible cohesive elements for three-dimensional crack-propagation analysis”. In: *International Journal for Numerical Methods in Engineering* **44** (1999), pp. 1267–1282. DOI: 10.1002/(SICI)1097-0207(19990330)44:93.3.CO;2-Z.

[60] José Reinoso and Marco Paggi. “A consistent interface element formulation for geometrical and material nonlinearities”. In: *Computational Mechanics* 54.6 (2014), pp. 1569–1581.

[61] Marco Paggi, Alberto Carpinteri, and Giorgio Zavarise. “A unified interface constitutive law for the study of fracture and contact problems in heterogeneous materials”. In: *Analysis and Simulation of Contact Problems, Lecture Notes in Applied and Computational Mechanics* 27 (2006), pp. 297–304.

[62] Marco Paggi and Peter Wriggers. “A nonlocal cohesive zone model for finite thickness interfaces – Part I: Mathematical formulation and validation with molecular dynamics”. In: *Computational Materials Science* 50.5 (2011), pp. 1625–1633. DOI: https://doi.org/10.1016/j.commatsci.2010.12.024.

[63] Marco Paggi and Peter Wriggers. “A nonlocal cohesive zone model for finite thickness interfaces–Part II: FE implementation and application to polycrystalline materials”. In: *Computational Materials Science* 50.5 (2011), pp. 1634–1643.

[64] Marco Paggi et al. “A numerical investigation of the interplay between cohesive cracking and plasticity in polycrystalline materials”. In: *Computational Materials Science* 77 (2013), pp. 81–92. DOI: https://doi.org/10.1016/j.commatsci.2013.04.002.

[65] Marco Paggi and Peter Wriggers. “Node-to-segment and node-to-surface interface finite elements for fracture mechanics”. In: *Computer Methods in Applied Mechanics and Engineering* 300 (2016), pp. 540–560. DOI: https://doi.org/10.1016/j.cma.2015.11.023.

[66] Mohit Pundir and Guillaume Anciaux. “Coupling between cohesive element method and node-to-segment contact algorithm: Implementation and application”. In: *International Journal for Numerical Methods in Engineering* n/a.n/a (2020). DOI: https://doi.org/10.1002/nme.6705.

[67] Gregorio Mariggiò et al. “Peeling of thick adhesive interfaces: The role of dynamics and geometrical nonlinearity”. In: *Mechanics Research Communications* 94 (2018), pp. 21–27. DOI: https://doi.org/10.1016/j.mechrescom.2018.08.018.

[68] Marco Paggi and José Reinoso. “An anisotropic large displacement cohesive zone model for fibrillar and crazing interfaces”. In: *International Journal of Solids and Structures* 69–70 (2015), pp. 106–120. DOI: https://doi.org/10.1016/j.ijsolstr.2015.04.042.

[69] Claudia Borri et al. “Adhesive behaviour of bonded paper layers: Mechanical testing and statistical modelling”. In: *Proceedings of the Institution of Mechanical Engineers, Part C: Journal of Mechanical Engineering Science* 230.9 (Oct. 2015), pp. 1440–1448. DOI: 10.1177/0954406215612502.

[70] José Reinoso, Marco Paggi, and Pedro Miguel De Almeida Areias. “A finite element framework for the interplay between delamination and buckling of rubber-like bi-material systems and stretchable electronics”. In: *Journal of the European Ceramic Society* 36.9 (2016), pp. 2371–2382. DOI: https://doi.org/10.1016/j.jeurceramsoc.2016.01.002.

[71] José Reinoso, Marco Paggi, and Antonio Blázquez. “A nonlinear finite thickness cohesive interface element for modeling delamination in fibre-reinforced composite laminates”. In: *Composites Part B: Engineering* 109 (2017), pp. 116–128. DOI: https://doi.org/10.1016/j.compositesb.2016.10.042.

[72] M.J. van den Bosch, P.J.G. Schreurs, and M.G.D. Geers. "A cohesive zone model with a large displacement formulation accounting for interfacial fibrilation". In: *European Journal of Mechanics - A/Solids* **26**.1 (2007), pp. 1–19. ISSN: 0997-7538. DOI: https://doi.org/10.1016/j.euromechsol.2006.09.003.

[73] Alberto Sapora and Marco Paggi. "A coupled cohesive zone model for transient analysis of thermoelastic interface debonding". In: *Computational Mechanics* 53 (2014), pp. 845–857. DOI: 10.1007/s00466-013-0934-8.

[74] Valerio Carollo, José Reinoso, and Marco Paggi. "A 3D finite strain model for intralayer and interlayer crack simulation coupling the phase field approach and cohesive zone model". In: *Composite Structures* 182 (2017), pp. 636–651. DOI: https://doi.org/10.1016/j.compstruct.2017.08.095.

[75] Bahram Nour-Omid and Peter Wriggers. "A note on the optimum choice for penalty parameters". In: *Communications in Applied Numerical Methods* 3 (1987), pp. 581–585.

[76] Sang-hoon Lee. "Rudimentary considerations for adaptive gap/friction element based on the penalty method". In: *Computers & Structures* 47.6 (1993), pp. 1043–1056. DOI: https://doi.org/10.1016/0045-7949(93)90308-Z.

[77] Dominique Chamoret et al. "New smoothing procedures in contact mechanics". In: *Journal of Computational and Applied Mathematics* 168.1 (2004), pp. 107–116. DOI: https://doi.org/10.1016/j.cam.2003.06.007.

[78] A. Francavilla and Olgierd Cecil Zienkiewicz. "A note on numerical computation of elastic contact problems". In: *International Journal for Numerical Methods in Engineering* **9**.4 (1975), pp. 913–924. DOI: 10.1002/nme.1620090410.

[79] Marco Paggi and José Reinoso. "A variational approach with embedded roughness for adhesive contact problems". In: *Mechanics of Advanced Materials and Structures* (2018). DOI: 10.1080/15376494.2018.1525454.

[80] Giorgio Zavarise et al. "Real contact mechanisms and finite element formulation–a coupled thermomechanical approach". In: *International Journal for Numerical Methods in Engineering* 35 (1992), pp. 767–785.

[81] H. M. Westergaard. “Bearing Pressures and Cracks: Bearing Pressures Through a Slightly Waved Surface or Through a Nearly Flat Part of a Cylinder, and Related Problems of Cracks”. In: *Journal of Applied Mechanics* **6**.2 (Mar. 1939), A49–A53. DOI: 10.1115/1.4008919.

[82] D. Nowell, D.A. Hills, and A. Sackfield. “Contact of dissimilar elastic cylinders under normal and tangential loading”. In: *Journal of the Mechanics and Physics of Solids* **36**.1 (1988), pp. 59–75. ISSN: 0022-5096. DOI: https://doi.org/10.1016/0022-5096(88)90020-8.

[83] “Filtering in the Frequency Domain”. In: *Computational Surface and Roundness Metrology*. London: Springer London, 2009, p. 13. DOI: 10.1007/978-1-84800-297-5_7.

[84] J. Raja, B. Muralikrishnan, and Shengyu Fu. “Recent advances in separation of roughness, waviness and form”. In: *Precision Engineering* **26** (2002), pp. 222–235. DOI: https://doi.org/10.1016/S0141-6359(02)00103-4.

[85] L. De Chiffre et al. “Quantitative Characterisation of Surface Texture”. In: *CIRP Annals* **49**.2 (2000), pp. 635–652. DOI: https://doi.org/10.1016/S0007-8506(07)63458-1.

[86] *Surface Texture (Surface Roughness, Waviness, and Lay)*. ASME, 2020. ISBN: 9780791873250.

[87] James Richard Barber. “Bounds on the electrical resistance between contacting elastic rough bodies”. In: *Proceedings of the Royal Society of London A* **459** (2003), pp. 53–66. DOI: 10.1098/rspa.2002.1038.

[88] James Richard Barber. *Contact Mechanics*. Springer International Publishing, 2018.

[89] Marco Paggi and James Richard Barber. “Contact conductance of rough surfaces composed of modified RMD patches”. In: *International Journal of Heat and Mass Transfer* **54** (2011), pp. 4664–4672. DOI: 10.1016/j.ijheatmasstransfer.2011.06.011.

[90] J. Andersson, A. Almqvist, and R. Larsson. “Numerical simulation of a wear experiment”. In: *Wear* **271**.11–12 (2011), pp. 2947–2952. DOI: 10.1016/j.wear.2011.06.018.

[91] A. L. Pinto et al. “Fretting fatigue under variable amplitude loading considering partial and gross slip regimes: Numerical analysis”. In: *Tribology International* **146** (2020), p. 106199. DOI: 10.1016/j.triboint.2020.106199.

[92] T. Zhang, P. E. McHugh, and S. B. Leen. “Computational study on the effect of contact geometry on fretting behaviour”. In: *Wear* **271**.9–10 (2011), pp. 1462–1480. DOI: 10.1016/j.wear.2010.11.017.

[93] I. R. McColl, J. Ding, and S. B. Leen. “Finite element simulation and experimental validation of fretting wear”. In: *Wear* **256**.11-12 (2004), pp. 1114–1127. DOI: 10.1016/j.wear.2003.07.001.

[94] M. Michael Yovanovich, J. Devaal, and A. H. Hegazy. “A statistical model to predict thermal gap conductance between conforming rough surfaces”. In: *3rd Joint Thermophysics, Fluids, Plasma and Heat Transfer Conference*. Reston, Virigina: American Institute of Aeronautics and Astronautics, June 1982. DOI: 10.2514/6.1982-888. URL: http://arc.aiaa.org/doi/10.2514/6.1982-888.

[95] M. Michael Yovanovich, A. H. Hegazy, and J. Devaal. “Surface hardness distribution effects upon contact, gap and joint conductances”. In: *3rd Joint Thermophysics, Fluids, Plasma and Heat Transfer Conference*. Reston, Virigina: American Institute of Aeronautics and Astronautics, June 1982. DOI: 10.2514/6.1982-887. URL: http://arc.aiaa.org/doi/10.2514/6.1982-887.

[96] L. E. Goodman. “Contact Stress Analysis of Normally Loaded Rough Spheres”. In: *Journal of Applied Mechanics* **29**.3 (Sept. 1962), pp. 515–522. ISSN: 0021-8936. DOI: 10.1115/1.3640599.

[97] D. A. Spence. “The Hertz contact problem with finite friction”. In: *Journal of Elasticity* **5**.0 (1975), pp. 297–319. DOI: https://doi.org/10.1007/BF00126993.

[98] B. Stingl, M. Ciavarella, and N. Hoffmann. “Frictional dissipation in elastically dissimilar oscillating Hertzian contacts”. In: *International Journal of Mechanical Sciences* **72** (2013), pp. 55–62. DOI: https://doi.org/10.1016/j.ijmecsci.2013.03.012.

[99] M. Ciavarella et al. “Linear elastic contact of the Weierstrass profile”. In: *Proceedings of the Royal Society of London A: Mathematical, Physical and Engineering Sciences* 456.1994 (2000), pp. 387–405. DOI: 10.1098/rspa.2000.0522.

[100] M. Ciavarella et al. “Elastic contact stiffness and contact resistance for the Weierstrass profile”. In: *Journal of the Mechanics and Physics of Solids* **52**.6 (2004), pp. 1247–1265. ISSN: 0022-5096. DOI: https://doi.org/10.1016/j.jmps.2003.12.002.

[101] *The Science of Fractal Images*. Springer-Verlag New York, 1988. ISBN: 978-1-4612-8349-2.

[102] P. Wriggers and J. Reinelt. “Multi-scale approach for frictional contact of elastomers on rough rigid surfaces”. In: *Computer Methods in Applied Mechanics and Engineering* 198 (2009), pp. 1996–2008. DOI: 10.1016/j.cma.2008.12.021.

[103] Y. Waddad et al. “A multiscale method for frictionless contact mechanics of rough surfaces”. In: *Tribology International* **96** (2016), pp. 109–121. ISSN: 0301-679X. DOI: https://doi.org/10.1016/j.triboint.2015.12.023.

[104] L. A. Galin. *Contact Problems in the Theory of Elasticity*. Ed. by I. N. Sneddon. North Carolina State College translation., 1961.

[105] H. D. Conway and K.A. Farnham. “The relationship between load and penetration for a rigid, flat-ended punch of arbitrary cross section”. In: *International Journal of Engineering Science* **6**.9 (1968), pp. 489–496. DOI: 10.1016/0020-7225(68)90001-3.

[106] H. O. Peitgen, D. Saupe, and M. F. Barnsley. *The Science of fractal images*. Springer-Verlag, 1988. ISBN: 9780387966083.

[107] Ulrich Eitner et al. “Non-linear mechanical properties of ethylene-vynil acetate (EVA) and its relevance to thermomechanics photovoltaic odules”. In: *Proceedings of the 25th European Conference on Photovoltaic Solar Energy* (2010), pp. 4366–4368.

[108] U. Eitner. “Thermomechanics of photovoltaic modules”. PhD thesis. Zentrum für Ingenieurwissenschaften der Martin-Luther-Universität Halle-Wittemberg, 2011.

[109] Marco Paggi, S. Kajari-Schröder, and U. Eitner. “Thermomechanical deformations in photovoltaic laminates”. In: *The Journal of Strain Analysis for Engineering Design* **46**.8 (2011), pp. 772–782. DOI: 10.1177/0309324711421722.

[110] Marco Paggi and Alberto Sapora. “An Accurate Thermoviscoelastic Rheological Model for Ethylene Vinyl Acetate Based on Fractional Calculus”. In: *International Journal of Photoenergy* **2015** (2015). DOI: 10.1155/2015/252740.

[111] M. Gagliardi, P. Lenarda, and M. Paggi. "A reaction-diffusion formulation to simulate EVA polymer degradation in environmental and accelerated ageing conditions". In: *Solar Energy Materials and Solar Cells* **164** (2017), pp. 93–106. DOI: https://doi.org/10.1016/j.solmat.2017.02.014.